
Cascades of antiprotonic helium measured at low target densities

Kaskaden von antiprotonischem Helium gemessen bei niedrigen Targetdichten

Hossein Aghai-Khozani



München 2016

Cascades of antiprotonic helium measured at low target densities

Kaskaden von antiprotonischem Helium gemessen bei niedrigen Targetdichten

Hossein Aghai-Khozani

Dissertation
an der Fakultät für Physik
der Ludwig-Maximilians-Universität
München

vorgelegt von
Hossein Aghai-Khozani
aus Teheran

München, den 17.06.2016

Erstgutachter: Prof. Dr. Theodor W. Hänsch

Zweitgutachter: Prof. Dr. Randolph Pohl

Tag der mündlichen Prüfung: 22.07.2016

Abstract

Metastable antiprotonic helium ($\bar{\text{pHe}}^+$) is an exotic atom consisting of a helium nucleus, an electron in the ground $1s$ state and an antiproton in a Rydberg state of large principal ($n \sim 38$) and angular momentum quantum number ($\ell \sim n$). $\bar{\text{pHe}}^+$ atoms in metastable states are stable against fast ($\sim \text{ns}$) Auger decay because of their large ℓ values. Instead they undergo slow ($\sim \mu\text{s}$) radiative transitions along decay chains of constant vibrational quantum number $v = n - \ell - 1$ until they reach states which rapidly ($\sim \text{ns}$) proceed to decay into $\bar{\text{pHe}}^{++}$ ions under emission of an Auger electron. The remaining ions are subject to collisional Stark effects such that prompt annihilations occur from states of small $\ell = \{0, 1, \dots\}$.

$\bar{\text{pHe}}^+$ atoms are readily synthesized when antiprotons are allowed to come to rest in helium targets. Once slowed down to electron-volt energies $\bar{\text{pHe}}^+$ atoms can be formed by atomic capture, where the antiproton replaces one electron of a helium atom. Theoretical models predict 15 – 30% of such formed $\bar{\text{pHe}}^+$ atoms to initially occupy metastable states of which most are of large $n \geq 41$. The resulting mean cascade lifetimes are therefore expected to be of order 5 – 7 μs . On the other hand only some $\sim 3\%$ of stopped antiprotons are experimentally observed to survive in helium targets with mean cascade lifetimes of $< 4 \mu\text{s}$. Laser spectroscopy experiments have revealed negligible populations in states of $n \geq 41$. This difference is conjectured to be due to collisional quenching, a hypothetical process which predicts the destruction of the $\bar{\text{pHe}}^+$ atom via electronically induced Stark mixings between metastable and short lived ℓ states. Collisional quenching is supposedly triggered by collisions of the $\bar{\text{pHe}}^+$ atom with one or more helium atoms from the dense target. Thus, one would naively expect the corresponding destruction efficiency to scale with the atomic collision rate in the helium medium, resulting in extended cascade lifetimes for measurements at reduced target densities. Previous experiments required targets of relatively high density in order to stop the $E_{kin} = 5.3 \text{ MeV}$ antiproton beam of the CERN Antiproton Decelerator. The construction of the Radio frequency quadrupole Decelerator (RFQD) which provides antiproton beams of kinetic energy $E_{kin} = 75 \text{ keV}$ has now enabled measurements in the very low density regime. In this work we report systematic cascade lifetime measurements of $\bar{\text{pHe}}^+$ atoms at the lowest density studied so far $\rho_L = 5 \times 10^{18} \text{ cm}^{-3}$. The results are compared to those from previous high density measurements and theoretical calculations. We found no significant difference in terms of cascade lifetimes as well as relative populations between measurements at low and high density. These results are discussed with regard to the $\bar{\text{pHe}}^+$ atom's formation model and collisional quenching effects.

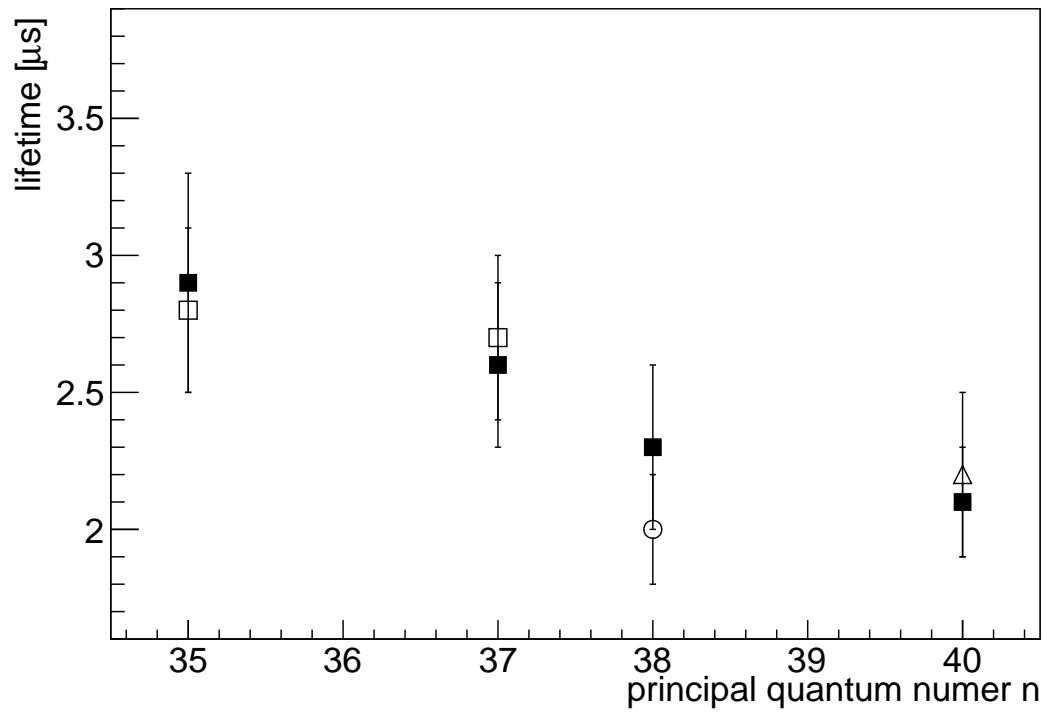


Figure 0.0.1: Cascade lifetime measurements compared at low (■) and high density (□,△,○). The measurements reported in this work show no significant change of the cascade state lifetimes within the experimental precision despite a 120 – 400 fold reduction in the target density down to $\rho = 5 \times 10^{18} \text{ cm}^{-3}$

Zusammenfassung

Metastabiles antiprotonisches Helium ($\bar{\text{pHe}}^+$) ist ein exotisches Atom, bestehend aus einem Heliumkern, einem Elektron im 1s Zustand sowie einem Antiproton in einem Rydberg-Zustand von großer Haupt- ($n \sim 38$) und Bahndrehimpulsquantenzahl ($\ell \sim n$). Aufgrund ihres großen ℓ -Wertes sind $\bar{\text{pHe}}^+$ Atome in metastabilen Zuständen stabil gegenüber dem schnellen ($\sim \text{ns}$) Augerzerfall. Stattdessen unterliegen sie langsamen ($\sim \mu\text{s}$) Strahlungsübergängen entlang von Zerfallsreihen mit konstanter Vibrationsquantenzahl $v = n - \ell - 1$ und zerfallen erst anschließend über den Augerzerfall in ein $\bar{\text{pHe}}^{++}$ Ion unter Emission eines Augerelektrons. In Kollisionen mit umliegenden Helium Atomen ist das entstehende Ion hierbei dem Starkeffekt ausgesetzt, derart, dass es von Zuständen mit kleinem $\ell = \{0, 1, \dots\}$ prompt annihiliert.

$\bar{\text{pHe}}^+$ Atome werden synthetisiert, wenn Antiprotonen in dichten Heliumtargets zur Ruhe kommen. Sobald diese bis auf Elektronvolt Energien verlangsamt sind, entstehen $\bar{\text{pHe}}^+$ Atome durch sogenannten "atomaren Einfang", ein Prozess, bei dem das Antiproton ein Hüllenelektron eines Heliumatoms ersetzt. Theoretische Modelle sagen voraus, dass 15 – 30% der so generierten $\bar{\text{pHe}}^+$ Atome metastabile Zustände besetzen, von denen die meisten $n \geq 41$ besitzen. Die daraus resultierende mittlere Kaskadenlebenszeit sollte daher 5–7 μs betragen. Entsprechende experimentelle Beobachtungen hingegen zeigen, dass nur $\sim 3\%$ der Antiprotonen mit mittleren Kaskadenlebenszeiten von $< 4 \mu\text{s}$ überleben. Laserspektroskopie Experimente haben darüber hinaus ergeben, dass Zustände mit $n \geq 41$ vernachlässigbar geringe Populationen aufweisen. Die Ursache zu der Diskrepanz zwischen Theorie und Experiment wird im "collisional quenching" vermutet, ein hypothetischer Prozess, bei dem das $\bar{\text{pHe}}^+$ Atom durch elektronisch induziertes Starkmixing zwischen metastabilen und kurzlebigen ℓ -Zuständen zerstört wird. Collisional quenching wird in Kollisionen des $\bar{\text{pHe}}^+$ Atoms mit umliegenden Heliumatomen ausgelöst, daher wäre naiv anzunehmen, dass die entsprechende Quenchingeffizienz mit der atomaren Kollisionsrate im Medium skaliert, was verlängerte Lebenszeiten bei geringen Targetdichten erwarten lässt. Vorherige Experimente benötigten relativ hohe Targetdichten, um die $E_{kin} = 5.3 \text{ MeV}$ Antiprotonen des CERN Antiproton Decelerators vollständig abbremsen zu können. Die Konstruktion des Radiofrequenzquadrupolentschleunigers (RFQD), welcher Antiprotonen mit $E_{kin} = 75 \text{ keV}$ bereitstellt, ermöglicht nun die Vermessung des Atoms bei niedrigen Targetdichten. In dieser Arbeit berichten wir über systematische Kaskadenlebenszeitmessungen des $\bar{\text{pHe}}^+$ Atoms bei den bisher niedrigsten gemessenen Targetdichten $\rho_L = 5 \times 10^{18} \text{ cm}^{-3}$. Wir vergleichen die Resultate mit denen von vorherigen Messungen bei hoher Dichte sowie zu theoretischen Berechnungen. Aus diesen Vergleichen ergeben sich keine Unterschiede in der Kaskadenlebenszeit und der Bevölkerungsverteilung bei niedriger gegenüber hoher Dichte. Wir diskutieren diese Erkenntnis mit Bezug zu $\bar{\text{pHe}}^+$ Entstehungsmodellen sowie zu collisional quenching.

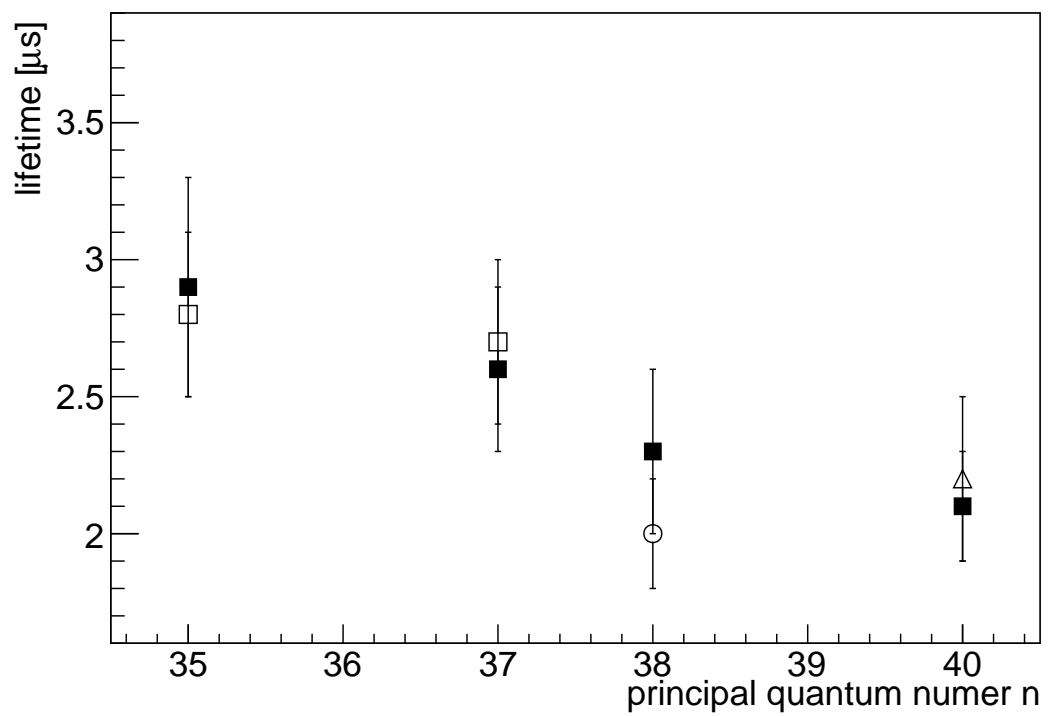


Figure 0.0.2: Vergleich von Kaskadenlebenszeitmessungen bei niedriger (\blacksquare) und hoher Targetdichte ($\square, \triangle, \circ$). Unsere Messungen zeigen keine signifikante Änderung in der Kaskadenlebenszeit trotz einer 120 – 400 fach reduzierten Targetdichte.

Contents

1	Antiprotonic Helium	1
1.1	History	1
1.2	$\bar{p}\text{He}^+$ properties	3
1.2.1	Structure	3
1.2.2	Auger decay	3
1.2.3	Radiative deexcitation	4
1.3	Theoretical description	6
1.4	$\bar{p}\text{He}^+$ formation	8
1.4.1	Naive approach	8
1.4.2	\bar{p} slow down and capture	9
1.4.3	Comparison to experimental results	11
1.5	Collisional Quenching	12
1.5.1	Hot $\bar{p}\text{He}^+$ collisional quenching	15
1.5.2	Cold $\bar{p}\text{He}^+$ collisional quenching	16
1.6	Investigation techniques	17
1.6.1	Delayed annihilation time spectrum (DATS)	17
1.6.2	Laser spectroscopy	18
1.6.3	$\pi^+ \rightarrow \mu^+ \rightarrow e^+$ background	20
1.7	Thesis objective	21
2	Numerical simulation of laser induced transitions	25
2.1	Laser power time profile	26
2.2	Relevant states and transitions	26
2.3	Initial populations	27
2.4	Rabi frequency	28
2.5	Optical Bloch equations	29
2.6	Computation	29
2.7	Results	30

3	Experimental setup	33
3.1	Antiprotons	34
3.1.1	Production target	34
3.1.2	The CERN AD	35
3.1.3	The ASACUSA RFQD	37
3.1.4	Low energy beam transport	38
3.2	Cryogenic target	39
3.2.1	Cold leak 2015	42
3.3	Detection system	43
3.4	Laser system	44
3.5	Hydrogen gas Raman shifter	47
3.5.1	Prior consideration	47
3.5.2	Design	51
4	Data analysis	55
4.1	Peak-to-total	55
4.1.1	Uncertainty to the ptt	56
4.1.2	Reproducibility of the ptt	57
4.2	Population evolution measurements	58
4.3	Offline antiproton shot rejection	59
4.4	Correlation of A_t to ptt	61
4.5	Cascade model	61
4.5.1	Extraction of cascade lifetimes	63
4.5.2	Reverse analysis	63
4.5.3	Extraction of capture probabilities	64
5	Results	65
5.1	Data taking	65
5.2	Comparison of signal strength	66
5.3	Population evolution measurements	67
5.3.1	$(n, \ell)=(40, 36)$; $\lambda = 1154$ nm	67
5.3.2	$(n, \ell)=(38, 35)$; $\lambda = 841$ nm	69
5.3.3	$(n, \ell)=(37, 35)$; $\lambda = 726$ nm	70
5.3.4	$(n, \ell)=(35, 33)$; $\lambda = 372$ nm	72
5.4	Relative capture probabilities for $v = 1, 2$	73
5.5	Summary	75
6	Discussions	77

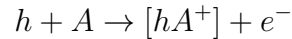
7 Outlook	79
A Formation models	81
A.1 Fermi Teller model (FTM)	81
A.2 Classical trajectory Monte Carlo calculation (CTMC)	82
A.3 Fermion molecular dynamics method (FMD)	82
A.4 Adiabatic Ionization model (AI)	83
A.5 Adiabatic hidden-crossing theory (AHC)	83
A.6 Diabatic state model (DS)	84
A.7 Time dependent scattering theory (TDST)	86
B Raman scattering	89
B.1 Induced polarization	90
B.2 Spontaneous Raman scattering	91
B.3 Stimulated Raman scattering	92
List of Acronyms	95
Bibliography	97

Chapter 1

Antiprotonic Helium

1.1 History

Since the 1950's and 60's experiments have studied how negatively charged hadrons such as π , κ or \bar{p} come to rest in matter. Bubble chambers revealed the associated lifetimes to be only \sim ps in matter and thus well below the respective value in vacuum, $\tau_{free} \gtrsim$ ns [1] [2]. This observation was explained by a model in which the negative hadron h is first slowed down before it undergoes what is called 'atomic capture'. This is a process in which h replaces one electron in a target atoms, forming a new neutral exotic atom:



This newly formed atom subsequently proceeds to annihilate via various cascade and quenching mechanisms. The timescale from capture to annihilation is of the order of ps and corresponds to the observed lifetime explaining $\tau_{matter} \approx$ ps \ll τ_{free} [3–5]. Already then Condo and Russel suggested that exotic helium atoms could under certain conditions be long lived i.e. $\tau_{He} \approx \tau_{free}$ [6–11].

Decades after the Condo-Russel prediction an experiment at the National Laboratory for High Energy Physics in Tsukuba Japan, KEK was carried out that had initially intended to search for the ${}^4_{\Sigma}\text{He}$ hypernucleus. Besides the successful discovery of the hypernucleus, the experiment found that 2% of incident kaons decayed with a lifetime of \sim 10 ns in helium, a value comparable to the lifetime of free kaons \sim 12 ns [12]. These results motivated a successor experiment at the Canadian National Laboratory for Particle and Nuclear Physics (TRIUMF - Tri University Meson Facility) with π^- mesons instead of kaons. Similar to the kaon experiment a fraction 2% of incidents pions were reported to decay with lifetimes $\tau \approx$ 10 ns [13].

The next step was to check if the observation could be reproduced with antiprotons. The antiproton \bar{p} , the antiparticle counterpart of the proton p , has charge: $q_{\bar{p}} = -q_p = -e$, mass: $m_{\bar{p}} = m_p \approx 1$ u and lifetime: $\tau_{\bar{p}} > 10^7$ yr [5]. In 1991 a dedicated experiment was carried out at KEK in which antiprotons were allowed to come to rest in gaseous, liquid and superfluid helium targets. These experiments observed $\sim 3\%$ of incident antiprotons to annihilate within lifetimes as long as few μs [14]. This so called 'longevity', was attributed to the formation of metastable antiprotonic helium atoms ($\bar{p}\text{He}^+$). These are neutral exotic atoms consisting of a helium nucleus, an electron in the ground $1s$ state, and an antiproton in a high lying Rydberg state of principal and angular momentum quantum numbers $n \sim \ell \sim 38$.

For the pursuit of more detailed studies the PS205 collaboration was founded at the European Laboratory for particle physics (CERN) in Geneva, Switzerland. In experiments at the Low energy antiproton ring (LEAR) the results observed at KEK were successfully reproduced. But in order to undoubtedly prove the existence of metastable antiprotonic helium atoms, laser spectroscopy experiments had to be carried out that could confirm its atomic structure. In 1993 the first transition was found after one week of scanning at the laser wavelength $\lambda = 597$ nm [15].

After the closure of the LEAR machine the antiprotonic helium experiment moved to the CERN Antiproton Decelerator (AD). Since the AD began routine operation in the year 2000 the ASACUSA collaboration (Atomic Spectroscopy and Collisions Using Slow Antiprotons) is carrying out laser spectroscopy experiments on antiprotonic helium atoms. As of today 32 transitions have been found. Among these a two photon transition has been measured with a fractional precision of $(2.3 - 5) \times 10^{-9}$ [16]. Comparisons between the measured frequencies and three-body QED calculations [17] have yielded the most precise value for the antiproton-to-electron mass ratio $1.836.1526736(23)$ [5]. Furthermore the study of the atom's initial populations has contributed to the theory of atomic capture [18]. In this thesis we investigate the population evolution of individual antiprotonic helium states in the low density regime. For this, new measurements at the lowest target densities studied so far $\rho = 5 \times 10^{18}$ cm^{-3} are compared to previous high density measurements. These results are discussed with respect to the atom's formation and quenching theory.

1.2 $\bar{\text{pHe}}^+$ properties

1.2.1 Structure

Customarily the $\bar{\text{pHe}}^+$ system is described in the so called atomic picture. Here the helium nucleus is taken to be stationary and orbited by the electron and the antiproton. The orbit of the electron can be approximated to be constant over the entire lifetime of the atom such the atomic state can be described by the associated principal and orbital angular momentum quantum number of the antiproton (n, ℓ) solely [19]. Obviously one prerequisite for metastability is a well localized antiproton orbit that possesses a finite distance to the nucleus, i.e (n, ℓ) must be sufficiently large. Antiprotonic states with orbits overlapping the nucleus on the other hand are subject to immediate annihilations via strong interaction and under isotropic emission of 4 – 5 light mesons, predominantly pions [20].

In Fig: 1.2.1 the energy level diagram according to this atomic picture is shown. To the right indicated by the solid and dotted lines the energy levels of the $\bar{\text{pHe}}^+$ atoms are shown, to the left indicated by the dashed lines the corresponding states of the $\bar{\text{pHe}}^{++}$ ion which is a hydrogenic two body system consisting of the antiproton and the helium nucleus only. One striking difference between the two systems is the ℓ degeneracy, which is removed by the presence of the electron in case of the atomic states but still in place for the ionized states. This fact makes $\bar{\text{pHe}}^{++}$ ions very prone to collisional stark mixings along ℓ states and thus leads to rapid annihilation when the antiproton is in a state of small orbital angular momentum ($\ell = 0, 1, \dots$) and thus overlaps with the nucleus [21].

1.2.2 Auger decay

Typically the dominant decay process for exotic atoms of high n and ℓ is the Auger process, a decay into the corresponding ion under the emission of an electron into the continuum:

$$[\bar{\text{pHe}}^+]_{n,\ell} \rightarrow [\bar{\text{pHe}}^{++}]_{n',\ell'} + e^- \quad (1.1)$$

A feature unique to "circular" $\bar{\text{pHe}}^+$ states, i.e. states with high principal and orbital quantum numbers $n \sim \ell - 1 \sim 38$, is their highly suppressed Auger decay rate γ^A . This is due to a strong dependence on the multipolarity exchange $\Delta\ell = \ell_{\text{initial}} - \ell_{\text{final}}$ and has been theoretically explained in Ref. [22, 23]. As a rule of thumb it can be assumed

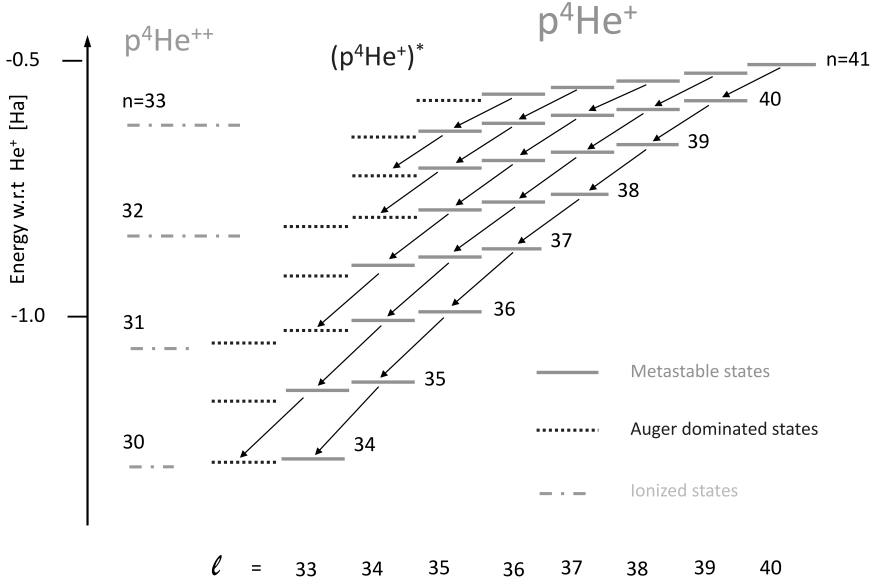


Figure 1.2.1: Energy level diagram in the atomic picture. $\bar{p}\text{He}^{++}$ ion states are denoted by the dashed line, neutral Auger dominated and metastable $\bar{p}\text{He}^+$ states by dotted and solid lines respectively. The presence of the electron removes the ℓ -degeneracy in case of atomic $\bar{p}\text{He}^+$ states.

that γ^A decreases by three orders of magnitude per unit increase in $\Delta\ell$ [24–26]

$$\gamma^A = 10^{17-3\Delta\ell} \text{ s}^{-1} \text{ for } \Delta\ell = 2, 3, 4 \quad (1.2)$$

States for which the angular momentum spacing to the next lower lying $\bar{p}\text{He}^{++}$ ion state $\Delta\ell$ is larger than three are therefore Auger suppressed with decay rates $\gamma^A \geq 10 \mu\text{s}^{-1}$. Adjacent states with $\Delta\ell \leq 3$ on the other hand have Auger decay rates of the order of $\sim \text{ns}^{-1}$. These states are termed metastable and Auger dominated and indicated by solid and dotted lines respectively in Fig. 1.2.1.

1.2.3 Radiative deexcitation

Metastable states primarily decay via radiative deexcitation. This is a transition into an energetically lower lying state under the emission of a photon.

$$[\bar{p}\text{He}^+]_{n,\ell} \rightarrow [\bar{p}\text{He}^+]_{n',\ell'} + \gamma \quad (1.3)$$

The lifetime of this decay is of order ($\tau^{\text{rad}} \sim \mu\text{s}$). Certain characteristics of radiative deexcitation can be best understood in the molecular picture. Here the system is regarded

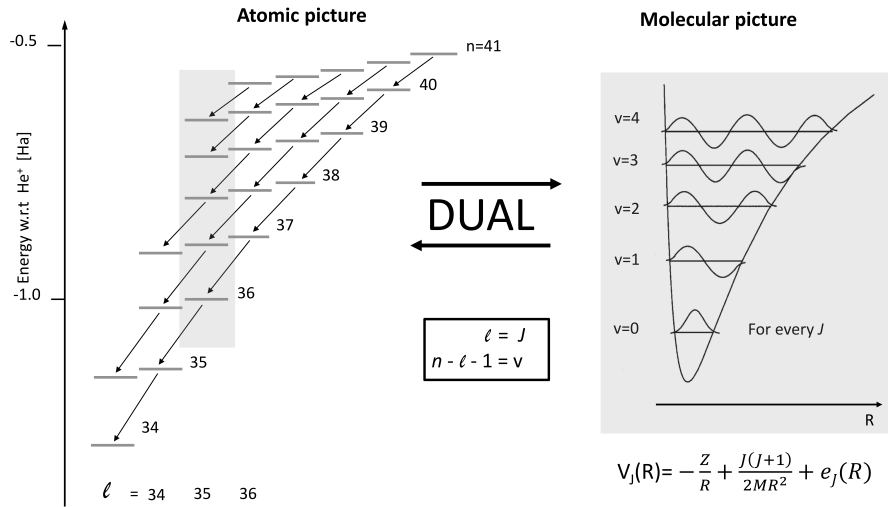


Figure 1.2.2: Comparison between atomic and molecular view of the $\bar{p}\text{He}^+$ system. In the molecular picture the new quantum numbers $J = \ell$ and $v = n - \ell - 1$ are introduced. For each J a Morse potential is obtained in which the vibrational states lie. Due to the propensity rules radiative transitions preferably occur along states of same v .

as a polar molecule with the antiproton being a negatively charged nucleus. Due to its much faster motion the electron is considered to adapt adiabatically to perturbations and the system is treated accordingly in the Born-Oppenheimer separation. In this picture the potential energy of the antiproton V is a function of its radial distance to the helium nucleus R . The rotational and vibrational quantum number $J = \ell$ and $v = n - \ell - 1$ are introduced such that the system's potential energy can be given [27]:

$$V(R) = -\frac{Z}{R} + \frac{J(J+1)}{2\mu^*R^2} + e_J(R) \quad (1.4)$$

where Z denotes the helium nucleus charge and μ^* the system's reduced mass. It is seen that for each rotational quantum number J a Morse potential has to be considered in which the vibrational eigenstates lie, see Fig. 1.2.2. The v quantum number also corresponds to the number of nodes of the wave function along R . Radiative deexcitation preferably takes place along transitions of constant v , following propensity rules of enhanced transition probabilities between states with the same number of nodes [27], a behavior that resembles the selection rules of simple diatomic molecules. Radiative decay chains along states of constant v are often called 'cascades' and always end in an Auger dominated states which promptly annihilate.

1.3 Theoretical description

Several theoretical approaches for the description of the $\bar{\text{p}}\text{He}^+$ atom have been suggested [22, 28, 29]. In the following we will discuss in more detail the method provided by Korobov as it has so far attained the highest precision in terms of energy levels, Auger and radiative decay rates [30].

In a first step a variational method is chosen to deal with the non-relativistic Hamiltonian of the system:

$$H = \frac{-1}{2\mu_{\alpha,\bar{\text{p}}}} \nabla_R^2 - \frac{1}{\mu_{\alpha,e^-}} \nabla_r^2 - \frac{m_{e^-}}{m_\alpha} \nabla_R \nabla_r - \frac{2}{r} - \frac{2}{R} + \frac{1}{|r-R|} \quad (1.5)$$

wherein $\mu_{ij}^{-1} = m_i^{-1} + m_j^{-1}$ are the associated reduced masses and R and r denote the position vectors of the electron and the antiproton respectively. Solution wavefunctions with the total angular momentum ℓ and projection to the Z-axis m to this Hamiltonian are of the type

$$\psi_l^m(R, r) = \sum_{\ell_{\bar{\text{p}}} + \ell_e = \ell} R^{\ell_{\bar{\text{p}}}} r^{\ell_e} \{Y_{\ell_{\bar{\text{p}}}} \otimes Y_{\ell_e}\}_{\ell m} G_{\ell_{\bar{\text{p}}}\ell_e}^\ell(R, r, \theta), \quad (1.6)$$

where $Y_{\ell_{\bar{\text{p}}}}$ and Y_{ℓ_e} are the spherical harmonics associated to the angular momentum of the $\bar{\text{p}}$ and e^- while $G_{\ell_{\bar{\text{p}}}\ell_e}^\ell(R, r, \theta)$ are functions that can be expanded as

$$G_{\ell_{\bar{\text{p}}}\ell_e}^\ell(R, r, \theta) = \sum_{i=1}^{\infty} C_i e^{-\alpha_i R - \beta_i - \gamma_i |R-r|}, \quad (1.7)$$

α_i , β_i and γ_i are pseudorandomly generated complex variables. It is now important to note that Auger-unstable states, defined above, are no real bound states but Feshbach resonances which break into subsystems within lifetimes ($\tau \leq 1$ ns). Their description with wavefunctions obtained in this way is therefore limited in accuracy to $\sim 10^{-4}$. To overcome this obstacle $\bar{\text{p}}\text{He}^+$ precision calculations therefore employ the complex coordinate rotation method (CCR) which embeds the resonance states into a continuum with a single normalizable wavefunction. For this a similarity operator $\hat{U}(a_d, \varphi)$ is introduced which rotates the coordinates in the complex plane

$$\hat{U} = a_d e^{i\varphi}, \quad (1.8)$$

where a_d and φ are both real and positive. The rotated Hamiltonian and wavefunctions are then of the type

$$H(a_d, \varphi) = \hat{U}(a_d, \varphi) H \hat{U}^{-1}(a_d, \varphi) \quad (1.9)$$

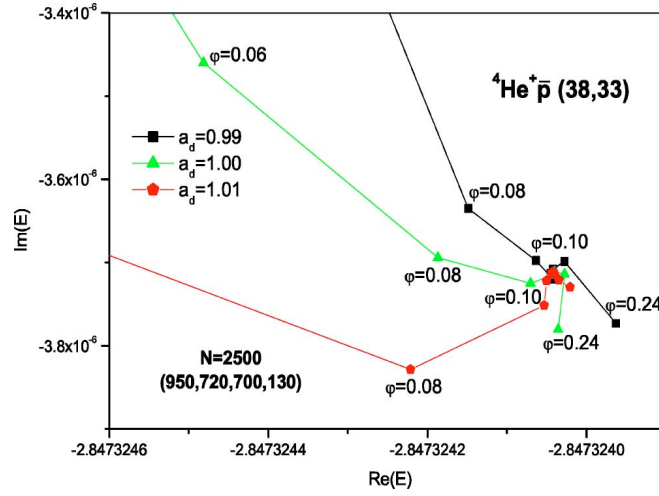


Figure 1.3.1: The complex energy converges towards a pole under variation of the scaling parameters a_d and φ . This figure is taken from Ref. [30] and illustrates the complex energy convergence for the $(n = 38, \ell = 33)$ state. In the calculation a set of 2500 basis functions was chosen.

and

$$\psi(a_d, \varphi) = \hat{U}(a_d, \varphi)\psi \quad (1.10)$$

The complex resonance energy E is then determined by the eigenvalue problem

$$(H(a_d, \varphi) - E)\psi(a_d, \varphi) = 0 \quad (1.11)$$

and a function of the scaling parameters a_d and φ . It is found that E converges under variation of these scaling parameters towards a resonant pole where $\partial E/\partial a_d = \delta E/\partial \varphi = 0$. At this pole the respective complex energy provides (i) the state's non-relativistic energy $E_{nr} = \Re(E)$ and (ii) its Auger decay rate $\gamma^A = -2\Im(E)/\hbar$. In Fig. 1.3.1 the convergence of the complex energy is graphically illustrated for the state $(n = 38, \ell = 33)$. Previous experiments have shown that measured and calculated Auger rates of agree within a precision of $< 30\%$ [31].

Given the CCR solution one can directly compute the radiative deexcitation rates using the obtained wavefunctions and perturbation theory

$$\gamma^{rad}(i \rightarrow f) = \frac{2\pi}{\hbar} |\langle i|H'|f\rangle|^2 \rho \quad (1.12)$$

where $\langle i|$ and $|f\rangle$ are the initial and final states, H' is the perturbed Hamiltonian and ρ is a phase space factor.

1.4 $\bar{p}\text{He}^+$ formation

1.4.1 Naive approach

Before dealing with the formation process of the $\bar{p}\text{He}^+$ atom in detail, we will consider a naive approach under a simplistic Bohr model. The $\bar{p}\text{He}^+$ atom will be treated in the atomic picture and taken to be a hydrogenic two body system. The helium nucleus and the electron are combined into an effective nucleus. The corresponding charge seen by the antiproton on its nearly classical trajectory is thus $Z_{\bar{p}}^{eff}$. In a first step we will introduce the antiproton's orbital radius $a_{\bar{p}}$

$$a_{\bar{p}} = \frac{m_e}{\mu^* Z_{\bar{p}}^{eff}} n^2 a_0 \quad (1.13)$$

and binding energy $B_{\bar{p}}$:

$$B_{\bar{p}} = (Z_{\bar{p}}^{eff})^2 \frac{\mu^*}{m_e} \frac{1}{n^2} R_{\infty} \quad (1.14)$$

where $(\mu^*)^{-1} = m_{\bar{p}}^{-1} + m_{\alpha}^{-1}$ denotes the reduced mass, $a_0 = 5.3 \times 10^{-11}\text{m}$ the Bohr radius and $R_{\infty} = 13.6\text{ eV}$ the Rydberg energy. Eq. 1.13 and 1.14 are to be compared to the electron's orbital radius and binding energy in the ordinary He atom:

$$a_e = \frac{1}{Z_e^{eff}} \cdot a_0 \quad (1.15)$$

and

$$B_e = (Z_e^{eff})^2 \cdot R_{\infty} \quad (1.16)$$

We now require the so called 'Massey resonance condition' which means maximal spatial and energetic overlap between the antiproton and the electron that is replaced

1. $B_{\bar{p}} \stackrel{!}{=} B_e$

2. $a_{\bar{p}} \stackrel{!}{=} a_e$

Inserting Eq. 1.14 - 1.15 into above, provides:

$$(Z_{\bar{p}}^{eff})^2 \frac{\mu^*}{m_e} \frac{1}{n_0^2} R_{\infty} = (Z_e^{eff})^2 R_{\infty} \quad (1.17)$$

which can be transformed to obtain the principal quantum number n_0 of the populated state:

$$\boxed{n_0 = \sqrt{\frac{\mu^*}{m_e}} \sim 38.2} \quad (1.18)$$

and

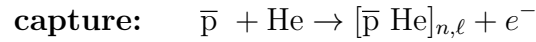
$$Z_{\bar{p}}^{eff} \approx Z_e^{eff} \approx 1.7 \quad (1.19)$$

for this particular orbital $n = n_0$

It is seen that Massey resonance condition in combination with a simplistic Bohr model already makes a concrete prediction concerning the antiproton orbit.

1.4.2 \bar{p} slow down and capture

At accelerator facilities antiprotons are typically available at kinetic energies in the keV–GeV range. This value greatly exceeds the characteristic energy scale for $\bar{p}\text{He}^+$ production which is the helium ionization potential $I_0 = 25$ eV. Experimentally $\bar{p}\text{He}^+$ atoms are produced by allowing fast antiprotons to come to rest in helium targets of sufficient density. Only when the antiprotons are slowed down to low enough energies they can undergo atomic capture. A full description of the $\bar{p}\text{He}^+$ formation process must therefore include the competition of both collision processes:



where $(\text{He})^*$ can be an ionized, excited or elastically recoiled He atom. The corresponding cross sections σ_{sd} and σ_{capt} are functions of the collision energy E_{coll} . Compelling information regarding the exact interplay between slow down and capture is contained in the primordial population distribution, i.e. the initial populations along states (n, ℓ) right after formation. The corresponding prediction of the primordial populations can therefore serve as an important check for any theoretical model.

Antiproton slow down

It was claimed by Cherepkov and Chernysheva that elastic scattering has a negligible contribution to σ_{sd} [32], so that stopping is dominated by events for which the antiproton's energy loss is independent of its incident energy. According to the theoretical considerations of Leon and Daniel this class of events should always produce a flat energy arrival distribution $F(E)$ in the relevant energy region; here

$0 < E_{kin} < I_0$, where $F(E)$ is defined such that $F(E)dE$ is the probability to find an antiproton within the energy range dE before it is captured [33] [34].

Antiproton capture

The theoretical description of atomic capture remains a topic of scientific debate for which various sophisticated models have been suggested. An overview of some of the most well known is given in Appendix A. In Fig. 1.4.2 we present the capture cross section σ_{capt} as a function of the collision energy E_{coll} calculated with some of these theoretical models. With the exception of the plane-wave Born model, they show reasonable agreement and all models exhibit two key features:

1. exponential decrease of σ_{capt} as a function of E_{coll}
2. significant deviation from this behavior at the helium ionization energy I_0 .

Assuming $\sigma_{capt} \approx 4a_0^2 = 10^8$ barn at $E_{coll} \approx I_0$ ¹ as well as a flat arrival distribution $F(E)$, we can conclude that a substantial fraction of $\bar{p}\text{He}^+$ atoms are produced by fast antiprotons with kinetic energies $T_{\bar{p}} \sim I_0$.

Another consistent characteristic of all models is the small kinetic energy of the ejected electron during atomic capture:

$$\boxed{T_e \approx 0}$$

This fact is due to the adiabaticity of the electrons, or in other words, the difficulty to transfer large amounts of energy and angular momentum via the Coulomb interaction within this system.

Energy considerations

These results can be evaluated with regard to the energy balance:

$$B^{n,\ell} = I_0 - T_{\bar{p}} \frac{m_{\text{He}}}{m_{\text{He}} + m_{\bar{p}}} + T_e$$

where $B^{n,\ell}$ is the $\bar{p}\text{He}^+$ binding energy. Under $T_e \approx 0$ and the consideration of $\sigma_{capt}(I_0) \gg 0$ two significant consequences arise: (i) fast antiprotons initially populate $\bar{p}\text{He}^+$ atoms in highly excited states ($n \geq 41$) (ii) these atoms experience large recoil momenta with $T_{\bar{p}\text{He}^+}$ up to 5 eV. It is essential to note that these conclusions arise from very basic assumptions and are shared by all models.

¹Correspond to a mean free path of 17 μm at target density $\rho = 5 \times 10^{18} \text{ cm}^{-3}$

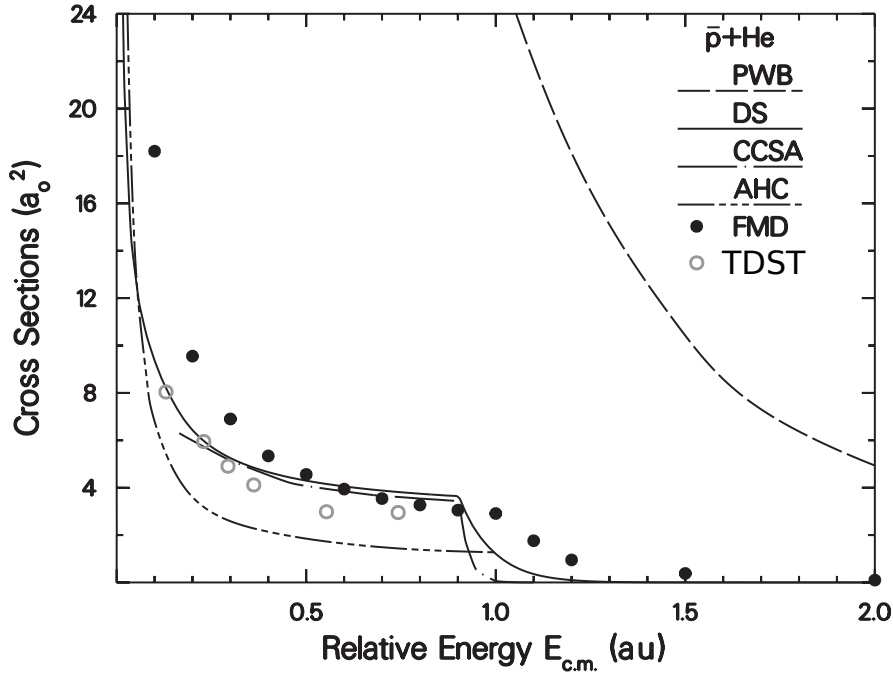


Figure 1.4.1: Capture cross section σ_{capt} as a function of collision energy E_{coll} in the center of mass frame as calculated by the different theoretical models presented: time-dependent scattering theory (TDST) [35], fermion molecular dynamics (FMD) [36], adiabatic hidden crossing theory (AHD) [37], coupled-channel semiclassical approximation (CCSA) [38], diabatic-state (DS) [39] and plane-wave Born (PWB) [40]. Figure taken from [41]

1.4.3 Comparison to experimental results

Via methods that will be discussed in Sec. 1.6 it is possible to obtain the population distribution around after atomic formation. In Fig. 1.4.2 the primordial populations along the principal quantum number n are shown for various v decay chains. The antiproton orbit with the highest population is the same as predicted by the Massey resonance condition $n_0 \approx \sqrt{\mu^*/m_e} \approx 38.2$. Besides the experimental values, theoretical predictions obtained by the diabatic and coupled-channel semi classical model are indicated. Theory and experiment agree well up to states with principal quantum number $n \approx 41$. However there is a significant discrepancy between the two in the higher n region. Various other experiments performed as of today give consistent results [18, 42, 43].

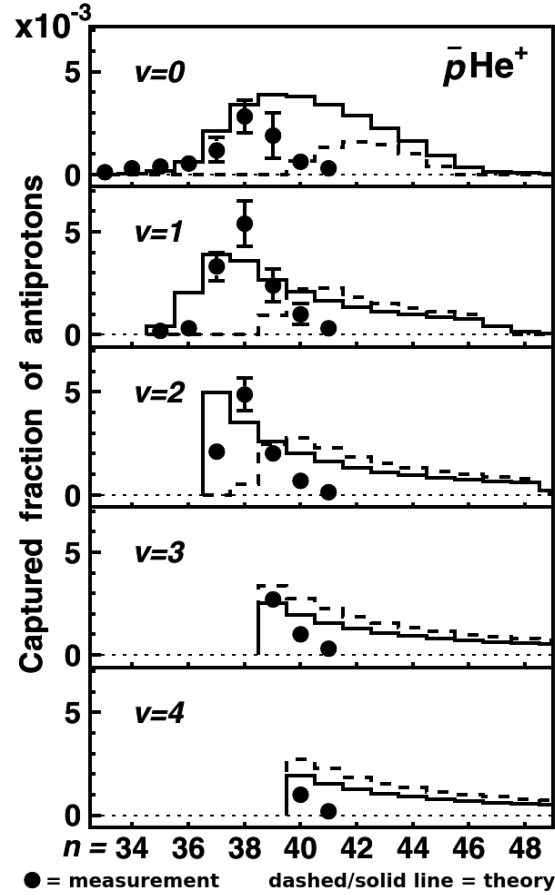
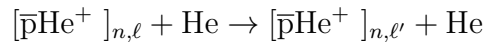


Figure 1.4.2: Primordial populations of $\bar{p}\text{He}^+$ atoms as a function of the principal quantum number n for different v decay chains. Experimental values are denoted by dots while theoretical calculations, i.e. the diabatic state [22] and semi classical couple-channel theory [44] are denoted by solid and dashed lines respectively. A discrepancy between theory and experimental values is present in $n > 41$ states. Figure from [18].

1.5 Collisional Quenching

Collisional quenching is a hypothesized process that could potentially explain the difference between theoretical predictions and experimental observations concerning the primordial populations of the $\bar{p}\text{He}^+$ atom. Collisional quenching is assumed to be due to the interaction between the $\bar{p}\text{He}^+$ and ordinary helium atoms in surrounding resulting in the $\bar{p}\text{He}^+$ atoms's destruction. The details to the process are under scientific debate while it has been suggested that because of the weak $\Delta E_{\ell,\ell'}$ splittings electronically induced Stark mixings redistribute the primordial ℓ populations homogeneously [45]



From Auger instable low $\ell=0, 1, \dots$ states the $\bar{\text{pHe}}^+$ atoms then proceed to annihilate as explained in Sec. 1.2. Suggested models however are constrained by the experimental observation that despite typical atomic collision frequencies $v_{coll} \sim 10^9 - 10^{13} \text{ s}^{-1}$ in dense helium media $\bar{\text{pHe}}^+$ atoms in states with $n \sim \ell \sim 38$ survive with μs lifetimes. In the following we present two models which differ in their initial theoretical approach but are both consistent with regards to these experimental observations. Interestingly, each of the two models motivates the distinction between two types of collisional quenching, depending on the underlying collision dynamics. At the end of these considerations we will discuss these two types with a focus on their experimental accessibility.

Sauge et. al addressed the collision problem in a molecular approach where the three nuclei ($\alpha - \bar{\text{p}} - \alpha$) are treated classically in a Born-Oppenheimer potential. The resulting interaction energy E_{int} expressed as a function of the internuclear distance R is then given as

$$E_{int} = E_{\text{He-}\bar{\text{pHe}}^+}(R) - E_{\text{He}} - E_{\bar{\text{pHe}}^+}$$

and comprises an effective activation barrier which 'protects' the antiproton, see Fig. A.6.1. The height of this activation barrier has a strong n dependence which is explained by the reduced Pauli shielding towards the tail of the $\bar{\text{pHe}}^+$ electron cloud. $\bar{\text{pHe}}^+$ atoms in the (38, 37) state e.g. were calculated to possess an activation barrier of height $\sim 2.2 \text{ eV}$ which is ~ 6 times larger than that of atoms in the (42, 41) [46]. The annihilation probability now depends on the underlying collision velocity v in the sense that the kinetic energy must be sufficiently high in order to overcome this activation barrier. Sauge et. al carried out simulations under utilization of the activation barrier approach using Monte-Carlo techniques. The corresponding results regarding the $\bar{\text{pHe}}^+$ atoms slowing down from $E_{kin} = 5 \text{ eV}$ to $\sim 80 \text{ meV}$ indicated the destruction of atoms in states across the atomic chart with particularly high efficiencies in the high n and low ℓ region [46].

In a second model Korenman directly calculated the quenching cross section σ_{cq} under utilization of the two-level Rosen-Zener-Demkov model. He discovered a very sensitive dependence of σ_{cq} on the so called Massey parameter $\eta_M = \Delta E_{\ell, \ell'} \times r / \hbar v$, where r is the radial distance between the antiproton and the α nucleus in the $\bar{\text{pHe}}^+$ atom [47]. The dependence on collision velocity v now allows to differentiate between

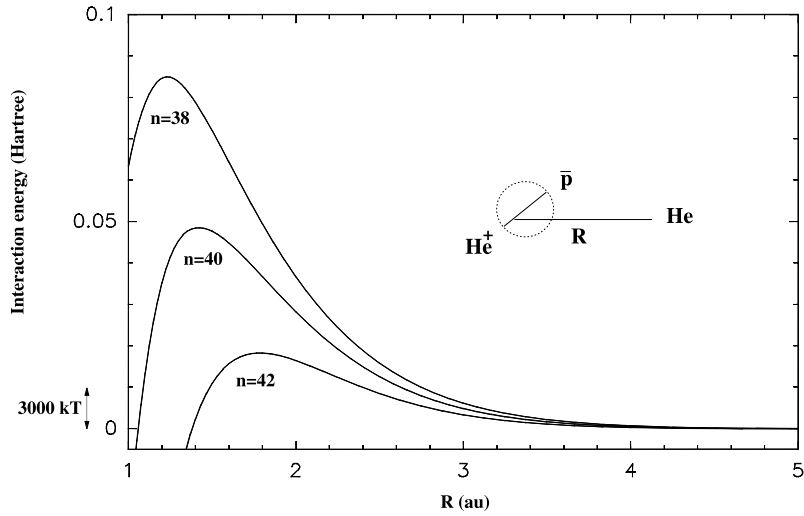


Figure 1.5.1: Interaction energy E_{int} between circular a $[\bar{\text{p}}\text{He}^+]_{n=\ell+1}$ and an ordinary helium atom. The resulting interaction forms an activation barrier which protects the antiproton. This activation barrier decreases for higher n states due to reduced Pauli shielding towards the tail of the electron cloud. Figure from [46].

two types of collisions

$$\sigma_{\text{quench}} = \begin{cases} \sim 0 & \text{for } v < v_{cr} \\ \sim \pi a_0/2 & \text{for } v \gg v_{cr} \end{cases}$$

distinguished by a critical value v_{cr} which is dependent on the atomic state (n, ℓ) of regarded $\bar{\text{p}}\text{He}^+$ atom. For circular states around $n \sim 38$ v_{cr} was calculated to be $\sim 6.3 \times 10^3$ m/s corresponding to a critical kinetic energy of the $\bar{\text{p}}\text{He}^+$ atom $T_{cr} \approx 1$ eV. Korenman then proceeded with a modified CCSA framework to compute the initial $\bar{\text{p}}\text{He}^+$ velocity distribution. The corresponding results were inserted into a collision model under direct employment of the obtained quenching cross section σ_{cq} . It was found that at least 80% of primordial states, in particular higher n states with $n > 40$, were nearly fully depleted. The thus populated region is indicated in Fig. 1.5.2 where the lines A, B and C denote the constraints from metastability, primordial population and hot collisional quenching [47].

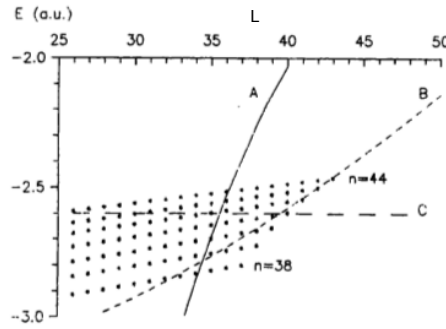


Figure 1.5.2: Populated region within the energy level diagram constrained by metastability (A), primordial population (B) and hot collisional quenching (C). Calculated for a helium target at standard pressure ($p = 1$ bar) and temperature ($T = 273.15$ K). Figure from [45]

Both discussed treatments are consistent with experimental observations in [18, 43]. Particularly noteworthy though is the fact that both predict a high sensitivity towards the involved collision velocity v . Moreover it needs to be considered that newly formed $\bar{\text{pHe}}^+$ atoms are expected to recoil with kinetic energies up to ~ 5 eV, see Sec. 1.4.2. The mean kinetic energy of $\bar{\text{pHe}}^+$ atoms in experimental targets with temperature $T \approx 1.5$ K on the other hand is small $E_{kin} \sim 10 \mu\text{eV}$. This difference motivates the distinction between two types of collisional quenching: (i) **hot $\bar{\text{pHe}}^+$ quenching** for the first set of collisions while the atom still possesses a relatively high recoil energy \sim eV (ii) **cold $\bar{\text{pHe}}^+$ quenching** for all collisions after the $\bar{\text{pHe}}^+$ atom is in thermal equilibrium with its ambient He atoms and thus $E_{kin} \approx \mu\text{eV}$.

1.5.1 Hot $\bar{\text{pHe}}^+$ collisional quenching

Hot $\bar{\text{pHe}}^+$ collisional quenching is closely related to the so called 'thermalization'. This is the first series of collisions subsequent to the $\bar{\text{pHe}}^+$ atoms formation through which it reaches thermal equilibrium with its environment. In cryogenic targets with $T \approx 1.5$ K thermalization of a $\bar{\text{pHe}}^+$ atom formed with $E_{kin} = 5$ eV comprises about 14 collisions corresponding to a time period of roughly 100 ps [19]. Only if the $\bar{\text{pHe}}^+$ atom is destroyed in these first few collisions one speaks of hot $\bar{\text{pHe}}^+$ collisional quenching. Although few in number these collision are expected to be particularly destructive such that both presented models expect hot $\bar{\text{pHe}}^+$ collisional quenching to be the main cause for the absence of $\bar{\text{pHe}}^+$ populations in the very high n region. Due to its short time scale and given the currently available accelerator technologies experimental access to this hypothesized phenomenon remains difficult.

1.5.2 Cold $\bar{p}\text{He}^+$ collisional quenching

Cold $\bar{p}\text{He}^+$ collisional quenching occurs only after thermalization has been completed. It is dependent on the target density as it directly scales with the underlying collision rate ν_{coll} . This dependence can be employed to access the contribution of cold $\bar{p}\text{He}^+$ collisional quenching in laser spectroscopy experiments so far. So far all experimental observations have indicated a strong suppression in this regard down to thermal collision frequencies $\nu_{coll} = 1.1 \times 10^9 \text{ s}^{-1}$ [18,19]. These observations are consistent with the presented models. Nevertheless it has also been claimed theoretically [48] and experimentally [49] that non negligible contributions from cold $\bar{p}\text{He}^+$ collisional quenching exist such that extended cascade lifetimes can be detected in experiments with target densities $\sim 1 \text{ mbar}$.

Besides said claims a density dependent lifetime shortening effect has been observed in one particular state. Laser spectroscopic studies revealed how the decay rate of the $(n = 37, \ell = 34)$ state increased nonlinearly with atomic density from $0.8 \mu\text{s}^{-1}$ at $\rho = 1.2 \times 10^{20} \text{ cm}^{-3}$ to $8 \mu\text{s}^{-1}$ at $\rho = 5.8 \times 10^{21} \text{ cm}^{-3}$. To date no satisfactory theoretical explanation for this phenomenon has been found [47,50].

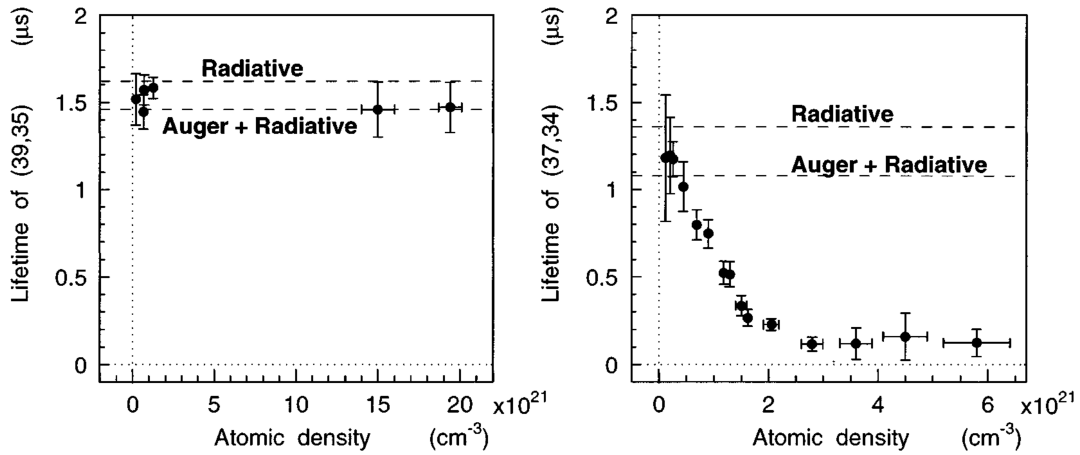


Figure 1.5.3: Measured lifetimes of the (39,35) and (37,34) state as a function of target density. Dots denote experimental values, dashed lines represent theoretical predictions [29]. (37,34) is the only state that showed a drastic density dependence. Figure from. [50]

1.6 Investigation techniques

1.6.1 Delayed annihilation time spectrum (DATS)

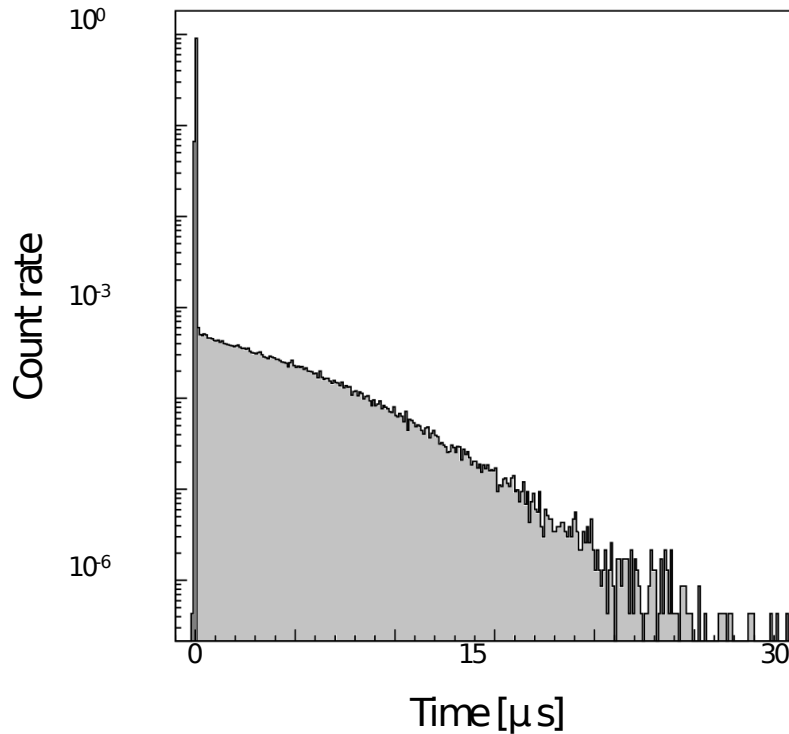


Figure 1.6.1: Time spectrum of antiproton annihilations in helium. 97% of the antiprotons annihilate within the first picoseconds, visible through the spike in the first bin, 3% survive for microseconds expressed in the long tail of the distribution. This behavior is explained by the formation of metastable antiprotonic helium atoms $\bar{p}\text{He}^+$. Fig. from [19]

Among the most common tools for the study of $\bar{p}\text{He}^+$ atoms is the delayed annihilation time spectrum (DATS) i.e. the annihilation count rate $\partial N/\partial t$ per unit time which is conveyed from the amount of emerging mesons that can be detected with particle counters, see Sec. 3.3. The DATS comprises two distinct features: (i) A sharp peak at $t = 0$ associated with all prompt annihilations, typically referred to as 'the prompt' and (ii) a long tail attributed to the formation of $\bar{p}\text{He}^+$ atoms in metastable states, called 'delayed component'. A typical DATS is shown in Fig. 1.6.1. The ratio between the 'delayed component' and the aggregate of all annihilations is referred to as trapping fraction f_{trap} and turns out to be to some extent sensitive to the target density such that $f_{trap} = 2.4\%$ and 3% at $\rho = 2.4 \times 10^{26} \text{ cm}^{-3}$ and $\rho < 10^{20} \text{ cm}^{-3}$ respectively [19]. The very shape of the delayed component is determined by the convoluted populations and lifetimes of all metastable states. Since pieces of information in the DATS regarding

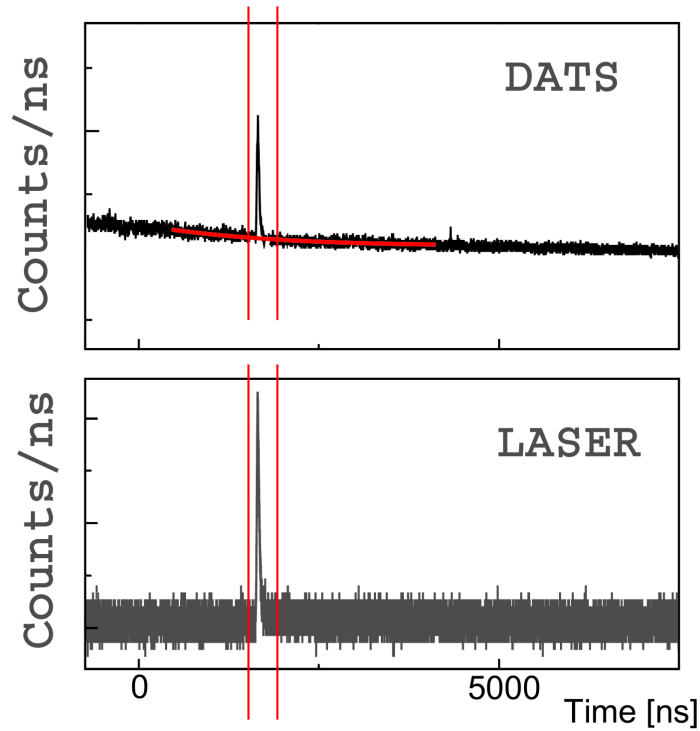


Figure 1.6.2: Annihilation time spectrum and laser time profile respectively. A laser beam causes a sharp increase in the annihilation count rate $\frac{\partial N}{\partial t}$. The integral of the induced peak relative to the delayed component is used as a bunch intensity corrected measure for the signal strength.

the individual cascades cannot be easily disentangled, the DATS does not allow for state selective studies of $\bar{p}\text{He}^+$ atoms. This is why the DATS alone is unsuited for the investigation of state dependant populations and lifetimes.

1.6.2 Laser spectroscopy

Laser spectroscopy experiments are sensitive to atomic structures and have proven to be a powerful tool for the investigation of $\bar{p}\text{He}^+$ atoms. When applied to ordinary atoms laser spectroscopy experiments most commonly employ the detection of: (i) fluorescent radiation of excited atoms, (ii) resonant absorption of laser photons or (iii) photoelectrons following multi-photon ionization. The fact that $\bar{p}\text{He}^+$ atoms are typically produced in very small numbers $\rho_{\bar{p}\text{He}^+} \leq 10^4 \text{ cm}^{-3}$ embedded in much denser helium media $\rho_{\text{He}} \geq 10^{18} \text{ cm}^{-3}$ makes all these methods unsuitable for laser spectroscopy. It has however proven possible to utilize the ≥ 1000 fold difference in lifetime between certain $\bar{p}\text{He}^+$ states for laser spectroscopy. In Sec. 1.2.1 we discussed how the atomic states of the $\bar{p}\text{He}^+$ atom can be classified into two groups

1. metastable states with lifetimes $\tau_m \approx \mu\text{s}$
2. Auger dominated states with lifetimes $\tau_m \approx \text{ns}$

If a resonant laser field now stimulates population transfer from a metastable to an Auger dominated state this results in an instantaneous ($\sim \text{ns}$) increase of the annihilation count. These so called 'forced annihilations' are then seen in form of a sharp spike in the DATS as shown in Fig. 1.6.2 and are always in time coincidence with the laser pulse. The area under the peak is identified with the signal representing a measure for the population transfer. It is further common to normalize this value against the aggregate of all annihilation contained in the delayed component to correct for shot-to-shot fluctuations in the antiproton beam. The resulting quantity is referred to as 'peak-to-total' (*ptt*) and will be used as the measure for the signal strength in this work.

According to the selection rules two different types of E1 transitions between metastable and Auger dominated states are allowed. The two types are distinguished by the change in the vibrational number Δv and dipole moment μ .

- *favoured* transitions: $\Delta v = 0$; $(n, \ell) \leftrightarrow (n - 1, \ell - 1)$; $\mu \approx 0.2 - 0.3$ Debye
- *unfavoured* transitions: $\Delta v = 2$; $(n, \ell) \leftrightarrow (n + 1, \ell - 1)$; $\mu \approx 0.02 - 0.03$ Debye

(i) Resonance profile measurements

We distinguish between two different classes of $\bar{\text{p}}\text{He}^+$ laser spectroscopy experiments in which either the laser timing is fixed and the frequency scanned or vice versa. The two classes address complementary physics questions. The atom's characteristic 'resonance profiles' are obtained in the first class of experiments, where peak-to-total is measured against the laser frequency. The profile shape and position in the frequency domain can then be compared to corresponding theoretical calculations to make physics statements e.g. regarding the antiproton's mass relative to that of the electron. The precision in these experiments is predominantly limited by thermal Doppler-broadening resulting from the $\bar{\text{p}}\text{He}^+$ atom's finite temperature. This is why $\bar{\text{p}}\text{He}^+$ laser spectroscopy experiments are routinely performed at cryogenic temperatures². The most precise measurements have been achieved under the employment of the so called two photon scheme. Here the transition is induced by two counter-propagating laser beams such that their relative Doppler-shifts partially cancel each other out. The most precise measurement to this date yielded $m_{\bar{\text{p}}}/m_e$ to be 1836.1526736(23) [16].

²Note: the full width half maximum of the Doppler width is proportional to the square root of the temperature $\Delta f \propto \sqrt{T}$

Population evolution measurements

Questions regarding populations, lifetime and quenching are typically addressed in the second class of laser spectroscopy experiments, where the peak-to-total is measured against the laser timing at fixed laser frequencies. In this way one measures the relative population in corresponding parent state (n, ℓ) as a function of time i.e. the state's population evolution. This value can then be inserted into $\bar{\text{p}}\text{He}^+$ cascade models providing the state's cascade lifetime which is the effective lifetime under which the population in regarded state decays. Cascade lifetimes of metastable $\bar{\text{p}}\text{He}^+$ states are generally determined by (i) their depletion due to radiative and Auger deexcitation (ii) their feeding from higher lying states (iii) the destruction of the atom e.g. triggered by collisional effects. Thus, the cascade lifetime of a given state is not only sensitive towards collisional effects in that particular state but also in higher lying states of the respective decay chain.

1.6.3 $\pi^+ \rightarrow \mu^+ \rightarrow e^+$ background

It is important to note that $\bar{\text{p}}\text{He}^+$ experiments using pulsed antiproton beams are inherently subject to a strong $\pi^+ \rightarrow \mu^+ \rightarrow e^+$ background [42]. Low energy pions emerging from antiproton annihilations stop in the target walls or the detector, from there they decay into muons, which further decay into positrons with a lifetime $\tau_\mu = 2.2\mu\text{s}$. When these positrons strike the detector a fake signal is created³. Given the analogue nature of the used detectors it is however not possible to distinguish regarded background from the signal produced by the annihilation of metastable $\bar{\text{p}}\text{He}^+$ atoms. An estimation however for a similar setup was determined in Ref. [51], where the DATS generated by a pulsed antiproton beam was compared to one obtained in a continuous beam experiment at comparable target and laser conditions. The continuous beam experiment now allowed for the rejection of the $\pi^+ \rightarrow \mu^+ \rightarrow e^+$ events by requiring that two or more pions were detected. In a comparison of the DATS obtained in the pulsed and continuous beam experiment it was found that the $\pi^+ \rightarrow \mu^+ \rightarrow e^+$ background constitutes $\sim 50 - 60\%$ of full delayed component. This results was also consistent with accordingly performed Monte Carlo simulations. For the experimental setup of this work no comparative measurement with a continuous antiproton beam has ever been performed which is why the $\pi^+ \rightarrow \mu^+ \rightarrow e^+$ background of our setup is relatively poorly understood. The determination of the trapping fraction

³It is interesting to note that due to their large atomic capture cross section π^- mesons do not contribute to this type of background

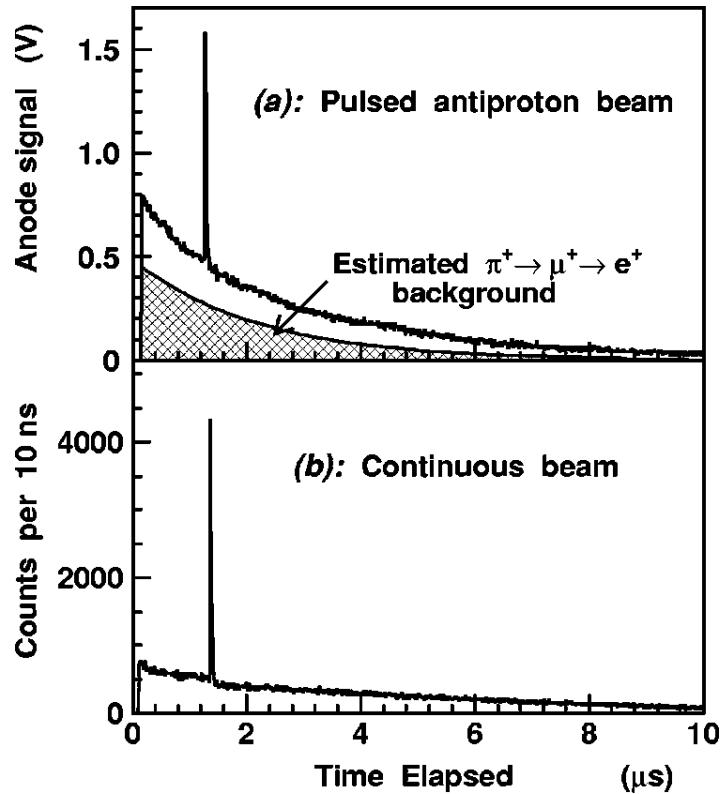


Figure 1.6.3: Delayed annihilation time spectrum measured with (a) a pulsed and (b) a continuous antiproton beam. Both spectra were obtained under the same target and laser condition, in particular the spikes at $1.6 \mu\text{s}$ refer to the same laser induced transition. The hatched area in the upper plot denotes the estimated contribution due to $\pi^+ \rightarrow \mu^+ \rightarrow e^+$ -decay.

f_{trap} from the DATS suffers inherently from this uncertainty.

1.7 Thesis objective

The objectives of this thesis are: (i) execute population evolution measurements at the lowest target densities and collision frequencies studied so far (ii) compare the results to those obtained in higher density experiments as well as to theoretical calculations (iii) investigate the hypothesis whether *cold $\bar{p}\text{He}^+$ collisional quenching contributes substantially to the destruction of $\bar{p}\text{He}^+$ atoms above within the studied density regime*

The rate of cold $\bar{p}\text{He}^+$ collisional quenching scales with the atomic collision frequency ν_{coll} . If the cold $\bar{p}\text{He}^+$ collisional quenching is a dominant mechanism in the destruction of $\bar{p}\text{He}^+$ atoms, particularly in the very high n region, then a reduction in

the target density and thus the atomic collision frequency will result in

1. altered population evolutions because of a modified population distribution
2. enhanced cascade lifetimes due to delayed feeding from the very high n region
3. a shift in the initial population distribution

In this work we report population evolution measurements of four states distributed over the metastable region of the atomic chart, see Table 1.1 and Fig. 1.7.1. These measurements were carried out at $\rho = 5 \times 10^{18} \text{ cm}^{-3}$ corresponding to $\nu_{coll} = 5 \times 10^5$ Hz at $T = 1.5$ K, which is 120 – 400 times lower than previous experiments in terms of target density and 240 – 800 times in terms of atomic collision frequency. We compare these results to previous high density measurements with particular focus on correspondingly extracted cascade lifetimes and relative initial populations.

Three of the studied states were chosen such that they represented the highest excited states probed previously in the $v = 1, 2$ and 3 decay chain respectively. These states promise to be the most sensitive access to potential density effects in the very high n region. Previous investigations of the $(40, 36)$ state, measured under the 1154 nm transition have revealed negligible populations in the respective decay chain above $n = 40$ at $\rho = 1 \times 10^{21} \text{ cm}^{-3}$ [43]. The state $(38, 35)$ is the highest lying state in the $v = 2$ decay chain for which population evolution measurements have previously been carried out. We probed this state employing the $(38, 35) \rightarrow (39, 34)$ transition at $\lambda = 841$ nm which unlike previously used transitions, allows measurements at very low densities. Within the $v = 1$ decay chain which is known to comprise the largest fraction of primordial $\bar{\text{p}}\text{He}^+$ atoms we measured population evolutions in the $(37, 35)$ and $(35, 33)$ state. These two are the highest and lowest lying state of with $v = 1$ for which measurements have previously been carried out [18]. The corresponding transitions were $(37, 35) \rightarrow (38, 34)$ at $\lambda = 726$ nm and $(35, 33) \rightarrow (34, 32)$ at $\lambda = 372$ nm. In a combined analysis it will be possible to give the relative initial populations within this decay chain.

In **Chapter 2** we present simulations that were carried out to estimate the required laser power for the efficient depopulation of the parent states. In these we numerically solve corresponding optical Bloch equations. A description of the experimental apparatus is given in **Chapter 3**. This includes the CERN antiproton decelerator and the ASACUSA radio frequency quadrupole decelerator which serve as the source for low energy antiprotons, the cryogenic low density helium target, the detection system

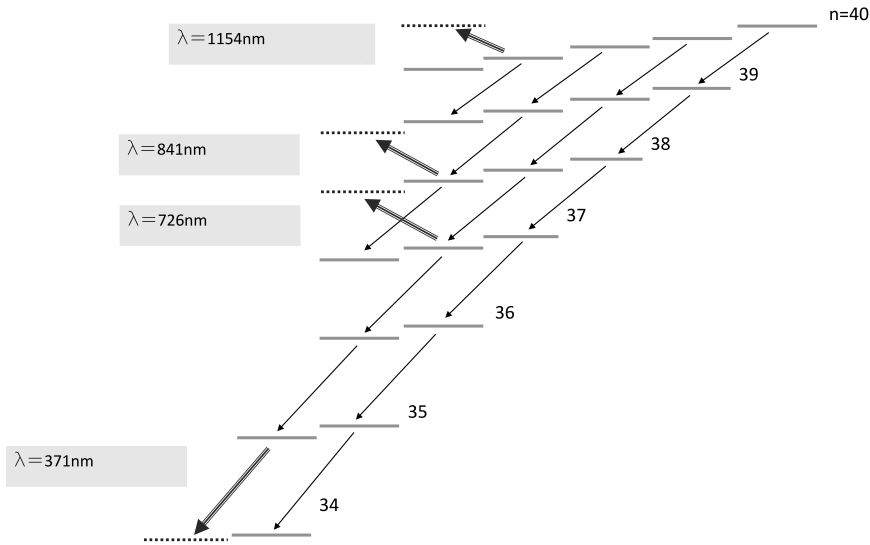


Figure 1.7.1: Four transitions spread over the principal $n = 35 - 40$ and vibrational quantum numbers $v = 1 - 3$ were studied. Three of the chosen transitions represented the highest lying state of their respective decay chain that had previously been measured at higher density. These transitions are particularly sensitive to possible populations in the very high n region. The fourth transition probes the lower n region.

Table 1.1: List of investigated transitions

transition	decay chain v	transition wavelength λ
$(40, 36) \rightarrow (41, 35)$	3	1154 nm
$(38, 35) \rightarrow (39, 34)$	2	841 nm
$(37, 35) \rightarrow (38, 34)$	1	726 nm
$(35, 33) \rightarrow (34, 32)$	1	372 nm

consisting of acrylic Cherenkov counters read out by fine-mesh photomultiplier tubes, the injection seeded Ti:Sapphire laser system generating high power narrow linewidth laser pulses. Within the laser system we describe in more detail the multi-pass hydrogen Raman-cell for wavelength shifting towards the IR. The performed data analysis including the underlying uncertainty calculation is explained in **Chapter 4**. In **Chapter 5** we present the results of this work which are the measurement of four population evolutions and relative populations at the lowest target density studied so far. The results are compared to previous measurements at high target density as well as to theory. In **Chapter 6** we discuss the results in terms of their implication towards presented quenching models. Finally in **Chapter 7** this work is put into the context of future projects and provide an outlook with regard to the CERN ELENA upgrade.

Chapter 2

Numerical simulation of laser induced transitions

We estimated the laser induced depopulation efficiency ϵ for the four transitions, where we defined $\epsilon = 1$ when all antiprotons in the parent state (n, ℓ) annihilated and $\epsilon = 0$ when none did so. For this we solved the optical Bloch equations in the conventional semiclassical picture, where a quantum mechanical two state system is regarded under the influence of a strong periodic laser field. The following effects were included: (i) individual transition frequencies and dipole moments between all hyperfine substates, (ii) dephasing terms due to Auger and radiative decay (iii) collisional dephasing, (iv) inhomogeneous Doppler broadening, (v) the laser field time profile.

The simulations comprised the following steps:

1. Approximation of the laser power profile
2. Identification of the relevant atomic states and transitions
3. Estimation of the initial populations
4. Calculation of the time dependent Rabi frequencies $\Omega_{m,m'}(t)$
5. Numerical computation of the Optical Bloch equations

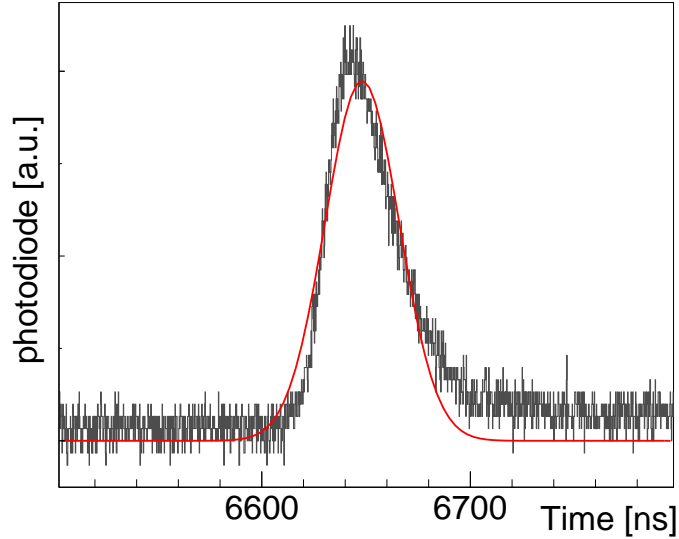


Figure 2.1.1: The laser pulse time profile compared to the Gaussian approximation used in the simulations.

2.1 Laser power time profile

For simplicity we assumed the laser beam to have a Gaussian temporal and flat-top spatial intensity profile such that the power seen by the $\bar{\text{p}}\text{He}^+$ atoms was of form

$$\vec{\theta}(t) = \vec{\theta}_0 \exp\left(4 \ln(2) \left(\frac{t}{2\delta_t}\right)^2\right) \quad (2.1)$$

where δ_t is the FWHM of the time profile and θ_0 the the peak power. For every studied transition the laser pulse length and energy were measured . In Fig. 2.1.1 the temporal profile of the laser pulse as recorded with a 1.5 GHz bandwidth p-i-n photodiode is compared to our Gaussian approximation. For the purpose of this simulations this rough approximation was sufficient.

2.2 Relevant states and transitions

In the discussions in Chapter 1 it was sufficient to describe the $\bar{\text{p}}\text{He}^+$ atom solely by the principal and orbital angular momentum quantum number of the antiproton (n, ℓ) . The quantitative computation of transitions probabilities however requires the consideration of all hyperfine substates i.e. (i) the coupling of the orbital angular momentum ℓ with the electron spin S_e to J (ii) the coupling of J with the antiproton spin $S_{\bar{\text{p}}}$ to F (iii) the magnetic quantum number of the atom m_F ranging from $-F$ to

Table 2.1: Hyperfine substates for given (n, ℓ) shown from top to bottom descending in energy.

state	J	F
$ - + \rangle$	$L - 1/2$	$F + 1/2$
$ - - \rangle$	$L - 1/2$	$F - 1/2$
$ + + \rangle$	$L + 1/2$	$F + 1/2$
$ + - \rangle$	$L + 1/2$	$F - 1/2$

F . In the absence of a magnetic field all m_F substates were energetically degenerate such that for each combination (n, ℓ) we considered four hyperfine substates, referred to in their ket notation as $|n, \ell, J, F, m\rangle$. It should be noted that contrary to the case of hydrogen $\bar{\text{p}}\text{He}^+$ states with $J = L - 1/2$ lie higher in energy than $J = L + 1/2$. This is due to the negative nuclear moment of the antiproton. A break down of the four hyperfine substates is given in Table 2.1 in energetical order.

For given initial state (n, ℓ) and final state (n', ℓ') one thus obtains eight allowed E1 transitions, of which four comprise a spin-flip of either the electron or the antiproton, see Fig. 2.2.1. Due to the odd parity of the spin wave functions these spin-flip transitions are highly suppressed and were therefore neglected in our considerations. This reduced the number of relevant transitions to four [52].

2.3 Initial populations

The hyperfine substates give rise to the splitting of the transition frequency. In case of the transitions at 726 nm and 841 nm the reported splitting (~ 1.7 GHz) is significantly larger than our laser line width ~ 100 Hz and the expected Doppler width ~ 200 MHz [53]. For this reason we assumed that here only half the parent state population contributes to the laser induced transitions. The other two transitions at 372 nm and 1154 nm on the other hand are known to have large natural width with respect to the corresponding splittings [43, 54, 55]. Thus, we assumed that here the full parent state population contributed to the transition here.

Furthermore we took all possible $|m_F\rangle$ substates to be equally populated upon laser beam arrival and all $\bar{\text{p}}\text{He}^+$ atoms to be subject to a Maxwell Boltzmann velocity distribution corresponding to an ensemble temperature of $T = 1.5$ K.

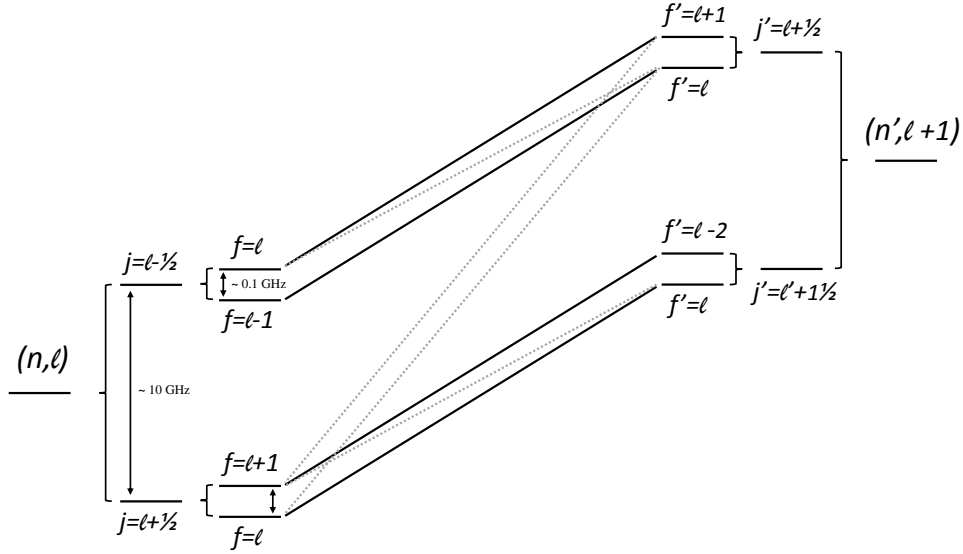


Figure 2.2.1: Given the initial (n, ℓ) and final state (n', ℓ') there exist eight E1 transitions between the associated hyperfine substates. Four of these comprise a spin-flip of either the electron or the antiproton, shown by gray dotted lines. These are highly suppressed due to symmetry considerations.

2.4 Rabi frequency

The Rabi frequency $\Omega_{m,m'}(t)$ characteristic to the effective oscillations between corresponding states $|n, \ell, J, F, m\rangle$ and $|n', \ell', J', F', m'\rangle$ is defined as:

$$\Omega_{m,m'}(t) = \frac{\langle \mu \rangle E(t)}{\hbar} \quad (2.2)$$

where $E(t)$ is the electric field and $\langle \mu \rangle$ the E1 transition dipole moment defined for the respective pair of initial and final state

$$\langle \mu \rangle = \langle n', \ell', J', F', m' | \mu | n, \ell, J, F, m \rangle \quad (2.3)$$

Using the Wigner-Eckhardt theorem it can be decomposed to [17]

$$\begin{aligned} \langle n', \ell', J', F', m' | \mu_D | n, \ell, J, F, m \rangle = & (-1)^{F'+m} \langle n', \ell' | \mu_D | n, \ell \rangle \begin{pmatrix} F & 1 & F' \\ m & 0 & m \end{pmatrix}_{3j} \\ & \times \sqrt{(2F+1)(2F'+1)} \left| \begin{pmatrix} J' & F' & 1/2 \\ F & J & 1 \end{pmatrix}_{6j} \right| \\ & \times \sqrt{(2J+1)(2J'+1)} \left| \begin{pmatrix} \ell' & J' & 1/2 \\ J & \ell & 1 \end{pmatrix}_{6j} \right| \end{aligned} \quad (2.4)$$

where $\langle n', \ell' | \mu_D | n, \ell \rangle$ is the reduced transition dipole moment and can itself be expressed as [42]

$$\langle n', \ell' | \mu_D | n, \ell \rangle = 1.8 \sqrt{2\ell + 1} \sqrt{\frac{\lambda^3}{\tau}} \times 10^6 \text{ (in Debye)} \quad (2.5)$$

with λ being the transition wavelength (in nm) and $1/\tau$ the spontaneous radiative decay rate.

2.5 Optical Bloch equations

The optical Bloch equations of the regarded two state system can be formulated in the density matrix formalism:

$$\frac{d}{dt} \begin{pmatrix} \rho_m^p \\ \rho_{m'}^d \\ \rho^x \\ \rho^y \end{pmatrix} = \begin{pmatrix} -1/\tau_p & 0 & 0 & 1/2\Omega_m(t) \\ 0 & -1/\tau_d & 0 & 1/2\Omega_m(t) \\ 0 & 0 & -1/2(1/\tau_p + 1/\tau_d) - \Gamma & \Delta\omega \\ -\Omega_m(t) & \Omega_m(t) & -\Delta\omega & -1/2(1/\tau_p + 1/\tau_d) - \Gamma \end{pmatrix} \begin{pmatrix} \rho_m^p \\ \rho_{m'}^d \\ \rho^x \\ \rho^y \end{pmatrix} \quad (2.6)$$

where ρ_m^p and $\rho_{m'}^d$ denote the populations of the parent and daughter state and ρ^x and ρ^y the off diagonal entries, τ_p and τ_d are the parent and daughter state lifetimes, Γ the collisional dephasing rate, $\Delta\omega$ the detuning of the laser frequency with respect to the rest frame transition frequency $\Delta\omega = \omega_{Las} - \frac{E_f - E_i}{\hbar}$ and $\Omega_{m(t)}$ the Rabi frequency as introduced above.

2.6 Computation

The optical Bloch equations were solved numerically using a 4th-order Runge-Kutta method. The populations of parent and daughter states were evaluated in steps of 20 ps. The daughter state lifetime τ_d dominated by the Auger decay and the parent state lifetime τ_p dominated by radiative deexcitation were taken from [25, 56] and [18, 43]. No experimental data for the dephasing rate Γ exists which is why we used theoretical values from [57]. Consistent with the discussion in Sec. 1.2 we considered the number of Auger decayed $\bar{\text{pHe}}^+$ atoms to be equal to the number of annihilations. The depopulation efficiency ϵ is therefore defined as

$$\epsilon = 1 - \frac{\rho_p(t = T) + \rho_d(t = T)}{\rho_p(t = 0) + \rho_d(t = 0)} \quad (2.7)$$

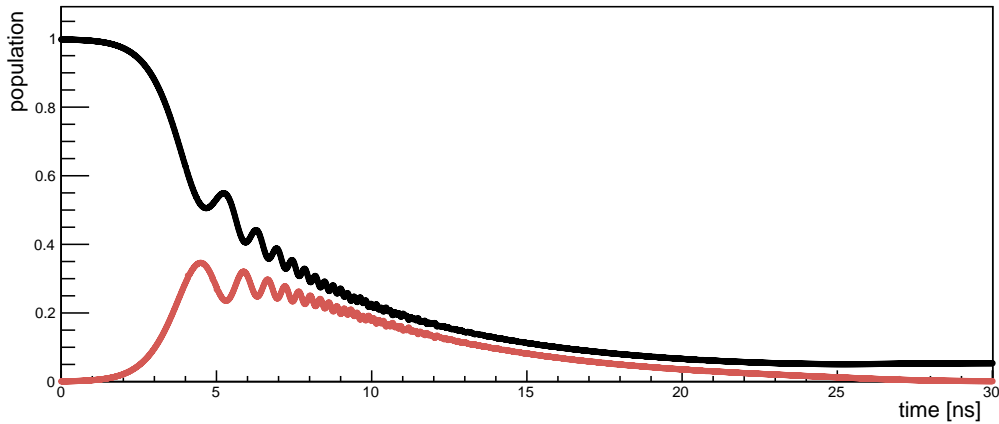


Figure 2.6.1: Population transfer illustrated

A typical time evolution spectrum of both states is illustrated in Fig. 2.6.1 comprising characteristic Rabi oscillations between the two respective populations. The fast Auger rate $\sim 10^9 \text{ s}^{-1}$, results in a damping of the oscillations and decay of the daughter state population towards the end of the spectrum.

2.7 Results

The results of our simulation are displayed in Fig. 2.7.1. Here the depopulation efficiency is plotted as a function of the laser pulse energy density. The simulation parameters are summarized in Table 2.2 where the pulse lengths δ_t were chosen to represent experimentally feasible values. Due to its relatively large transition dipole moment of $\langle \mu \rangle = 0.361 \text{ D}$ the favored transition at wavelength $\lambda = 372 \text{ nm}$ could be efficiently depopulated already at low energy densities. The unfavored transitions at 726 nm and 841 nm had considerably smaller dipole moments, which is why larger energy densities were required to depopulate them. On the other hand their large hyperfine splittings reduced the accessible parent state population and thus the depopulation efficiency in the considered states by half. The IR transition at 1154 nm is of unfavored type too but could well be depopulated due to its large natural width with respect to its hyperfine splitting [43].

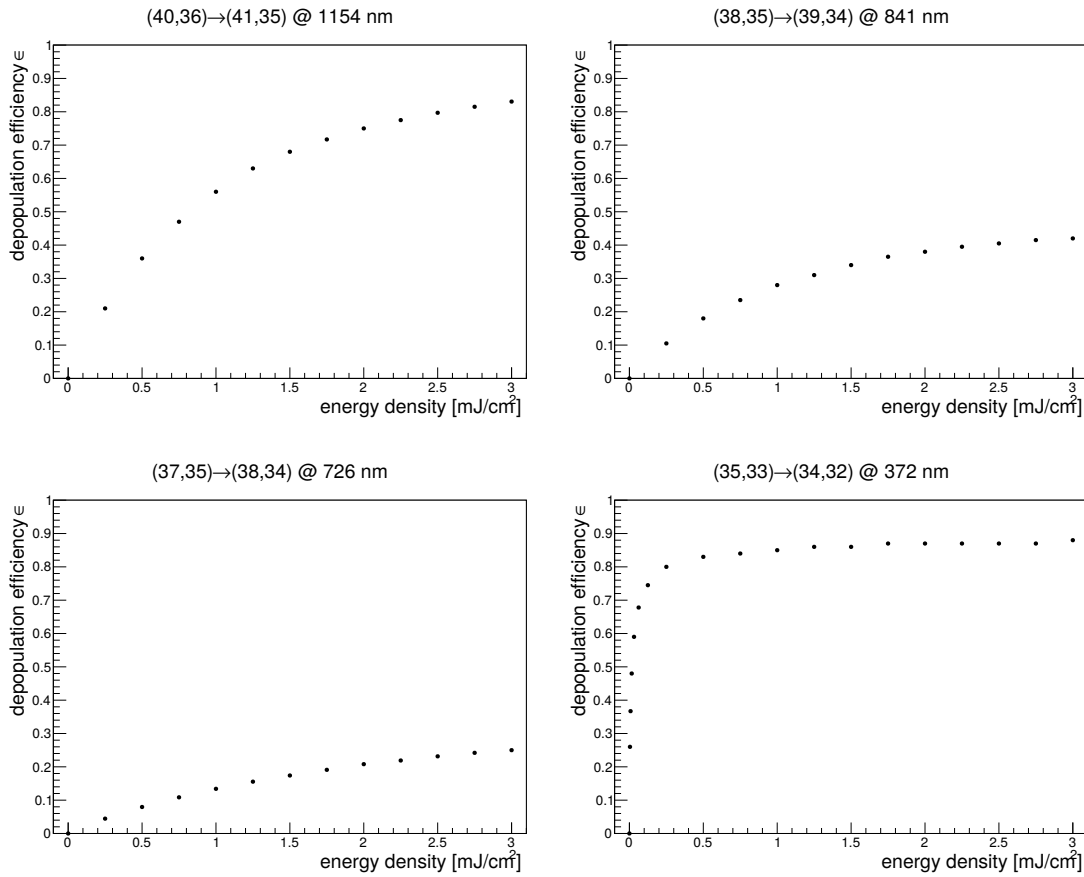


Figure 2.7.1: Simulated depopulation efficiencies as a function of the laser pulse energy.

Table 2.2: Transition parameters: Transition wavelength λ , the averaged dipole moment $\langle\mu\rangle$, the parent and daughter states lifetimes τ_p and τ_d , the laser pulse length (FWHM) δ_t .

parent	daughter	λ	$\langle\mu\rangle$	τ_p	τ_d	δ_t
(40, 36)	(41, 35)	1154 nm	0.034 D	2.2 μs [43]	0.2 ns [43]	30 ns
(38, 35)	(39, 34)	841 nm	0.030 D	2.2 μs [18]	1 ns [26]	60 ns
(37, 35)	(38, 34)	726 nm	0.023 D	3.0 μs [18]	10 ns [26]	60 ns
(35, 33)	(34, 32)	372 nm	0.361 D	3.0 μs [18]	6 ns [26]	30 ns

Chapter 3

Experimental setup

The experiments presented in this work were carried out in a similar setup as reported in Ref. [16]. A schematic illustration is provided in Fig. 3.0.1: A pulsed antiproton beam was allowed to come to rest in low density helium target gas and subsequently irradiated with a pulsed laser beam at a characteristic $\bar{p}\text{He}^+$ transition frequency. A Cherenkov detector positioned in proximity measured emerging annihilation products.

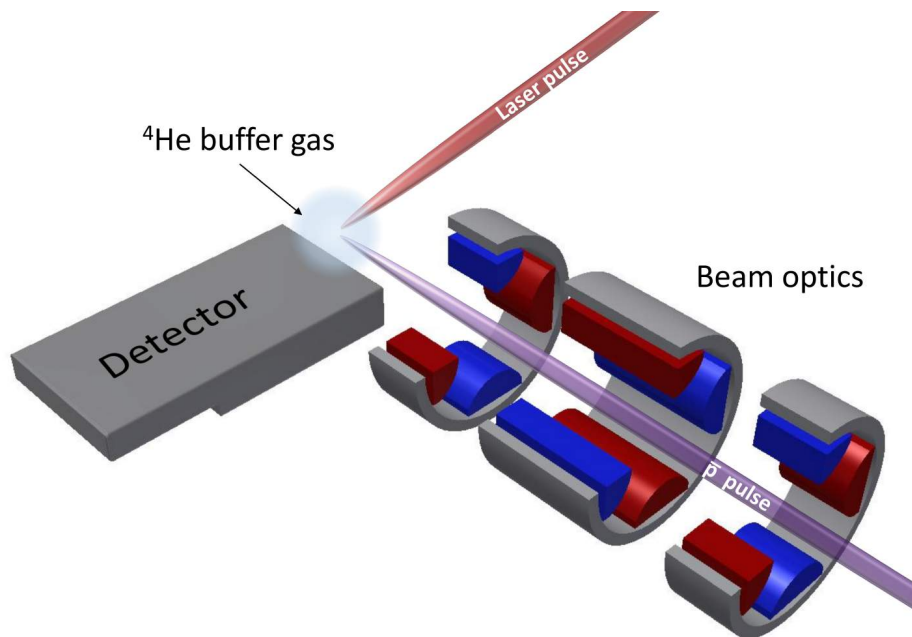


Figure 3.0.1: Overview to the experimental setup. Antiproton bunches were allowed to come to rest in a low density helium gas. A pulsed laser was irradiated on the target at a character transition frequency of the $\bar{p}\text{He}^+$ atom. Nuclear fragment emerged and were detected with a Cherenkov counter.

3.1 Antiprotons

3.1.1 Production target

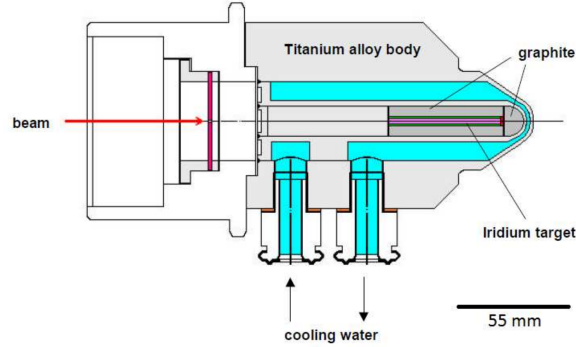
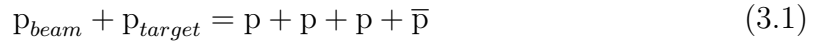


Figure 3.1.1: CERN AD antiproton production target. Being 3 mm in diameter and 55 mm long the Ir target is encapsulated by a graphite matrix and embedded into a water cooled titanium housing. Fig. from [58]

Antiprotons can be produced via irradiation of fixed solid targets with high energy protons, here the predominant production reaction is



where the antiproton yield increases with the intensity and energy of the primary proton beam.

For the design of a dedicated production target the following aspects have to be considered:

- The proton interaction length L_{int} must be as large as possible, such that many protons contribute to the production. At the same time the antiproton absorption length L_{abs} must be small enough for most antiprotons to leave the target before annihilation. The optimum condition is typically met at $L_{target} \approx L_{int} \approx L_{abs}$. On the other hand beam optics for the incident p and emerging \bar{p} -beam can be better adapted for small L_{target} , which is why dense materials are preferred.
- The incident proton beam has to be as small as possible to fix the antiproton emittance $\epsilon = \pi x'x$. The chosen material must therefore be stable against thermal shock waves triggered by the high intensity beam.

In Fig. 3.1.1 the design of the current CERN antiproton production target is illustrated. It comprised a thin iridium rod of diameter $d = 3$ mm and length $L_{target} = 55$ mm

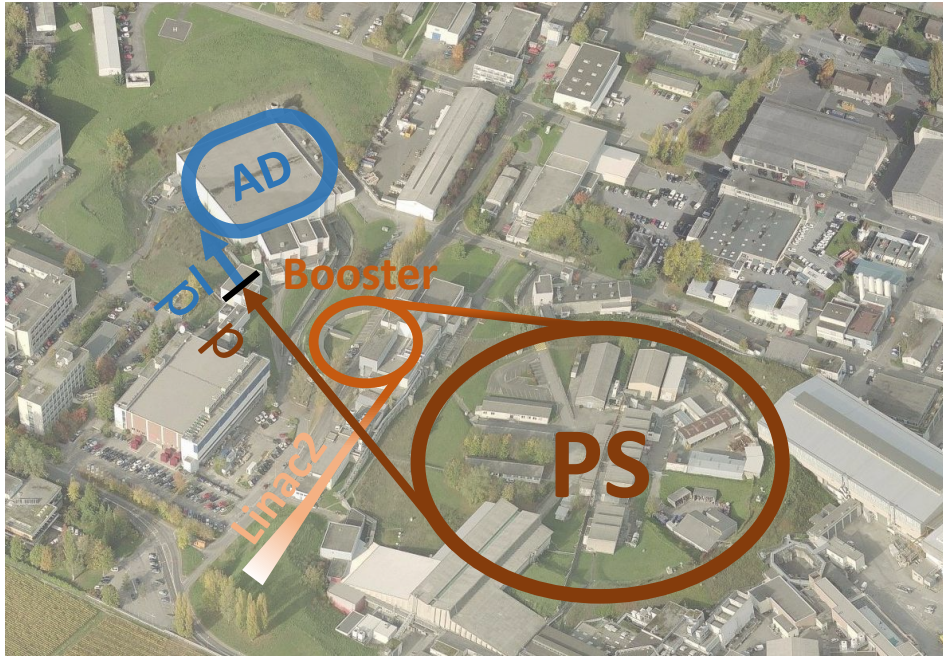


Figure 3.1.2: The AD is part of the CERN accelerator complex. Protons are accelerated to 26 GeV in the linear and circular accelerators 'Linac2', 'Booster' and 'Proton Synchrotron' (PS) before being irradiated onto the antiproton production target. The emerging antiprotons are decelerated and cooled in the AD. Areal view from <http://maps.cern.ch>

encapsulated in a graphite matrix which was embedded in a water cooled titanium body. Iridium is the second densest material on earth with $\rho = 22.65 \text{ g/cm}^3$, thermal expansion $\alpha_v = 6.4 \times 10^{-6} \text{ K}^{-1}$ and conductivity $k = 237 \text{ W/(m}\times\text{K)}$. In this design destructive thermal shock waves limit allowed temperature excursions to $\sim 1800 \text{ K}$ corresponding to a 1 mm proton beam $\sim 6 \times 10^{14}$ protons \times GeV [59].

3.1.2 The CERN AD

The CERN Antiproton Decelerator (AD) is an oval shaped 188 m circumference storage synchrotron incorporated into the CERN accelerator complex as shown in Fig. 3.1.2. It decelerates and cools antiproton bunches from $\sim 3.6 \text{ GeV}$ to 5.3 MeV kinetic energy. Deceleration is necessary since antiprotons are efficiently produced only at energy scales well above what that of trap and spectroscopy experiments carried out in the AD. In accordance with Liouville's theorem, however a mere deceleration would result in an adiabatic expansion in the ensemble's phase-space density

$$D = \frac{N}{\sqrt{E_v E_h}} L \frac{\Delta p}{p} \quad (3.2)$$

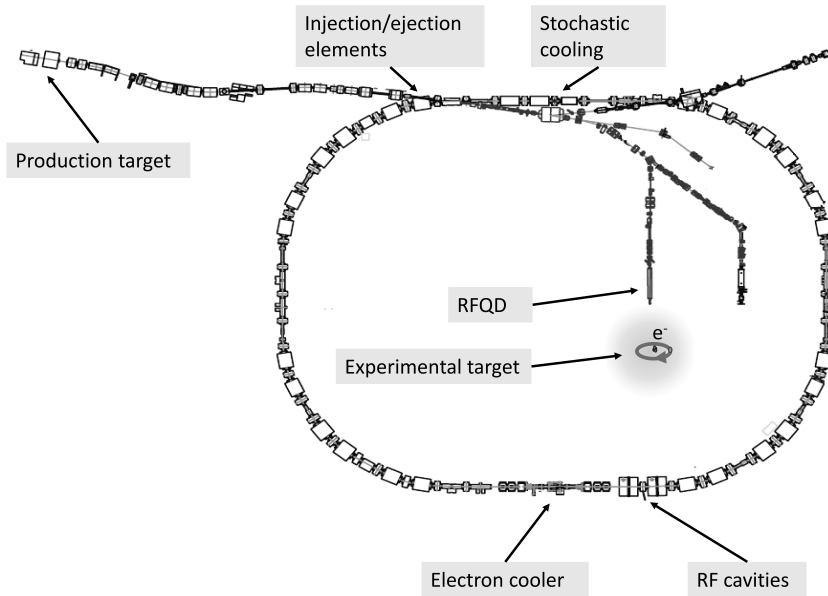


Figure 3.1.3: The AD is a 188 m circumference storage synchrotron that decelerates and cools antiprotons from kinetic energies ~ 3.6 GeV to 5.3 MeV. It comprises deceleration and cooling instruments besides dipole and quadrupole magnets for beam bending and focusing. Fig. from <http://cern.ch>.

where E_v and E_h denote the vertical and horizontal emittance, L the longitudinal length, and $\Delta p/p$ the momentum spread. For these reasons the AD comprises cooling instruments besides radio-frequency deceleration cavities, see Fig. 3.1.3. During the experiments reported here the AD operated in a ~ 100 s cycle that could be divided into the following steps: (i) production: proton bunches of energy 26 GeV and intensity 1.5×10^{13} protons per bunch were extracted from the CERN Proton Synchrotron (PS) and irradiated on the production target. Emerging antiprotons were focused into a parallel beam using a pulsed current (400 kA) magnetic horn-type lens. The obtained beam of energy ~ 3.57 GeV, transverse emittance $\sim 200 \pi$ mm mrad, momentum spread $\Delta p/p \sim 6\%$ and longitudinal length $L = 30$ m ($\geq \Delta t = 25$ ns) was injected into the AD, at a yield $\bar{p}/p \approx 3.5 \times 10^{-6}$, i.e. 5×10^7 antiprotons per bunch. (ii) RF bunch rotation: In the first step the RF cavity stretched the bunch length to $L = 190$ m or $\Delta t = 150$ ns reducing its momentum spread $\Delta p/p$ to 1.5%. (iii) Stochastic cooling and first deceleration: pick up electrodes detected transverse position and momentum variations of antiproton subgroups with respect to the total ensemble. This information was transferred to a kicker electrode on the opposite side of the ring which steered the corresponding subgroups towards the mean value. This process was iterated until the antiproton bunch orbit converged i.e. the emittance was reduced

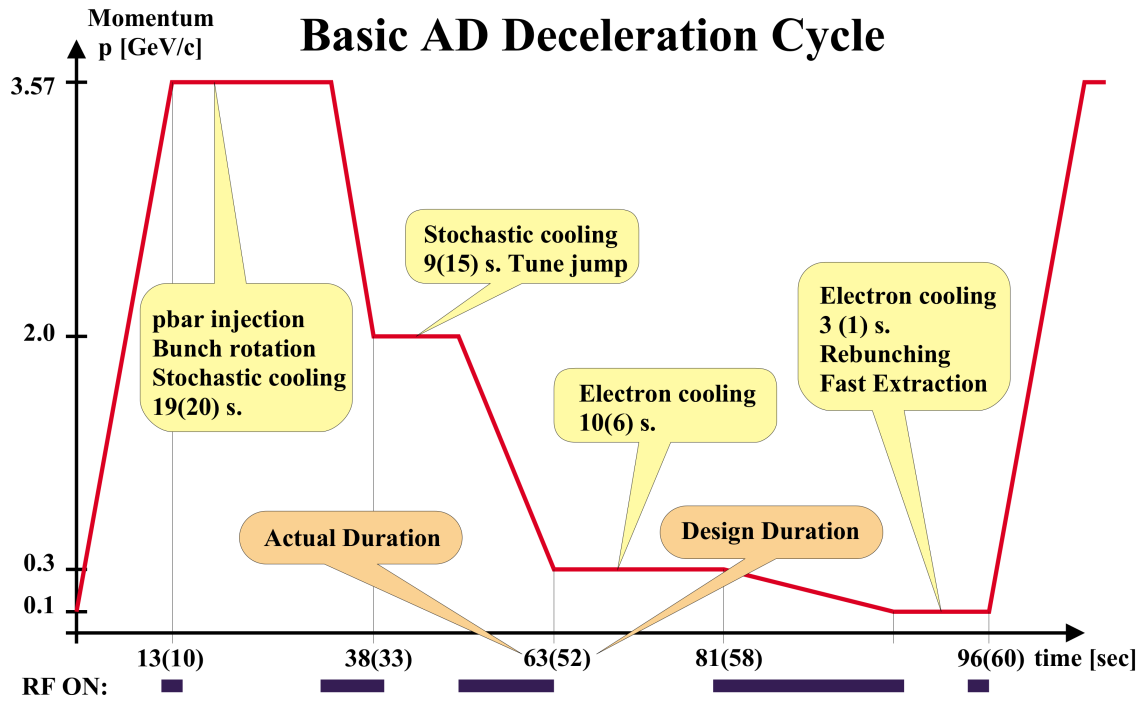


Figure 3.1.4: Illustration of AD cycle, with the antiproton momentum plotted against the elapsed time. Fig. from [61]

to $3 - 4\pi$ mm mrad and $\Delta p/p = 0.07\%$. Now the antiprotons were decelerated in the RF cavity to 2 GeV kinetic energy and stochastic cooling is repeated. (iv) Second deceleration and electron cooling: in the subsequent step the antiproton bunch was further decelerated to $p = 300$ MeV/c before being electron cooled i.e merged with a 20 mm diameter $I \sim 3$ A low temperature electron beam. For optimal cooling the velocity of the electrons was chosen such that they appeared stationary in the antiproton rest frame. Finally the antiprotons were decelerated to $p = 100$ MeV/c, electron cooled again and decelerated to $p = 5.3$ MeV/c. At the end of the 100 s cycle the beam was ejected towards the individual experiments with emittance 0.3π mm mrad, momentum spread $\Delta p/p = 0.01\%$ containing $\sim 3 \times 10^7$ antiprotons per bunch [59] [60]

3.1.3 The ASACUSA RFQD

Together with the CERN beam department the ASACUSA collaboration developed a radio frequency quadrupole decelerator (RFQD) which further reduced the kinetic energy of the AD beam to 10 – 120 keV [62]. To prevent antiprotons from hitting its inner walls during the deceleration process the RFQD also strongly focussed the beam. The RFQD consisted of four 3.4 m long rod electrodes in a quadrupole formation

with a ~ 1 cm aperture. The shape of the electrodes was wavelike with a series of peaks and troughs. Pairs of opposite electrodes were identical while peaks and troughs are shifted for neighbouring electrodes by half a period. The rods were excited by a radiofrequency field of frequency $f = 202.5$ MHz and maximum voltage $V \sim 170$ kV on the rod surfaces. Before the antiproton beam from the AD was allowed to enter the RFQD it was shaped by a radio-frequency buncher into a train of 300 ps long micro-bunches at 202.5 MHz. Beam tuning of the bunched beam into the RFQD was aided by scintillation detectors. These were two plates of BC-408 (Saint-Gobain) which were inserted into the antiproton beam line such that circular holes at their center were on axis with the RFQD aperture. Two CCD cameras were pointing to the scintillation plates and detected the released scintillation light whenever parts of the antiproton beam was off axis to the RFQD aperture. During their passage through the RFQD the antiprotons were decelerated along the longitudinal axis by a few megavolt per meter. The wavelength of the electrodes gradually decreased matching the antiproton velocity change. Furthermore the antiprotons were alternately focused and defocused in the two transversal planes by the electrode quadrupole structure resulting in a net focusing in both planes. A tunable DC bias superimposed upon the RFQD radio-frequency field allowed to adjust the kinetic energy of emerging antiprotons. Some 25% of the antiprotons that entered were successfully decelerated and exited the RFQD under emittance $\epsilon \sim 50 - 100\pi$ mm mrad and energy spread $\Delta E/E \approx 10\%$.

3.1.4 Low energy beam transport

In the experiments reported here the beam emerging from the RFQD was transported to the experimental target in a dedicated low energy beam line, schematically illustrated in Fig. 3.1.5. An achromatic momentum analyzer, consisting of two dipole magnets separated the decelerated from the non-decelerated beam. The beam line also comprised a magnetic quadrupole triplet, three solenoids and an electrostatic quadrupole triplet to prevent the high emittance beam from hitting inner beam line walls. For operation the solenoids required relatively large currents of order ≥ 200 A. In order to reduce the heat load, the current was provided in form of μ s long pulses matched to the antiproton time of flight. The electrostatic quadrupole triplet was composed of a series of three individual quadrupole lenses of length $L = 100$ mm, 200 mm and 100 mm. Each lens was made of four cylindrical stainless steel electrodes with radius of curvature $r = 57.5$ mm operated at a voltage $V \pm 3.5$ kV. Under appropriate settings the beam diameter in front of the target could be reduced $d \lesssim 15$ mm.

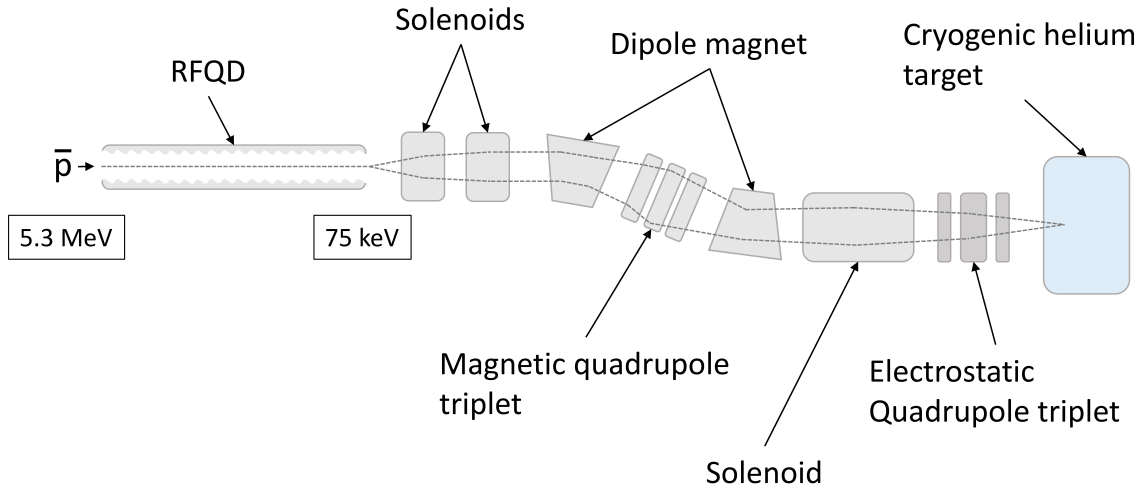


Figure 3.1.5: Overview of low energy beam line. Antiprotons emerging from the RFQD pass an achromatic momentum analyzer consisting of two magnetic dipoles. A series of lenses prevents the antiproton bunches from hitting inner walls.

Critical to beam tuning was the knowledge of the beam's position and divergence. For this reason three parallel plate secondary emission chambers were positioned behind the RFQD, just before the electrostatic quadrupole triplet and in front of the target. These beam profile monitors (BPM) consisted of two position sensitive photocathode grids arranged in the X-Y-plane. Each grid comprised 32 gold coated tungsten wires of thickness $5 - 10 \mu\text{m}$ separated from each other by $0.25 - 1 \text{ mm}$. The two photocathode grids (biased at -50 V) were sandwiched between 3 anode grids (at ground potential). All grids were stretched over a ceramic frame of size $100 \text{ mm} \times 90 \text{ mm} \times 2 \text{ mm}$ with a $50 \text{ mm} \times 50 \text{ mm}$ opening at its center to allow the beam pass through. The ceramic frame was fixed within a vacuum chamber which was mounted to the beam line. When antiprotons hit the photocathode wires, electrons were released and accelerated towards the anode grids. Charge sensitive preamplifiers measured the ejected charge. The signal was sent to an active-filter post amplifier and subsequently digitized using an CAMAC ADC [63,64].

3.2 Cryogenic target

The antiproton beam was allowed to come to rest in a low density helium buffer gas target. The target chamber was $15 \text{ cm} \times 15 \text{ cm} \times 15 \text{ cm}$ in size, made of oxygen free high conductivity (OFHC) copper and comprised 70 mm diameter windows on its 4 sides. The base side was only 2 mm thick allowing nuclear fragments to penetrate

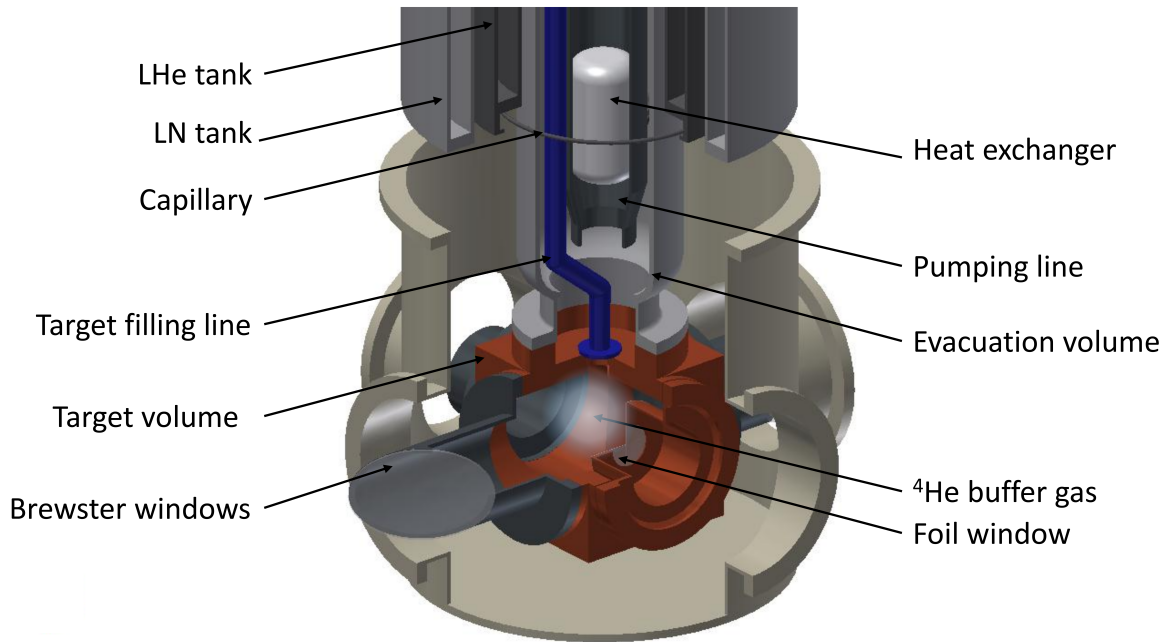


Figure 3.2.1: Schematic overview on the helium gas target cooled from the top by an open cycle Joule-Thompson cryocooler. All OHFC heat shields are omitted for better visibility.

through. Antiprotons entered through a $1.4 \mu\text{m}$ thick biaxially-oriented polyethylene terephthalate (BoPET) window which was additionally strengthened by an array of gold plated tungsten wires. The other 3 windows were made of fused silica for the access with laser beams. The two opposing fused silica windows were cut at Brewster's angle.

While the target was being cooled to 1.3 K, ultra high purity ^4He (99.999%) was introduced via a separated filling line. A thin layer of superfluid helium condensed on the inner walls from which cold gas evaporated. This buffer gas, used as target, was operated at $P = 1.1 \text{ mbar}$ pressure and $T = 1.5 \text{ K}$ temperature corresponding to an atomic density $\rho = 5 \times 10^{18} \text{ cm}^{-3}$ and collision rate $\nu_{\text{coll}} = 5 \times 10^6 \text{ s}^{-1}$. The gas pressure was continuously measured by capacitance manometers and stabilized within $< 1\%$ of its nominal value. Two carbon ceramic temperature sensors [65] were encapsulated by an OHFC copper housing and thermally connected to the top and bottom of the target housing using indium joints. A 5 m long low temperature graded 4 wire manganin-copper cable (12% - 84%) [66] connected the sensors to a temperature monitoring unit [67]. To avoid a thermal link between the target volume and room temperature the 4 wire cable was thermalized to the cold surface inside the cryostat at several points. The entire target structure was covered by two layers of blackened

OHFC copper heat shields thermalized at 4.2 K and 77 K respectively.

On the top side the target was in thermal contact with an open-cycle Joule-Thomson type cryocooler. Within the cryocooler liquid helium was stored at 1.1 bar in a thermally isolated reservoir. A separated expansion volume was evacuated through a 150 mm diameter pumping line by a 2000 m³/h roots blower and a 800 m³/h rotary vane pump. A thin capillary tube connected the two volumes. Liquid helium from the reservoir transported through the capillary was first precooled to 2.2 K in a coil type heat exchanger, wound within the pumping line, before it was allowed to expand through a needle valve, controlled by a stepper motor, into the expansion volume. During this expansion the helium coolant reduce its temperature to 1.3 K while five layers of OFHC heat baffles thermalized at $\sim 4 - 70$ K protected it against heat radiation from the warm pumping line. The cryocooler was arranged in a cylindrical configuration such that the expansion volume comprising the coolant was surrounded by the liquid helium reservoir and second reservoir containing liquid nitrogen thus providing additional protection against heat radiation. The entire cryosystem was separated from room temperature environment through an isolation vacuum at $\sim 10^{-5}$ mbar directly connected to the AD accelerator system, see below Sec. 3.2.1. A 1 m thick concrete wall protected the cryogenic setup from the acoustic noise of the pumps. Continuous pumping in the target's proximity was provided by a 800 l/s turbomolecular pump additionally to natural cryo-pumping. When continuously operated the cryostat's liquid helium and nitrogen consumption was ~ 800 and 400 l per week respectively.

In this design the temperature and pressure of the buffer gas were highly sensitive to the presence of coolant in the evacuation volume, while a sudden expansion of the buffer gas could have exploded the thin BoPET window. For safety reasons the coolant level was therefore continuously measured in two redundant ways: (i) two temperature sensors were added: one directly submerged in the coolant and another mounted further upwards on the pumping line. (ii) a liquid helium level gauge was positioned in the evacuation volume. It comprised a fine superconductive filament contained within a 0.25 inch diameter tube through which a current was sent keeping it in resistive state when submerged in gaseous and superconducting states when in liquid helium. A helium monitoring unit measured the voltage along the level gauge and thus provided the level in 2 minute intervals [68]. A dedicated software program monitored the temperatures, the target pressure and the liquid helium level at all times. The software also enabled remote access of the stepper motor controlling the needle valve and thus allowed for necessary adjustments while the experiment was

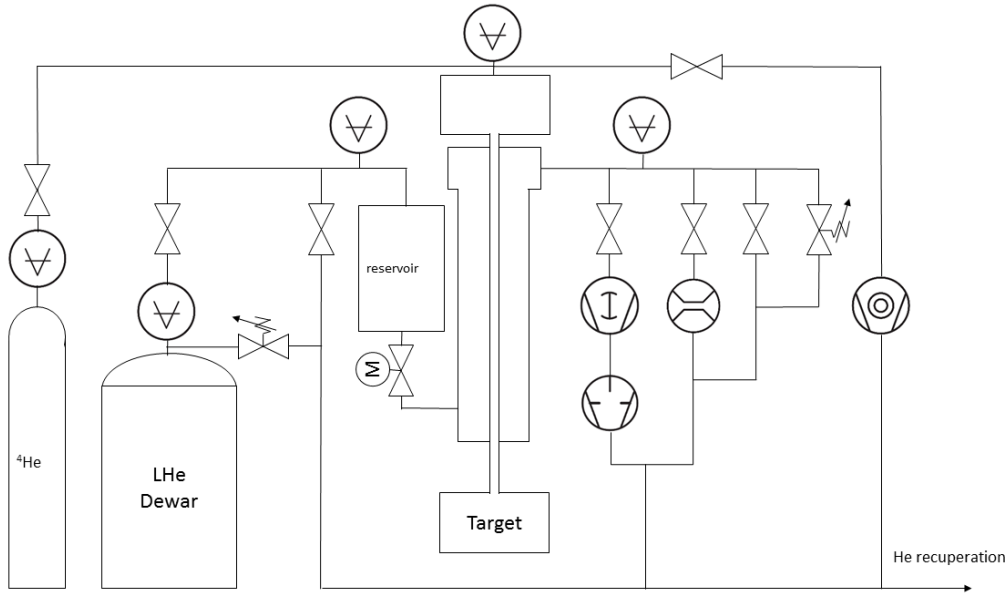


Figure 3.2.2: Schematic illustration of helium gas system employing two separate circuits. (i) Coolant is loaded to a reservoir from where it is allowed to slowly penetrate into an evacuation volume. There evaporative cooling results in a further temperature drop to 1.5 K. (ii) High purity ^4He gas is filled through an ultra clean line into the cooled target. Helium from both lines is recuperated into the CERN helium system.

running and access to the experimental area was limited due to high radiation levels.

3.2.1 Cold leak 2015

In previous years the isolation vacuum in the system measured $\leq 10^{-7}$ mbar. During the experiments reported in this work however our target housing suffered a cold leak at the rate $\sim 10^{-4}$ mbar $\times 1 \times \text{s}^{-1}$ discovered only days before the beam time. The leak was small enough such that the pressure drop in the target could be overcome by a continuous inflow of high purity helium. However three more turbomolecular pumps with a combined pumping power ~ 1700 l/s were added along the antiproton beam line. With these the vacuum level in the vacuum system could be improved by two orders of magnitude on the accelerator side and a factor two near the target side.

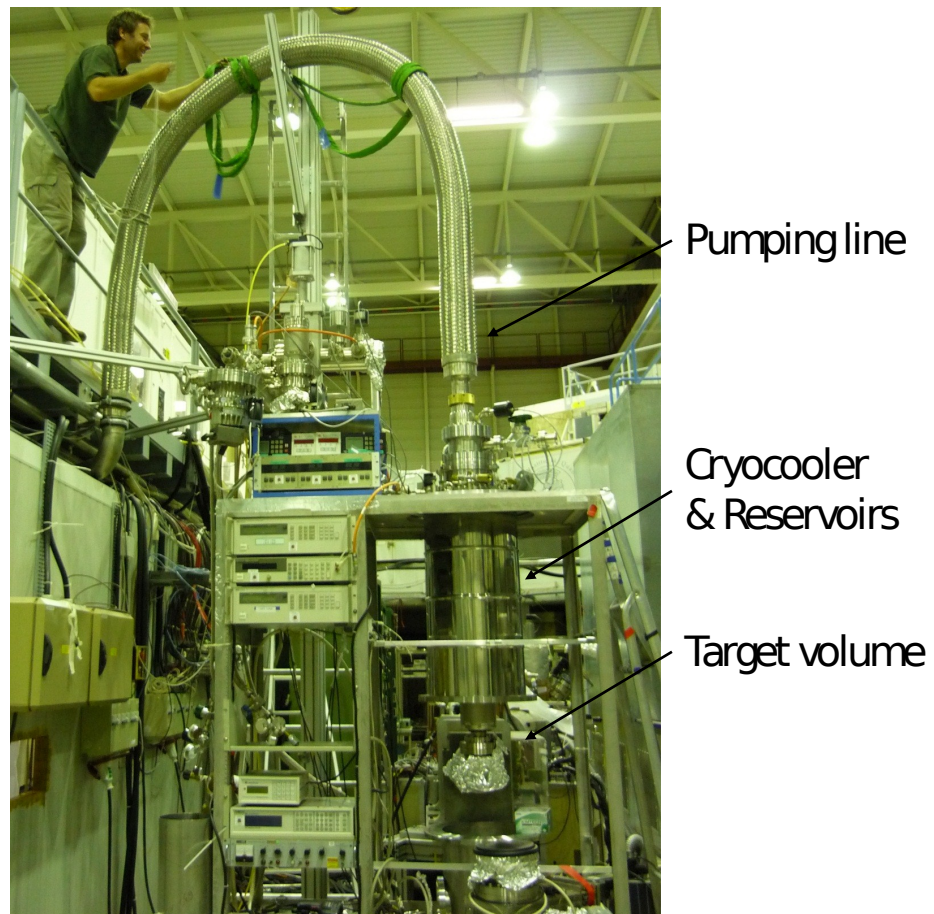


Figure 3.2.3: Target setup: The cryocooler, LHe and LN reservoirs were arranged in a concentric setup and supported from their top on a stainless steel support structure. A 150 mm pumping line connected the cryocooler evacuation volume to a 2000 m³/h roots blower and a 800 m³/h rotary vane pump (not shown in the picture). The target housing was connected to the cryocoolers bottom. A 1 m thick concrete wall protected the cryogenic setup from the acoustic noise of the pumps.

3.3 Detection system

Charged particles emerging from antiproton annihilations in helium were detected using a Cherenkov counter [51]. The increased yield towards the UV motivated the usage of Cherenkov media that contained no UV absorbing additives [69]. An acrylic (Bicron BC-800 decolorized methyl methacrylic monomer) plate of size $\sim 1000 \text{ mm} \times 300 \text{ mm} \times 20 \text{ mm}$ and refractive index $n = 1.49$ was used. Charged particles with velocities $v \gtrsim 0.7 \times c$ corresponding to a kinetic pion energy $E_\pi \gtrsim 130 \text{ MeV}$ produced Cherenkov light in this material. Optical transmission through the plate was $\geq 90\%$ at all visible wavelengths above 350 nm. The plates were covered in a 4 μm thick inner layer of reflecting aluminum and a 100 μm thick outer layer of blackened plastic. For

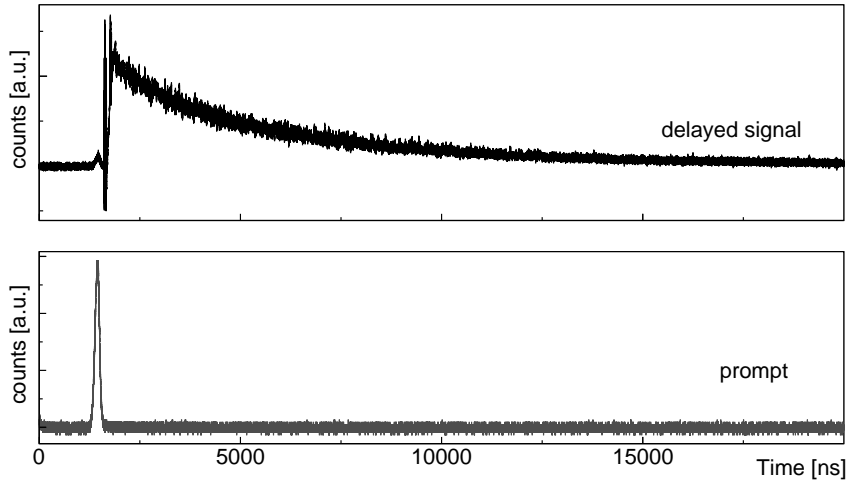


Figure 3.3.1: Typical event: (i) Delayed component measured with a gated Cherenkov counter (ii) prompt measured with the ungated cherenkov detector

readout a triangular-shaped waveguide made of the same material coupled the plate optically to a 34 mm diameter custom made fine mesh photomultiplier tube (PMT, Hamamatsu Photonics R5505 GXASSY2). The photomultiplier consisted of a series of 19 fine mesh dynodes each separated by less than 1 mm from its neighbours. The time structure of the Cherenkov light consisted of a strong initial flash and a long tail attributed to prompt and delayed antiproton annihilations. To avoid saturation by the initial flash, the PMT was gated off for $\sim 100 - 200$ ns. For this the potentials on four of the dynodes were reversed during the gate. The Cherenkov counter was located ~ 10 cm below the helium target covering a solid angle of $\sim 1.2\pi$. A second smaller ungated Cherenkov counter of size $10 \text{ mm} \times 30 \text{ mm} \times 20 \text{ mm}$ was positioned nearby for the detection of the initial prompt. Both PMT signals were recorded using a digital oscilloscope with 2 GHz sampling rate and 8 bit resolution. The real timing resolution however was determined by the time response of the photomultiplier which was ~ 5 ns. For each event $20 \mu\text{s}$ long spectra were recorded. Typical spectra are shown in Fig. 3.3.1 where channel 1 corresponds to the big Cherenkov detector measuring the delayed component and channel 2 the small detector measuring the prompt.

3.4 Laser system

Simulations in Sec. 2 have shown that to efficiently induce $\bar{p}\text{He}^+$ transitions with dipole moments ranging between $0.02 - 0.4$ Debye and given the microsecond long parent state lifetimes, laser beams with power densities of $\gtrsim 20 \text{ kW/cm}^{-2}$ must be used. Laser spectroscopy experiments however require narrow linewidth. To

achieve both requirements, injection seeded pulsed laser beams with 30 – 100 ns long pulse-lengths were used in a setup very similar to the one reported in Ref. [70]. A schematic illustration of the used system is provided in Fig. 3.4.1. A cw Nd:YVO4 DPSS laser of output power $\theta = 10$ W pumped a Ti:Sapphire ring laser (Coherent MBR-110-PS or 899–21) such that $\gtrsim 1$ W cw power at wavelengths $\lambda = 726 - 841$ nm could be obtained. The cw beam was stabilized to a Fabry-Perot cavity of free spectral range 390 MHz and finesse 2000, using the Pound-Drever-Hall technique. For pulse amplification it was transported over a distance $d \sim 3$ m in a single mode optical fiber and then seeded into a second ring laser with cavity length $L_{circ} = \sim 300$ mm. This cavity consisted of a concave mirror with a radius of curvature $R_c = 4$ m mounted on a piezo crystal (PZT), a dispersive prism as a rough wavelength selecting element (PRISM), a 20 mm long Ti:Sapphire crystal cut at Brewster's angle with its c-axis parallel to the laser polarization (C1) and a flat output coupler with reflectivity 80%–90% (OC). The cavity was designed for large transverse mode diameters $d_t \sim 1.1$ mm to allow for reduced power densities in the Ti:Sapphire crystal which lowered the single pass gain and thus resulted in longer laser pulses. The laser cavity length was locked to the seed beam in the following way: (i) The piezo mounted mirror in the cavity was dithered at the frequency $f_d \sim 26$ kHz (ii) amplitude modulated light reflected from the prism was measured with a photodiode (iii) using the diode signal a lock-in amplifier generated a correction signal referenced to f_d (iv) this correction signal was fed back to the piezo. The pulsed ring laser generated 40 – 100 ns long laser pulses of energy $E \sim 6 - 8$ mJ. These were further amplified to 8 – 35 mJ in three passes through another Ti:Sapphire crystal (C2). The final linewidth of the pulse amplified laser beam was of order $\lesssim 100$ MHz. For the study $\bar{p}\text{He}^+$ transition $(n, \ell) = (35, 33) \rightarrow (34, 32)$ a UV beam at $\lambda = 372$ nm was generated via frequency doubling of the appropriate IR beam in a beta barium borate (BBO) crystal. Analogously the $(n, \ell) = (40, 36) \rightarrow (41, 35)$ was studied with a laser beam at $\lambda = 1154$ nm generated via Raman shifting of an IR beam at $\lambda = 780$ nm in a multi-pass hydrogen cell, see Sec. 3.5. The pulsed ring laser and the three-pass amplifier were pumped by the second harmonic of a Q-switched Nd:YAG laser which provided 3 ns long pulses of energy $E \sim 200$ mJ at 532 nm wavelength. In order to prevent the high peak power from damaging the Ti:Sapphire crystals, the 3 ns long pulses were stretched to ~ 20 ns in a series of beam splitters. The stretched pulse was then separated into three parts such that one part of energy $E \sim 20 - 40$ mJ was used to pump the ring laser crystal and the remaining two were used for the 3 pass crystal.

During all experiments the wavelength of the cw seed laser was recorded us-

ing a Fizeau type wavemeter (HighFinesse/Angstrom WSU-10). The seed beam entered the device via an optical fiber where it was split into several beams. Each beam was allowed to pass a Fizeau interferometer of specified length and the resulting interference patterns were recorded with a CCD. A connected PC calculated the laser wavelength from the aggregate of all recorded patterns. All optical instruments were located in a dust-free low humidity laser hut from where the laser beam was transported to the experimental area using high reflectivity mirrors. During this transport typically 30% - 50% of the laser power was lost. Right before the experimental target the laser beam was expanded to a diameter $d \sim 2$ cm for maximal overlap with the antiproton stopping distribution in the buffer gas target. In Table 3.1 we summarized the realized laser specifications. In the near infra-red 6 – 10 mJ power could be achieved at $\lesssim 100$ MHz linewidth. The nonlinear processes for the generation of UV and IR light came at the cost of some power loss and linewidth broadening. In particular linewidth at 1154 nm was strongly broadened due to the Raman width of the H_2 gas, which was of order ~ 500 MHz given the temperature and pressure conditions in the respective cell, see Sec. 3.5. It should however be noted that the 372 nm and 1154 nm transitions are known to be relatively broad by themselves \sim GHz, see Sec 2, which is why a very narrow laser linewidth was not desirable.

The AD control electronics provided a trigger signal $380 \mu s$ before the antiprotons arrived at the target. The Nd:YAG Q-switching could be adjusted to this AD trigger and thus allowed to control the laser timing with respect to the antiproton arrival at the target. Population evolution measurements were executed by time scanning of the Nd:YAG laser Q-switching against the AD-trigger. In the experimental area a p-i-n photodiode recorded the arrival time of the laser beam. The observed timing jitter of the laser measured less than 5 ns.

Table 3.1: Experimentally realized laser conditions for the four studied transitions and expected depopulation efficiency.

λ	δ_t	energy/pulse	linewidth	ϵ
1154 nm	~ 28 ns	1.75 ± 0.5 mJ	~ 600 MHz	35%
841 nm	~ 54 ns	10 ± 2 mJ	$\lesssim 100$ MHz	40%
726 nm	~ 54 ns	6 ± 1 mJ	$\lesssim 100$ MHz	25%
372 nm	~ 41 ns	2 ± 0.5 mJ	$\lesssim 200$ MHz	83%

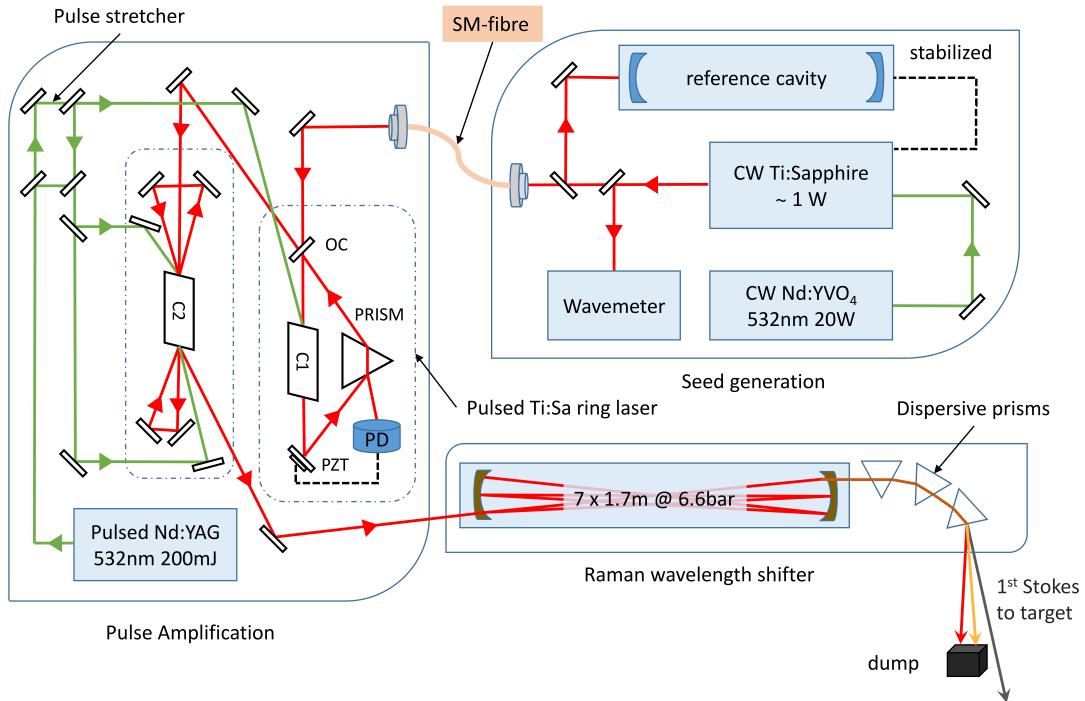


Figure 3.4.1: The narrow linedwidth and high power requirement were satisfied in a setup where CW beam is stabilized on a Fabry-Perot reference cavity and then pulse amplified in Ti:Sapphire ring laser and 3-pass amplifier.

3.5 Hydrogen gas Raman shifter

The wavelength tuning range of Ti:Sapphire is $\lambda \sim 680\text{--}1100\text{ nm}$ whereas the maximum gain and lasing efficiency is obtained at $\sim 790\text{ nm}$. In order to access the transition $(40, 36) \rightarrow (41, 35)$ at 1154 nm , a wavelength shifting cell was developed together with the MPQ workshop that employed stimulated Raman scattering (SRS) [71]. The cell was filled with high pressure H_2 gas and irradiated with an intense pump beam at wavelength $\lambda_p = 780\text{ nm}$. The intense vibrational $Q(1)$ transition of the H_2 molecule at $\nu_R/c = 4155\text{ cm}^{-1}$ provided the associated Stokes field at wavelength $\lambda_s = 1154\text{ nm}$.

3.5.1 Prior consideration

For details to the Raman process see Appendix B. We designed the cell for a tight focussing laser setup in order to maximize the peak field at the cell center and thus the conversion efficiency [72]. A full simulation of the Raman process is difficult and often not very accurate. It is therefore customary to characterize wavelength shifting cells employing SRS through the estimation of the threshold power P_{thr} , which is defined as the pump power P_p required for to produce 1 kW in the first Stokes. Due to

the avalanche nature of the SRS process higher conversion rates are up to 50% are readily possible beyond this point when $P_p \approx 2 - 3 \times P_{thr}$ [73]. It is further important to note that stimulated Raman scattering requires the presence of an initial seed field. In many wavelength shifting gas cells this initial field is provided by spontaneously Raman scattered photons of the pump beam. It has been shown that photons generated in this way are random in phase [74] and thus ultimately only one single photon serves as seed for the SRS process. Nevertheless it must be guaranteed that at least one seed photon in the correct mode does exist which can then be amplified via SRS.

In the prior considerations, presented here, we estimated the constraints on critical design specifications such as cell length L , number of transits n and hydrogen gas density ρ such that

1. the number of potential seed photons generated via spontaneous Raman scattering N_{spont} was guaranteed to be > 1
2. the threshold power P_{thr} was $\lesssim 10$ kW thus allowing for the generation of Raman shifted light in the first Stokes of $\gtrsim 40$ kW with the given laser system.

Spontaneous Raman scattering

Spontaneous Raman scattering is a linear effect. Analogous to the Beer-Lambert law the number of spontaneously Raman scattered photons N_{spont} emitted into the solid angle $d\Omega$ is can be deduced from the number of photons in the pump beam N_{pump} , the number density of hydrogen molecules ρ_{H_2} and the differential cross section $\frac{\partial\sigma_R(\Omega)}{\partial\Omega}$, see Appendix B.

$$N_{spont} = \int N_{pump}\rho_{H_2}\frac{\partial\sigma_R(\Omega)}{\partial\Omega}d\Omega(z) \quad (3.3)$$

For our purpose we will restrict the integration over $d\Omega$ such that only photons are considered that pass through the entire Rayleigh length where, as will be shown later, SRS is most efficient. In a tight focussing setup $d\Omega$ is typically small allowing for the approximation $\frac{\partial\sigma_R(\Omega)}{\partial\Omega} = \text{const}$. Experimental values for $\frac{\partial\sigma_R}{\partial\Omega}$ obtained in forward scattering experiments were retrieved from Ref. [74] thus providing

$$N_{spont}(\lambda = 1154 \text{ nm}) \approx 3.5P_p \times \rho_{H_2} \quad (3.4)$$

where P_p and ρ_{H_2} are expressed in units of "mJ" and "amg" respectively. N_{spont} is independent of the cell length since only photons generated close to the beam waist are likely to contribute. We found that assuming $\rho_{H_2} = 6.6$ amg a pump energy per pulse

of $\gtrsim 1$ mJ is needed to guarantee that at least one potential seed photon is generated per pulse.

Stimulated Raman scattering

Stimulated Raman scattering is a non-linear effect. Following the approach of Boyd et al the steady state stokes field E_s can be deduced given the pump field E_p in an entirely classical ansatz [75]

$$\left(\frac{1}{k_s} \nabla_T^2 + i \frac{\partial}{\partial z}\right) E_p = \frac{i\epsilon_0}{2} cn^2 G |E_p|^2 E_s \quad (3.5)$$

with the material dependant Raman gain coefficient

$$G = \frac{3i\omega_s}{2\mu_s\mu_p\epsilon_0 c} \chi_R \quad (3.6)$$

The Raman gain coefficient is linear to the Stokes field frequency and depends on the so called Raman susceptibility χ_R . For details to Raman gain see Appendix B and Ref. [76]. It has been theoretically [77] and experimentally [72] shown that in a confocal setup with tight focus and under neglect of the pump depletion the Raman amplification into the first stokes can be approximated as

$$\frac{P_s}{P_{s0}} = e^{\alpha_1} = e^{\frac{1}{4\lambda_p} (2GP_p - 2\sqrt{4GP_p}) \cdot \arctan(L/b)} \quad (3.7)$$

where we have introduced the Rayleigh length b defined as

$$b = \frac{2\pi\omega_0^2}{\lambda_p} \quad (3.8)$$

It is seen that the conversion efficiency quickly saturates with increasing cell length L as $\arctan(L/b)$ converges towards $\pi/2$. This is due to the non-linearity of the SRS process which is most efficient in the high field region identified with the Rayleigh length. In steady state mode the Raman gain coefficient G can in principle be linearly scaled with the molecular density of the H_2 gas [78]. Transient effects however have been shown to strongly weaken this gain when pulsed lasers with $\delta t \sim$ ns are used [79] [80]. Ultimately the allowed H_2 density is limited by optical gas break down. The critical value for H_2 as a function of the intensity has been measured in Ref. [81]:

$$(\rho \times I)_{cr} \approx 4 \times 10^{12} \text{ amg} \times \text{Watt/cm}^2 \quad (3.9)$$

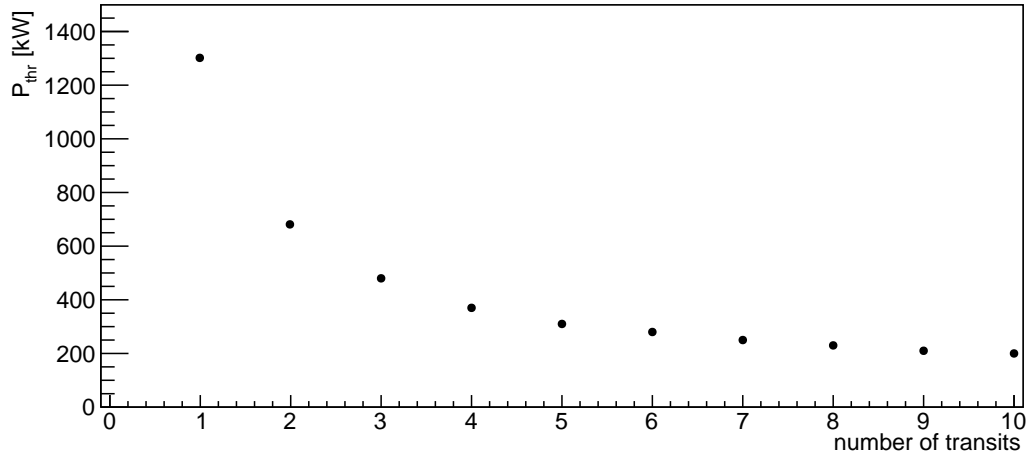


Figure 3.5.1: Mirror reflectivity $r = 90\%$, cell length $L = 1.71$ m, H_2 density $\rho = 7$ amg.

It is therefore customary to shift to a multi-pass design. Here P_{thr} is reduced via incrementation of the transit number n through the Raman medium. Following Ref. [82] the corresponding value α_1 in Eq. 3.7 must be replaced by α_n considering multiple transits. It can be expressed for given mirror reflectivity r

$$\alpha_n = \frac{1 - r^n}{1 - r} \alpha_1 + (n - 1) \ln(r) \quad (3.10)$$

In Fig 3.5.1 the resulting P_{thr} is shown as a function of the transit number, at given parameters: Mirror reflectivity $r = 90\%$, cell length $L = 1.7$ m, H_2 density $\rho = 7$ amg. We chose to implement 7 transits in our setup which reduces the expected P_{thr} from ~ 1.3 MW to ~ 250 kW compatible with the available pump laser. Thus, a symmetric Herrot type design similar to the one in Ref. [72] was used. Here the resonator parameters $g = 1 - L/R_c$ given by the mirror radius of curvature R_c define the angle between successive spots θ [83]

$$\theta = \cos^{-1}(2g^2 - 1) \quad (3.11)$$

Conversely it follows that one unique value for g is obtained for a cell with transit number n and integer value of azimuthal revolutions around the beam axis μ [84].

$$g = \frac{-1}{\sqrt{2}} \cdot \sqrt{\cos\left(\frac{4\pi\mu}{n+1}\right) + 1} \quad (3.12)$$

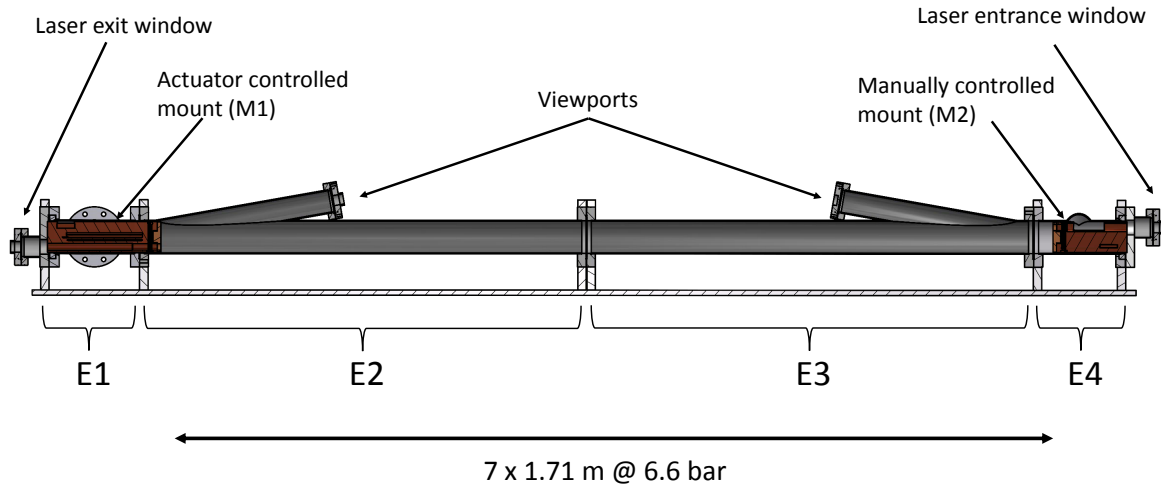


Figure 3.5.2: Schematical illustration of the 7-pass Raman cell with length $L = 1.71$ m. The actuator controlled mirror mount (E1) and view-ports (E2 and E3) comprising high pressure sapphire windows allowed for beam alignment after evacuation and filling of the cell.

The choice of g further defines the beam spot size on the mirrors w_m as well as at the beam waist w_0 [83]

$$w_m = \left(\frac{L \cdot \lambda}{\pi} \right)^{1/2} \left[\frac{1}{(1 - g^2)} \right]^{1/4} \quad (3.13)$$

$$w_0 = \left(\frac{L \cdot \lambda}{\pi} \right)^{1/2} \left[\frac{g(1 - g^2)^{1/2}}{2(1 - g)} \right]^{1/2} \quad (3.14)$$

The technical design of the cell was constrained by the obtained values for g , w_m and w_0 , which were determined by the choice of the transit number n .

3.5.2 Design

A schematical illustration of the cell is shown in Fig. 3.5.2. By default it comprised 7 transits of length $L = 1.71$ m but could be extended to 11 transits and $L = 1.87$ m. It consisted of four cylindrical stainless steel chambers that were connected in series. The two central elements (E2 & E3) were pipes of length $L = 847$ mm and diameter $d = 64$ mm to which a shorter ($L = 334$ mm, $d = 44$ mm) viewport-pipes were welded under an angle 10 degrees. The viewports had high pressure sapphire windows connected to their ends and were pointing to the mirrors thus aiding during

alignment once the cell had been closed. The two outer parts (E1 & E4) were 160 mm long standard cross and tee element respectively. Spring loaded mirror mounts (M1 & M2) were positioned within these outer elements. The material of choice for them was cupronickel in the mixture Cu-Ni-Fe = 89-10-1, with an elastic modulus of 135 GPa and high resistance against hydrogen fatigue [85]. One of the mirror mounts, shown in Fig. 3.5.3, was actuator controlled enabling mirror alignment after the cell had been closed. The actuators comprised DC motors operated at $V = 6$ VDC, $I = 0.25 - 6$ and a gearbox of ratio 134:1 yielding a maximum continuous torque of 0.3 Nm. The actuator and the corresponding wirings were vacuum rated to 10^{-6} mbar. The second mirror mount was controlled by micrometer screws instead of actuators. It was positioned in the tee type element through which it could be accessed. The mounts held concave gold plated copper mirrors, with radius of curvature $R_c = 1$ m and an 12 mm diameter off axis through hole for laser entry/exit. High pressure sapphire windows of diameter 25 mm were mounted collinear to the mirror holes on the vacuum chambers. The entire cell was pumped for over a week to a pressure 3.5×10^{-6} mbar before it was filled with high purity hydrogen (99.999% ^2H) to 6.6 bar. It was operated at room temperature resulting in a Raman width of ~ 400 MHz [78]. Assuming that the Raman contribution is additive one obtains approximately 500 MHz as the effective linewidth of the Raman shifted laser beam.

A pulsed beam of energy $E = 14$ mJ per pulse, pulse length $\tau = 50$ ns FWHM and wavelength 780 nm was mode matched into the cell using planoconcave lenses with large focal lengths $f = 5, 3, 2$ m. The first Stokes line at $\lambda = 1154$ nm and $E \sim 3$ mJ per pulse was obtained and separated from the fundamental and anti-Stokes using dispersive fused silica and prisms of size 25 mm. The separation of the first Stokes and its transportation to the target resulted in a power loss of $\sim 50\%$.

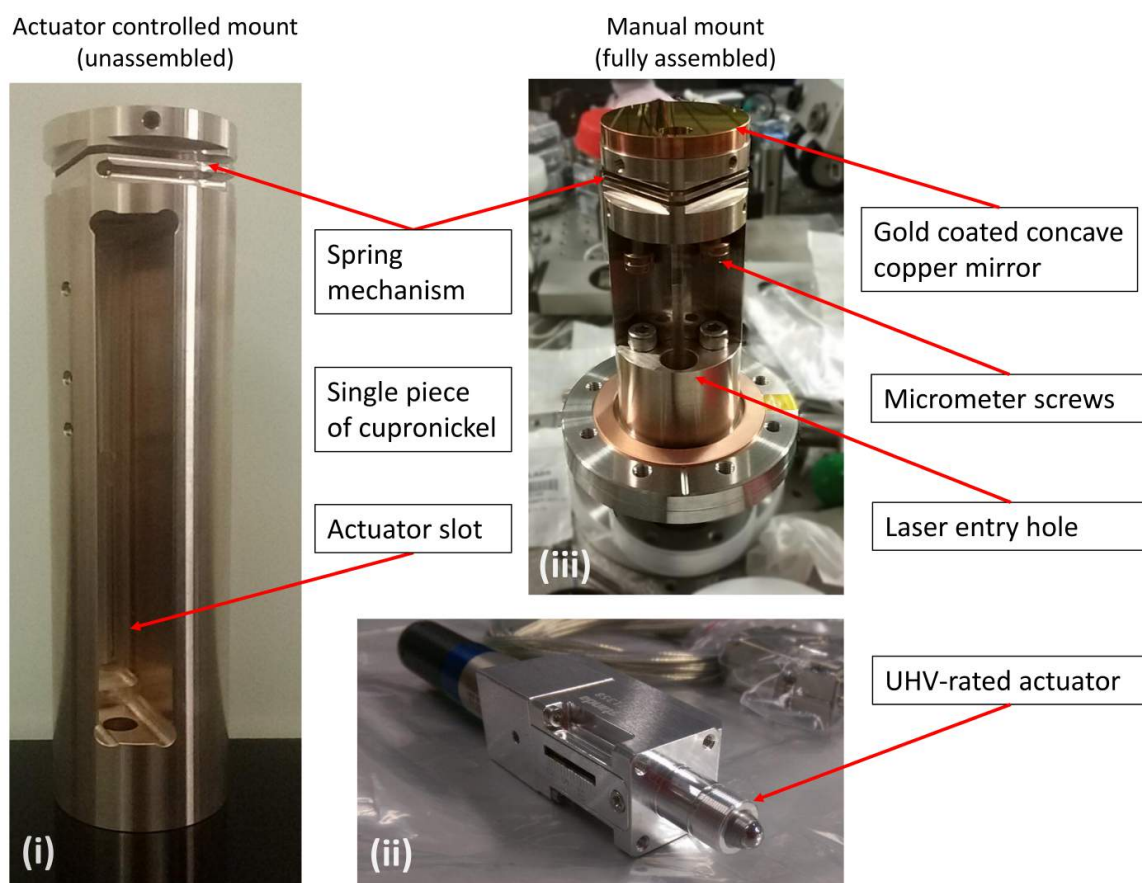


Figure 3.5.3: (i) Unassembled cupronickel mirror mount with actuator slots allowing for remote alignment in the high pressure H_2 atmosphere. The mount comprised a spring mechanism allowing for the mirror tilt and was manufactured in one piece. (ii) Second mirror mount using micrometer screws for mirror alignment. The mounts were directly bolted on a copper CF flange for maximum stability. Gold coated copper mirrors with 12 mm off axis holes were aligned with respect to laser entry holes. (iii) UHV actuator rated to 10^{-6} mbar. The actuator comprised a brushed DC motor operated at 12 V.

Chapter 4

Data analysis

4.1 Peak-to-total

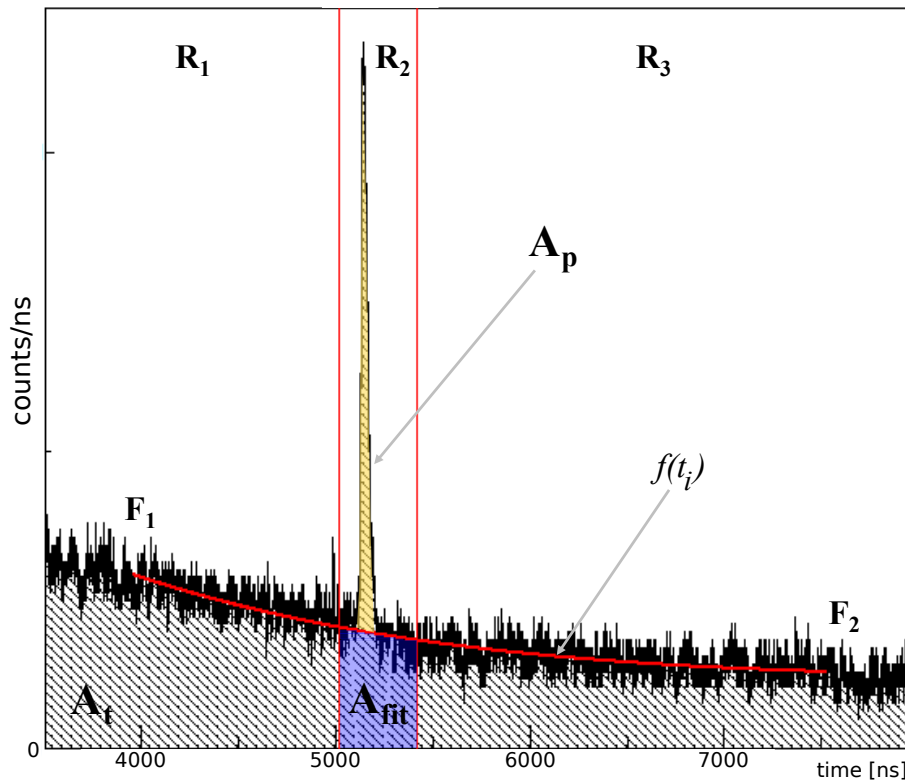


Figure 4.1.1: The DATS is fitted around the laser induced peak. The area under the peak A_p is obtained when the DATS value is subtracted from the fit value with the region R_2 . The ratio between A_p and the aggregate of all delayed annihilations in the DATS A_t provides the peak-to-total ($ptt = A_p/A_t$).

As explained in Sec. 1.6.2, $\bar{p}\text{He}^+$ in laser spectroscopy experiments the population

transfer from parent to daughter state is measured using the p_{tt} . The p_{tt} is defined within the DATS as the area under the forced annihilation peak A_p divided by the aggregate of the delayed component A_t , see Fig. 4.1.1.

$$p_{tt} = \frac{A_p}{A_t} \quad (4.1)$$

To access A_p we separated the peak from the residual DATS. For this we divided the DATS into three regions, denoted as R_1, R_2 and R_3 in Fig. 4.1.1. The peak region R_2 of length 400 ns defined by the laser timing t_{Las} was chosen such that it embraced the entire laser induced peak while R_1 and R_3 were lying to its respective sides. We now used the information in R_1 and R_3 to separate the residual from the laser induced peak in R_2 , i.e. we fitted the measured spectrum within a fitting window $[F_1, F_2]$ around the laser induced peak extending over R_1 and R_3 but excluding R_2 . The fit function $f(t)$ was then extended such that it filled the gap in R_2 . A_p was obtained as the difference between the area defined by the fit A_{fit} and the integral of all bins within R_2 as shown in Fig. 4.1.1.

$$A_p = A_{R_2} - A_{fit} = \sum_{R_2} b_i - \int_{R_2} f(t)dt \quad (4.2)$$

Analogously the integration over all bins b_i provided A_t

$$A_t = \sum_{R_1, R_2, R_3} b_i \quad (4.3)$$

It was noted that the p_{tt} was stable against the exact choice of the fit function as well as the size of the fitting window. In the work reported here we chose:

$$f(t, \vec{c}) = c_0 e^{c_1 t} + c_2 t \quad (4.4)$$

and a fitting window of 3 μs consistent with previous experiments reported in Refs. [16, 53, 86]

4.1.1 Uncertainty to the p_{tt}

In the limit of uncorrelated variables the total uncertainty to the p_{tt} is

$$\sigma_{p_{tt}} = \sqrt{\left(\frac{\sigma_{A_p}}{A_t}\right)^2 + \left(\frac{\sigma_{A_t}}{A_t^2}\right)^2} \quad (4.5)$$

It was noted that because A_t is very large with respect to σ_{A_t} , the second term could be neglected in the error treatment [87]. The uncertainty in the peak area σ_{A_p} is given by the uncertainty to its constituents as defined in Eq. 4.2:

$$\sigma_{A_p} = \sqrt{\sigma_{A_{R_2}}^2 + \sigma_{A_{fit}}^2} \quad (4.6)$$

$\sigma_{A_{R_2}}$ represents the uncertainty to the integral over all bins b_i within the peak window R_2 . We estimated it by appropriate scaling of the average bin uncertainty $\sigma_{\bar{b}}$

$$\sigma_{\bar{b}} = \frac{1}{N_b} \sum_{R_1, R_3} (b_i - f(t_i, \vec{c})) \quad (4.7)$$

such that

$$\sigma_{A_{R_2}} = \sqrt{\sum_{R_2} (\sigma_{\bar{b}})^2 \frac{b_i}{f(t_i, \vec{c})}} \quad (4.8)$$

where the number of considered bins N_b was used for normalization.

$\sigma_{A_{fit}}$ represents the uncertainty to the area defined by the fit $f(t, \vec{c})$ and the affiliated fit parameters $\vec{c} = \{c_1, c_2, c_3\}$. Under the assumption that \vec{c} is a Gaussian random vector, we obtained the respective covariance matrix V_{mn} using the CERN Minuit package [88]. The error matrix σ_{mn} was then obtained via multiplication of respective entries with the reduced χ_{red}^2 [89]

$$\sigma_{mn} = \sqrt{\chi_{red}^2 \times V_{mn}(\vec{c})} \quad (4.9)$$

where

$$\chi_{red}^2(\vec{c}) = \frac{1}{N_{df}} \sum_{[F_1, F_2] \setminus R_2} (b_i - f(t_i, \vec{c}))^2 \quad (4.10)$$

and N_{df} is the number of degrees of freedom. The uncertainty $\sigma_{A_{fit}}$ was then obtained via direct propagation of uncertainties

$$\sigma_{A_p} = \sqrt{\sum_{mn}^3 \frac{\partial A_p}{\partial c_m} \sigma_{m,n}^2 \frac{\partial A_p}{\partial c_n}} \quad (4.11)$$

4.1.2 Reproducibility of the p_{tt}

In Fig. 4.1.2 we show the measured p_{tt} with associated uncertainty for five antiproton shots. The shots were taken over a time period of five \sim hours. The target conditions as well as the laser timing $t_{Las} = 5.7\mu s$ were constant for all shots. It is seen that the

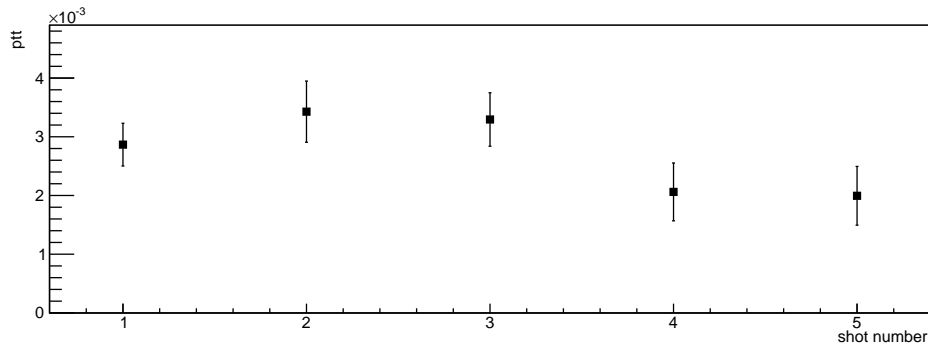


Figure 4.1.2: Peak-to-total (ptt) measured for five different antiproton shots at constant laser timing $t_{Las} = 5.7 \mu s$ and target conditions. The shots were taken over a time period of 5 h. The associated uncertainty is consistent with the reproducibility of the ptt .

error estimation is consistent with the reproducibility of the ptt . In the same figure we also show the respective measurements of the total DATS (A_t) which can serve as a measure for the antiproton bunch intensity.

4.2 Population evolution measurements

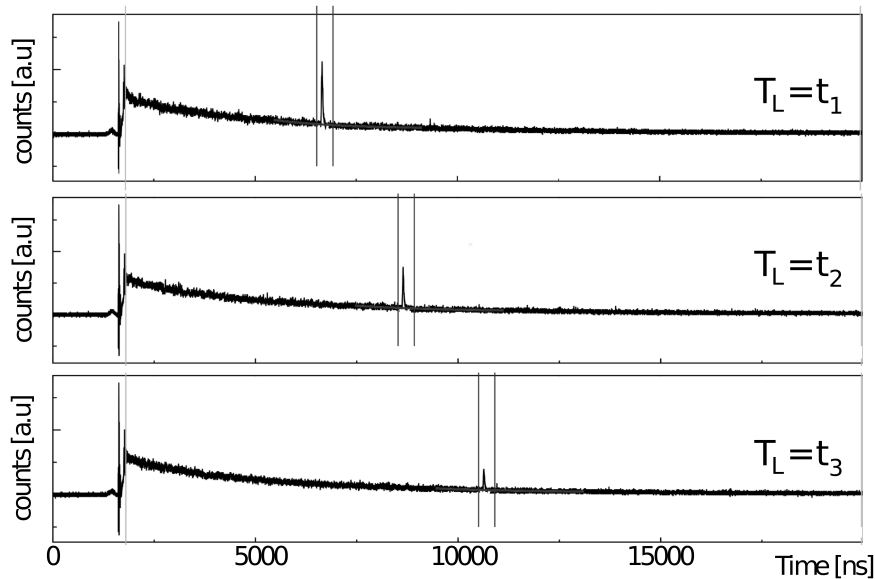


Figure 4.2.1: For population evolution measurements the laser timing was scanned against the antiproton arrival.

For population evolution measurements the laser timing t_{Las} was scanned with respect to the antiproton arrival at the helium target. For each antiproton shot the

ptt was identified and evaluated according to the analysis described above. As a first analysis step all time spectra were sliced into one hundred 200 ns long segments S_i , see Fig 4.2.2. Shots for which the forced annihilation peak was in the i^{th} segment were indexed $j = \{1, 2, \dots\}$ and combined using the weighted average calculation, where the squared uncertainty σ^2 served as weight:

$$\overline{ptt}_i = \frac{\sum_j \frac{ptt_j}{\sigma_j^2}}{\sum_j \frac{1}{\sigma_{ptt_j}^2}} \quad (4.12)$$

In an analogous treatment the laser timings t_{Las_j} were averaged for each timing segment S_i . In all population evolutions reported in this work we plot the thus averaged peak-to-total (\overline{ptt}_i) against the averaged laser timing (\overline{t}_i)

Since the individual measurement of the ptt have relatively large associated certainties we can assume that these dominate the overall uncertainty to \overline{ptt}_i rather than their distribution. $\overline{\sigma_{ptt}_i}$ can therefore be approximated as

$$\overline{\sigma_{ptt}_i} = \sqrt{\frac{1}{\sum_j \frac{1}{\sigma_j^2}}} \quad (4.13)$$

The uncertainty of the average laser timing $\overline{\sigma_{t_i}}$ has three contributions: (i) the pulse length of the antiproton pulse $\sigma_B \approx 200$ ns. (ii) the individual measurement uncertainties σ_{mes} (iii) the distribution of individual laser timings t_{Las_j} around the average value t_i . Among these σ_{mes} was negligibly small of order \lesssim ns. In the experiments we further chose $t_i - t_{Las_j} < 20$ ns such that

$$\overline{\sigma_{t_i}} \approx \sigma_B = 200 \text{ ns} \quad (4.14)$$

4.3 Offline antiproton shot rejection

In Fig. 4.3.1 we show how the antiproton beam intensity per shot was subject to larger fluctuation during a particularly bad day of beam time. In some other cases there was an additional trend towards lower intensities over a time period of several hours due to a continuous beam drift. Since beam tuning was an time consuming endeavor we only engaged in doing so when the average beam intensity dropped by $\sim 50\%$.

Antiproton pulses that lost part of their intensity during or after extraction

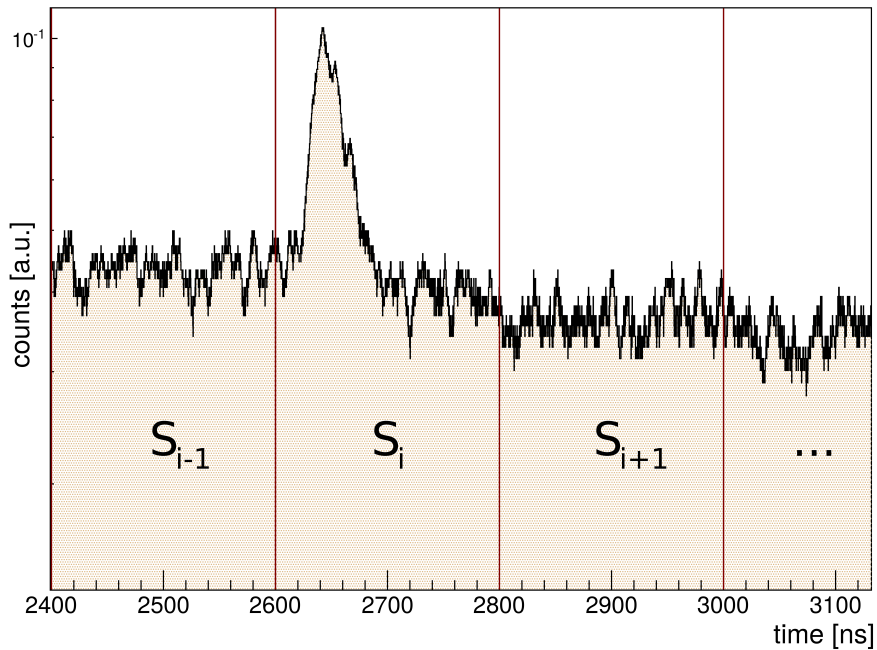


Figure 4.2.2: Section of the DATS containing the forced annihilation peak. For each antiproton shot the respective DATS was sliced into one hundred 200 ns long segments. Shots for which the forced annihilation peak was in the i^{th} segment were combined using the weighted average calculation.

however could not be identified online using the AD instrumentation at all. Instead they were identified offline by measuring the full aggregate of the DATS in terms of the A_t . In the analysis we rejected shots with intensities below 50% of the average A_t -value, see Fig. 4.3.1.

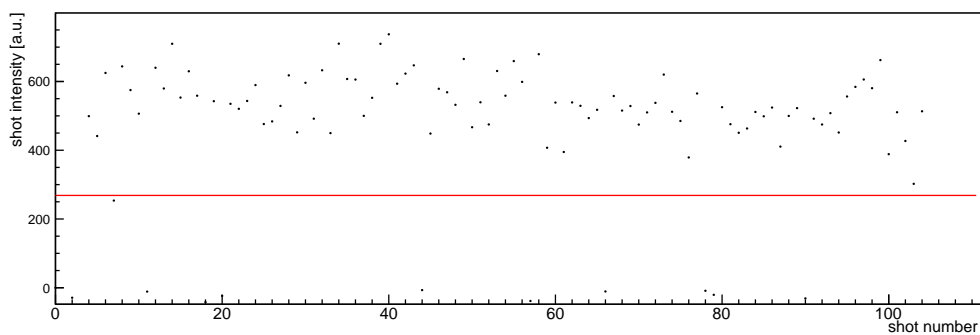


Figure 4.3.1: Antiproton intensity per bunch measured in terms of A_t . Shots with intensity below 50% of the average value were rejected in the offline analysis.

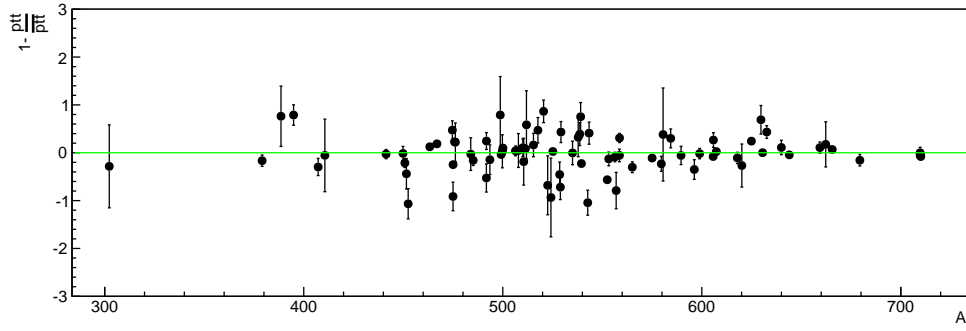


Figure 4.4.1: Deviation of the individual ptt measurements from the mean shown as a function of the antiproton bunch intensity A_t . No correlation between the two quantities is seen which shows that our definition of the ptt corrects for the antiproton beam intensity fluctuations reasonably well. The fluctuations of the laser pulse energy as well as the fluctuations of its spatial profile cannot be easily corrected for and are to a large part responsible to the remaining fluctuations.

4.4 Correlation of A_t to ptt

Here we show how the ptt as defined in Sec. 4.1 properly corrects for the fluctuation of the beam intensity. For this we calculated the deviation of each ptt -value from the average \overline{ptt} as defined for the respective annihilation class. The obtained deviation was normalized and plotted against the antiproton bunch intensity A_t as is shown in Fig. 4.4.1. If the intensity of antiproton bunch would be affecting the ptt a correlation of the two in form of a slope in regarded plot would be seen. Instead the individual values for $1 - ptt/\overline{ptt}$ are homogeneously distributed around zero independent of the antiproton bunch intensity. Uncorrelated deviations from zero are explained by fluctuation in the laser pulse energy and spatial profile. The associated errors differ in size depending on the given strength of the ptt which is not visible in the plot due to normalization.

4.5 Cascade model

It has been shown that the population time evolution of $\bar{p}\text{He}^+$ states can be well described in a simplified cascade model that assumes a single decay chain i.e. a sole ladder which feeds lower lying states from above, see Fig 4.5.1 [90–92]. At the end of this ladder there is always an Auger dominated state, which is the only state from which antiproton annihilation occurs. The corresponding differential equations to an

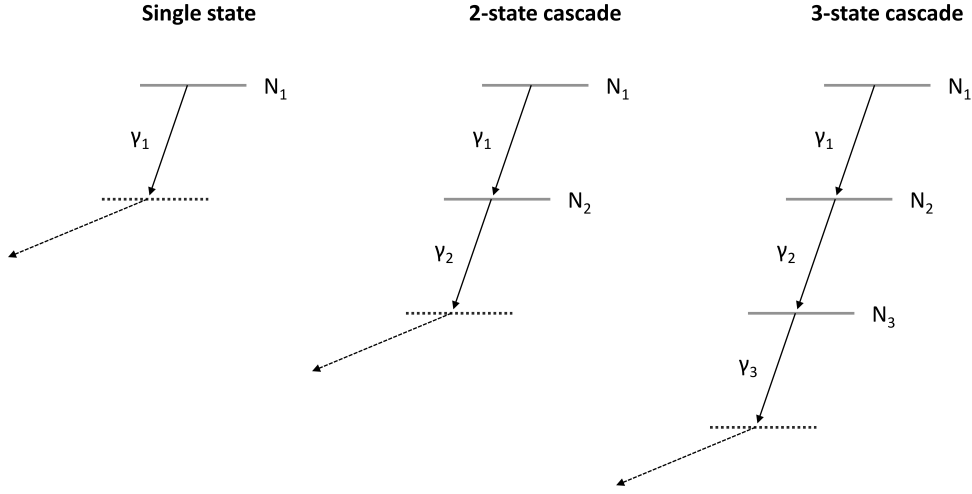


Figure 4.5.1: The population evolution of $\bar{p}\text{He}^+$ states was described by one of three simplified cascade models in which a single decay chain was assumed.

exemplary 3 state model are

$$\frac{dN_1}{dt} = -\gamma_1 N_1 \quad (4.15)$$

$$\frac{dN_2}{dt} = \gamma_1 N_1 - \gamma_2 N_2 \quad (4.16)$$

$$\frac{dN_3}{dt} = \gamma_2 N_2 - \gamma_3 N_3 \quad (4.17)$$

where N_1, N_2, N_3 and $\gamma_1, \gamma_2, \gamma_3$ denote the respective initial populations and decay rates. This set of differential equations can be solved via direct integration such that

$$N_1(t) = N_1^0 e^{-\gamma_1 t} \quad (4.18)$$

$$N_2(t) = N_1^0 \frac{\gamma_1}{(\gamma_2 - \gamma_1)} e^{-\gamma_1 t} + \left(N_2^0 - N_1^0 \frac{\gamma_1}{\gamma_2 - \gamma_1} \right) e^{-\gamma_2 t} \quad (4.19)$$

$$N_3(t) = N_1^0 \frac{\gamma_1 \gamma_2}{(\gamma_2 - \gamma_1)(\gamma_3 - \gamma_1)} e^{-\gamma_1 t} + \left(N_2^0 - N_1^0 \frac{\gamma_1}{\gamma_2 - \gamma_1} \right) \frac{\gamma_2}{\gamma_3 - \gamma_2} e^{-\gamma_2 t} + \left[N_3^0 - N_1^0 \frac{\gamma_1 \gamma_2}{(\gamma_2 - \gamma_1)(\gamma_3 - \gamma_1)} - \left(N_2^0 - N_1^0 \frac{\gamma_1}{\gamma_2 - \gamma_1} \right) \frac{\gamma_2}{\gamma_3 - \gamma_2} \right] e^{-\gamma_3 t} \quad (4.20)$$

where N_i^0 denotes the population in the i^{th} state at $t = 0$. All population evolution measurements reported in this work were fitted with one of these three cascade models.

The least squares method was applied under minimization of the weighted χ_{red}^2

$$\chi_{red}^2(\vec{\gamma}, \vec{N}_0) = \frac{1}{N_{df}} \sum_i \frac{(\overline{ptt}_i - N(t, \vec{\gamma}, \vec{N}_0))^2}{\overline{\sigma}_{ptt_i}} \quad (4.21)$$

The corresponding uncertainty was obtained in a similar way as outlined Sec. 4.1.1 where the covariance matrix $V_{mn}(\gamma_1)$ was retrieved with the CERN Minuit package [88] while the respective diagonal matrix element was multiplied with χ_{red}^2 .

4.5.1 Extraction of cascade lifetimes

In the analysis we fitted the measured population evolutions with the simplest cascade model that could still describe the data such that ($\chi_{red}^2 < 1$). We then extracted γ_3 which is the inverse cascade lifetime τ^{cas} of the parent state of measured transition. As explained in Sec. 1.6.2 the cascade lifetime is defined by (i) the depletion of the state via Auger and radiative deexcitation under the lifetime $\tau^{dep} = (\gamma_A + \gamma_{rad})^{-1}$ (ii) the feeding into the state (n, ℓ) from higher lying states of the same decay chain and (iii) potential quenching effects. It is essential to note that if the state (n, ℓ) is neither subject to feeding nor quenching, then the cascade lifetime is identical to the depletion lifetime $\tau^{cas} \stackrel{!}{=} \tau^{dep}$ while a strong excess of the cascade lifetime on the other hand will indicate substantial feeding from populations in higher lying states. We compared the measured cascade lifetimes τ^{cas} to the theoretically predicted depletion lifetimes τ^{dep} to quantify the degree of feeding into that state.

4.5.2 Reverse analysis

We applied a reverse analysis to measurements which were fitted with a two or three state cascade model. Here we fixed the decay rates of the lower lying states $\gamma_{2,3}$ to the theoretical value and let γ_1 be the free parameter. The obtained value for γ_1 was inverted to provide the cascade lifetime of the respective high lying state. In an analogous treatment to the above this value could then be compared to the corresponding depletion lifetime from theoretical calculations in order to estimate the feeding into that state.

4.5.3 Extraction of capture probabilities

The capture probabilities of an antiproton into a $\bar{p}\text{He}^+$ state (n, ℓ) is proportional to the population in that state at $t = 0$. The extraction of absolute populations in individual states however is a delicate endeavor that is possible only if the total trapping fraction f_{trap} is known, see Sec. 1.6. Since this value has not been measured for our setup yet, we constrained our analysis to relative capture rates only. These are directly given by the ratio of the respective parameters N_i^0 in the two and three state cascade models. The associated statistical uncertainties were determined in an analogous treatment as in the above. To check for large systematic errors we applied this analysis procedure to previous data from Ref. [18] for which a full study of the populations had been performed where we found the previous results to be reproduced within the margin of uncertainty.

Chapter 5

Results

5.1 Data taking

We carried out population evolution measurements distributed over four eight hour shifts. The first ~ 30 shots of each shift were dedicated to the tuning of the antiproton beam on the helium target. Fluctuations of the beam intensity and spatial profile together with the low repetition rate complicated this task. Normally the bunch intensity was $1 \pm 0.4 \times 10^6 \bar{p}$ /bunch at kinetic energy $E_{\bar{p}} \approx 75$ keV and $f_{rep} \approx 0.01$ Hz repetition rate. Low intensity antiproton shots could be identified within the AD deceleration cycle using longitudinal Schottky pick-up electrodes and were rejected online [93]. Retuning of the beam was carried out whenever the BPMs showed a spatial drifting of $\gtrsim 1$ cm or an intensity drop of $\geq 50\%$.

The temperature and pressure of the helium target were continuously monitored while remote control of the coolant flow allowed for small corrections. In all reported measurements identical target conditions were ensured, i.e. constant target temperature $T = 1.50 \pm 0.05$ K and pressure $P = 1.10 \pm 0.05$ mbar. The helium and nitrogen reservoir of our cryocooler were refilled before each shift. Due to the high helium consumption a second filling was necessary during data taking for which the measurements were halted. This procedure typically took ~ 20 min.

The pulse energy of the laser beam was measured at the beginning and middle of each shift, and another time during the refilling of the helium reservoir. Additionally the photodiode located in the experimental zone recorded every laser shot providing information on the pulse energy and pulse length. This was particularly helpful to reject shots for which one of the lasers had dropped out of lock.

We measured the peak-to-total as a function of the laser timing from $t_{Las} \sim 100$ ns after antiproton arrival, up to a large t_{Las} value where no laser induced peak could be observed. We incremented t_{Las} in step sizes of $0.1 \mu\text{s}$ for very early times when distinct features were visible in the population evolution and a step size of $0.5 \mu\text{s}$ elsewhere. Each point was measured 3 – 5 times while the intervals between individual measurements of the same point were spaced by at least 2 hours.

5.2 Comparison of signal strength

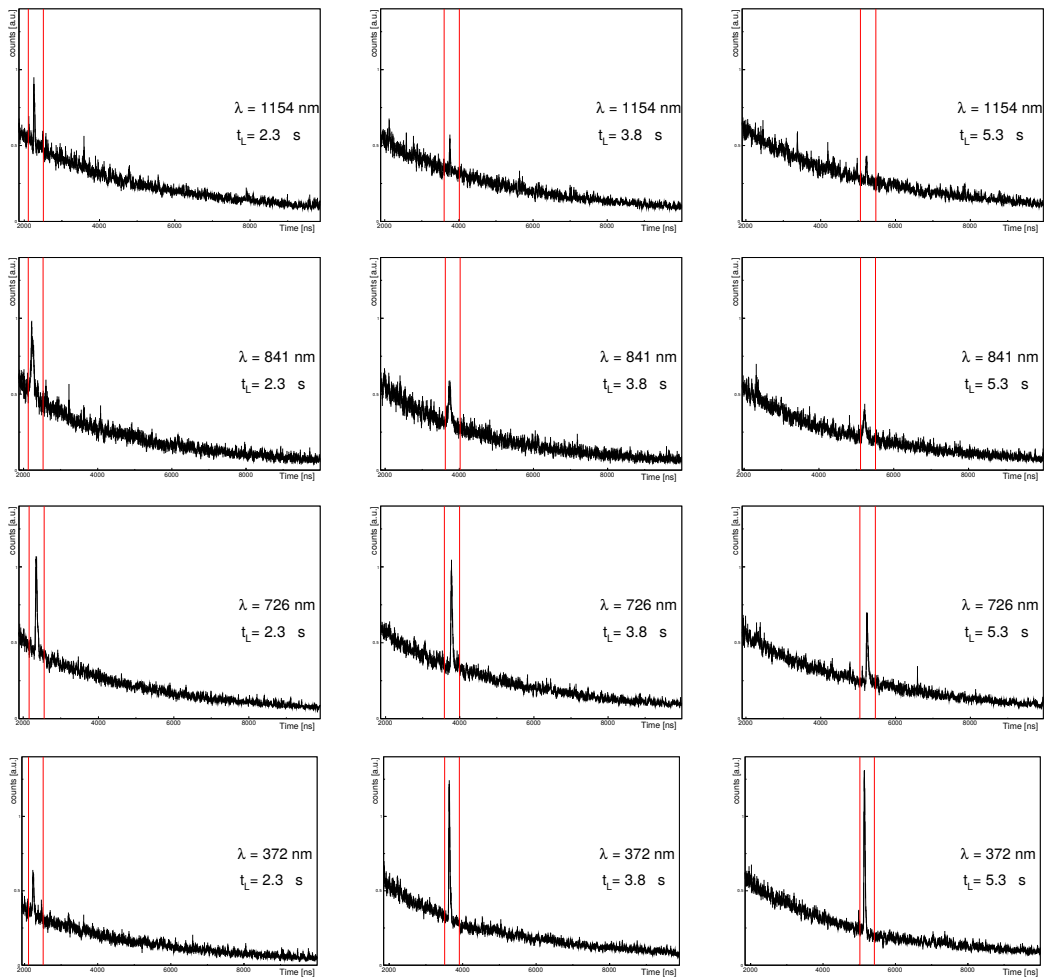


Figure 5.2.1: Normalized annihilation time spectra with the laser induced peak at $t_{Las} = 2.3, 3.8$ and $5.3 \mu\text{s}$

We measure four transitions at $\lambda = 1154, 841, 726$ and 372 nm. In Fig. 5.2.1 we show the respective DATS for varying laser timings $t_{Las} = 2.3, 3.8$ and $5.3 \mu\text{s}$ with respect

to the antiproton bunch arrival at the target. It is seen how the induced peaks under the transitions at 1154 nm and 841 nm decrease as t_{Las} is incremented, while peaks induced via the 726 nm transition are of similar strength at $t_{Las} = 2.5$ and $3.9 \mu\text{s}$. Unlike the others the peak under the 372 nm transition gains in strength with t_{Las} and reaches maximum between 3.8 and $5.3 \mu\text{s}$.

5.3 Population evolution measurements

We carried out population evolution measurements at the lowest target density $\rho_L = 5 \times 10^{18} \text{ cm}^{-3}$ and atomic collision rate $\nu_L = 5 \times 10^6 \text{ s}^{-1}$ studied so far. The raw data was obtained under the experimental conditions of Sec. 5.1 using the experimental apparatus described in Chapter 3 and analyzed as explained in Chapter 4. In the following figures the normalized peak-to-total which is proportional to the absolute number of $\bar{\text{p}}\text{He}^+$ atoms captured in that particular state is plotted against the laser probing time t_{Las} . Population evolution measurements obtained in this way are compared to previous measurements carried out at high density. These previous measurements studying the states (38, 35), (37, 35) and (35, 33) determined absolute capture probabilities but had larger associated uncertainties than the relative measurements presented here. Both, low and high density population evolution measurements were fitted with cascade models described in Sec. 4.5 such that the cascade lifetimes τ^{cas} of the investigated states could be extracted. The respective values for the two density sets were compared to each other and to the theoretically expected depletion lifetimes τ^{dep} of the parent state. In addition we applied a reverse analysis to the population evolution measurements of the states (38, 35) and (37, 35) such that the τ^{cas} of (39, 36) and (39, 37) could be extracted. Due to the nature of the analysis these cascade lifetimes must be compared to the respective radiative lifetimes τ^{rad} as the reverse analysis is not sensitive to the Auger decay rate.

5.3.1 $(n, \ell)=(40, 36)$; $\lambda = 1154 \text{ nm}$

In the high n region we measured the $(40, 36) \rightarrow (41, 35)$ transition at the transition wavelength $\lambda = 1154 \text{ nm}$. The parent state lies in the $v = 3$ decay chain and at the energetically upper edge of the known region of metastability. Previous high density measurements at $\rho_{H1} = 1 \times 10^{21} \text{ cm}^{-3}$ revealed how the population in this state decays exponentially [43].

In Fig. 5.3.1 we show new low and previous high density population evolu-

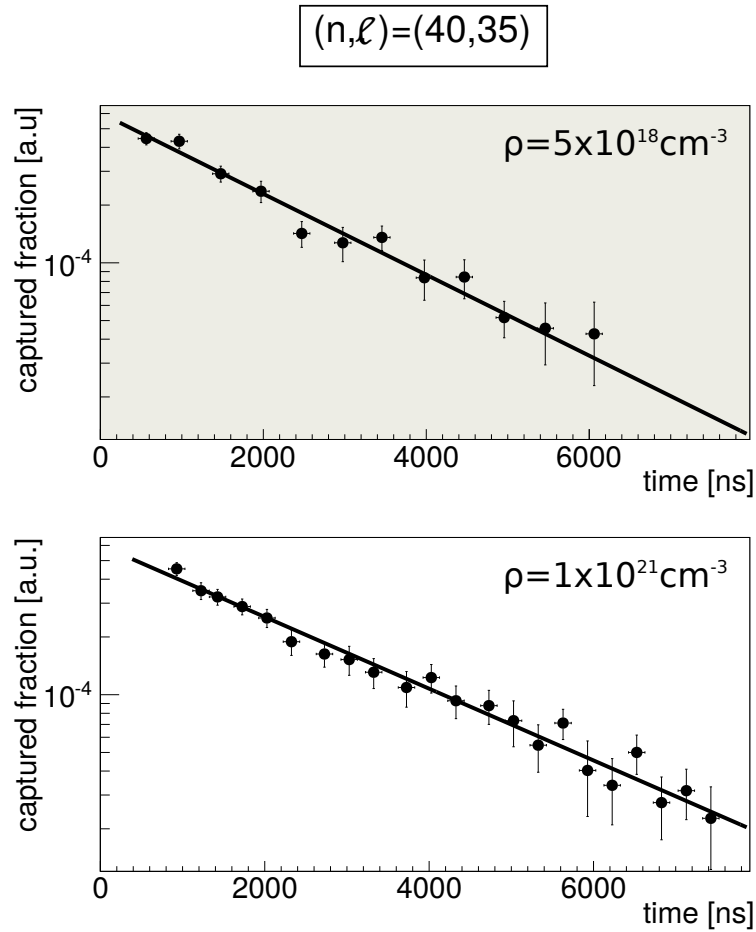


Figure 5.3.1: Comparison of the population evolution in the $(40, 36)$ state measured at $\rho_L = 5 \times 10^{18} \text{ cm}^{-3}$ (top) and $\rho_{H1} = 1 \times 10^{21} \text{ cm}^{-3}$ (bottom). Both time spectra are well described using the single state cascade model. The obtained cascade lifetimes are $\tau_{\rho_L}^{cas}(40, 36) = 2.2 \pm 0.2 \mu\text{s}$ and $\tau_{\rho_{H1}}^{cas}(40, 36) = 2.1 \pm 0.2 \mu\text{s}$ respectively.

tion measurements. At low density the population decayed as a single exponential of lifetime $\tau_{\rho_L}^{cas}(40, 36) = 2.2 \pm 0.2 \mu\text{s}$. Fitting the previous high density measurement with the same cascade model yielded $\tau_{\rho_{H1}}^{cas}(40, 36) = 2.1 \pm 0.2 \mu\text{s}$.

If the $n \geq 41$ states of the $v = 3$ decay chain were highly populated, their feeding into $(40, 36)$ would result in a deviation of the corresponding population evolution from a simple exponential decay. No obvious deviation was observed. The comparison of the measured cascade lifetimes with the theoretical depletion lifetime $\tau_{theo}^{dep}(40, 36) = 1.62 \mu\text{s}$ is consistent with small populations in higher lying states of this decay chain.

5.3.2 $(n, \ell) = (38, 35)$; $\lambda = 841$ nm

In the medium n region we studied the $(38, 35)$ state. This state is in proximity to the theoretical population maximum at $n \approx 38.2$. Previous high density measurements of this state had employed the $(38, 35) \rightarrow (37, 34)$ transition at wavelength $\lambda = 529$ nm which is of favored type and takes advantage of the density dependent lifetime shortening in $(37, 34)$ [18]: the transition only becomes amenable to laser spectroscopy at sufficiently high target densities $\rho_{H_2} \geq 2 \times 10^{21}$ cm $^{-3}$. These measurements revealed a large initial capture probability in $(38, 35)$ followed by an exponential decay was observed.

In Fig. 5.3.2 we compare newly obtained low density measurements at ρ_L under the $(38, 35) \rightarrow (39, 34)$ transition of 841 nm wavelength to the previous measurements of the 529 nm transition at high density. We fitted the low density measurement with a two state cascade model which considered feeding from the higher lying $(39, 36)$ state and obtained the cascade lifetime $\tau_{\rho_L}^{cas}(38, 35) = 2.3 \pm 0.3$ μ s in this way. A fit of the high density measurement with the same cascade model on the other hand provided $\tau_{\rho_{H_2}}^{cas}(38, 35) = 2.0 \pm 0.2$ μ s.

Theoretical calculations predict a comparably small depletion lifetime of only $\tau_{theo}^{dep}(38, 35) = 1.49$ μ s for $(38, 35)$. This value is substantially smaller than $\tau^{cas}(38, 35)$ which suggest some feeding from states above $n = 39$ in the $v = 2$ decay chain, which were not considered in the cascade model that was used for fitting. We performed a reverse analysis of the population evolution in $(38, 35)$ and found $\tau_{\rho_L}^{cas}(39, 36) = 2.6 \pm 0.4$ μ s at low and $\tau_{\rho_{H_2}}^{cas}(39, 36) = 3.4 \pm 0.3$ μ s for the state $(39, 36)$ at high density. Comparing these values with the theoretically calculated radiative lifetimes $\tau^{rad}(39, 36) = 1.77$ indicates some feeding from the state $(40, 37)$.

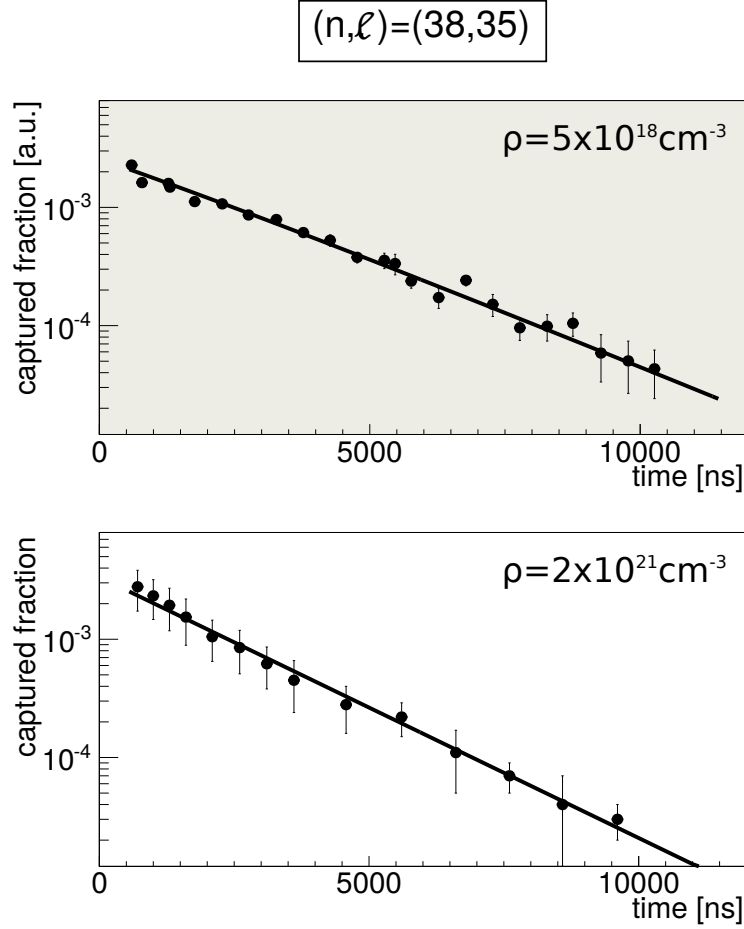


Figure 5.3.2: Population evolution in the $(38, 35)$ state measured at density $\rho_L = 5 \times 10^{18} \text{ cm}^{-3}$ under the 841 nm transition (top) and $\rho_{H2} = 2 \times 10^{21} \text{ cm}^{-3}$ under the 529 nm transition (bottom). The measurements were fitted with the same two state cascade model providing the associated cascade lifetimes $\tau_{\rho_L}^{cas}(38, 35) = 2.3 \pm 0.3 \mu\text{s}$ and $\tau_{\rho_{H2}}^{cas}(38, 35) = 2.0 \pm 0.2 \mu\text{s}$

5.3.3 $(n, \ell) = (37, 35)$; $\lambda = 726 \text{ nm}$

We next measured the $(37, 35) \rightarrow (38, 34)$ transition at wavelength $\lambda = 726 \text{ nm}$. Previous high density measurements of this transition at $\rho_{H3} = 6 \times 10^{20} \text{ cm}^{-3}$ had revealed an initially constant population evolution followed by an exponential decay.

A comparison between new low and previous high density measurements is given in Fig. 5.3.3. The low density population evolution was also found to be constant for the first $\sim 200 \text{ ns}$ before decaying exponentially. We fitted the data with a three state cascade model and found the cascade lifetime to be $\tau_{\rho_L}^{cas}(37, 35) = 2.6 \pm 0.3 \mu\text{s}$ at low and $\tau_{\rho_{H3}}^{cas}(37, 35) = 2.7 \pm 0.3 \mu\text{s}$ at high density.

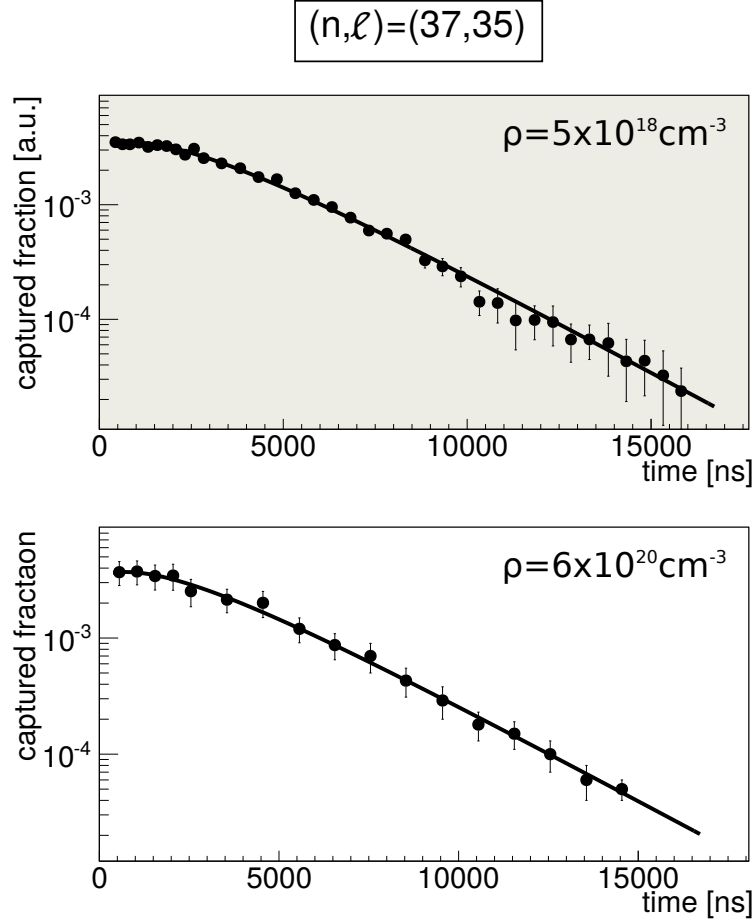


Figure 5.3.3: Population evolution of the $(37, 35)$ state measured at densities $\rho_L = 5 \times 10^{18} \text{ cm}^{-3}$ (top) and $\rho_{H3} = 6 \times 10^{20} \text{ cm}^{-3}$ (bottom). A fit with a three state cascade model was applied to the low density measurement providing the cascade lifetime $\tau_{\rho_L}^{cas}(37, 35) = 2.6 \pm 0.3 \mu\text{s}$. When applying the same cascade model to previous high density measurement we found $\tau_{\rho_{H3}}^{cas}(37, 35) = 2.7 \pm 0.3 \mu\text{s}$.

The initial constant population evolution can be explained by the strong feeding from the highly populated $(38, 36)$ state canceling out the exponential decay in $(37, 35)$ at early times after formation. The comparably small theoretical depletion lifetime $\tau_{theo}^{dep}(37, 35) = 1.39 \mu\text{s}$ further indicates strong feeding from higher lying states. In a reverse analysis we obtained the $\tau_{\rho_L}^{cas}(39, 37) = 2.5 \pm 0.4 \mu\text{s}$ and $\tau_{\rho_{H3}}^{cas}(39, 37) = 2.1 \pm 1.3 \mu\text{s}$, which compared to the corresponding theoretical value $\tau_{theo}^{rad}(39, 37) = 1.70 \mu\text{s}$ indicates some feeding population from $(40, 38)$.

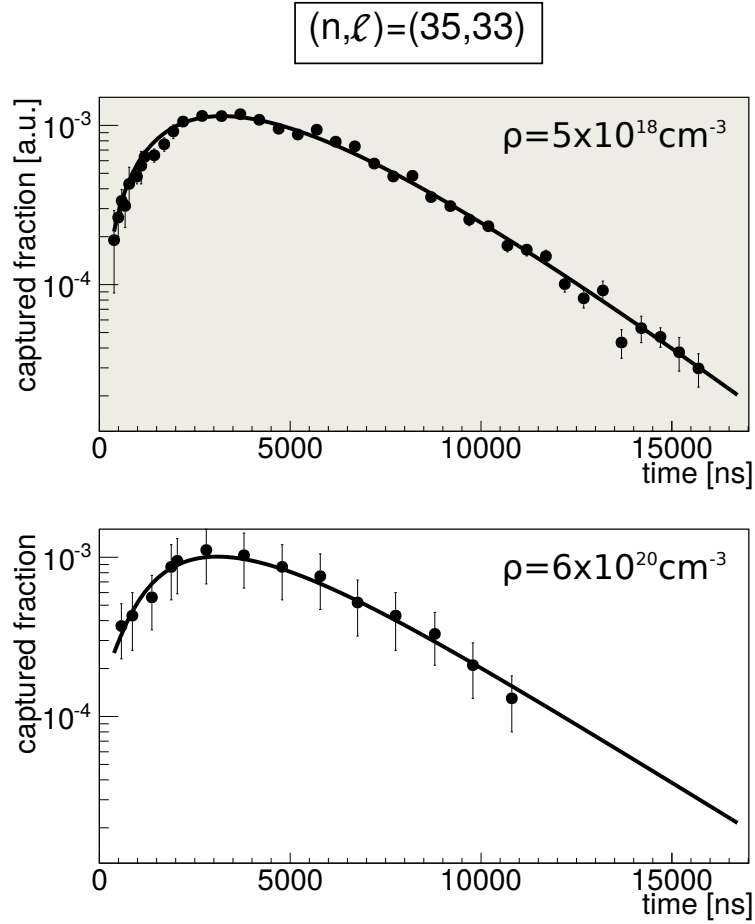


Figure 5.3.4: Population evolution of the $(35, 33)$ state measured at densities $\rho_L = 5 \times 10^{18} \text{ cm}^{-3}$ (top) and $\rho_{H1} = 6 \times 10^{20} \text{ cm}^{-3}$ (bottom). Both population evolutions showed a curved structure with little initial population $t = 0$ and a maximum at $t_{Las} \approx 4 \mu\text{s}$. We fitted a three state cascade model to the population evolutions and obtained the cascade lifetimes $\tau_{\rho_L}^{cas}(35, 33) = 2.9 \pm 0.3 \mu\text{s}$ and $\tau_{\rho_{H3}}^{cas}(35, 33) = 2.8 \pm 0.3 \mu\text{s}$

5.3.4 $(n, \ell) = (35, 33)$; $\lambda = 372 \text{ nm}$

In the low n region we studied the $(35, 33)$ state using the $(35, 33) \rightarrow (34, 32)$ transition at wavelength $\lambda = 372 \text{ nm}$. Contrary to the other transitions presented in this work, this one is of favored type and lies at the end of the $v = 1$ decay chain. Previous high density measurements at ρ_{H3} had revealed a curved structure of the population evolution which peaked at $t_{Las} \approx 4 \mu\text{s}$ [18].

A comparison of new low density measurements at ρ_L to the previous high density measurements is provided in Fig. 5.3.4. The population evolution at ρ_L showed little

initial population which gradually increased with t_{Las} . The maximum was reached at $t_{Las} \approx 4 \mu s$ before the population decreased exponentially. The measurement was fitted with a three state cascade model which included feeding from the two higher lying states and provided the low density cascade lifetime $\tau_{\rho_L}^{cas}(35, 33) = 2.9 \pm 0.3 \mu s$. Applying the same fit to the high density measurement yielded $\tau_{\rho_{H3}}^{cas}(35, 33) = 2.8 \pm 0.3 \mu s$.

The structure of the population evolution indicates how a negligible number of $\bar{p}He^+$ atoms are initially captured into (35, 33) while the majority of the population is due to the cascade of higher lying states in the $v = 1$ decay chain. The theoretical depletion lifetime $\tau_{theo}^{dep}(35, 33) = 0.99 \mu$ is only $\sim 1/3$ of the measured cascade lifetime.

5.4 Relative capture probabilities for $v = 1, 2$

From the low density measurements we extracted the relative capture probabilities using the analysis as explained in Sec. 4.5.3. The obtained values were normalized to that of the $n = 38$ state in the respective decay chain. For the $v = 1$ states we combined the measurements from the $\lambda = 726$ and $\lambda = 327$ transition and found the capture probability to peak at $n = 38$ with $(55 \pm 7)\%$ and $(81 \pm 9)\%$ of the peak value in the $n = 39$ and $n = 37$ state respectively. On the other hand only negligible capture probabilities were measured in the states of $n = 35$ and $n = 36$. Within the $v = 2$ decay chain we found the capture probability in the $n = 39$ state to be only 29% of that in the $n = 38$ state.

The low density results are compared to previous high density measurements in Table 5.1 and in Fig. 5.4.1. The high density values in the $v = 1$ decay chain were consistent with those at low density, including the peak at $n = 38$ as well as the small populations in the low n states $n = 36$ and $n = 35$. The relative capture probabilities in the states with $n = 39$ and $n = 37$ were $(42 \pm 12)\%$ and $(65 \pm 12)\%$ respectively. In the $v = 2$ decay chain high density measurements revealed how the capture probability in the $n = 39$ state was $(40 \pm 10)\%$ of that in the $n = 38$ state.

Table 5.1: Relative capture probability normalized to the value at $n = 38$

decay chain	N_{39}^0/N_{38}^0	N_{38}^0/N_{38}^0	N_{37}^0/N_{38}^0	N_{36}^0/N_{38}^0	N_{35}^0/N_{38}^0
low density $\rho_L = 5 \times 10^{18} \text{ cm}^{-3}$					
$v = 1$	0.55 ± 0.07	1.0 ± 0	0.81 ± 0.09	0.030 ± 0.009	0.027 ± 0.009
$v = 2$	0.29 ± 0.06	1.0 ± 0			
high density $\rho_{H3} = 6 \times 10^{20} \text{ cm}^{-3}$ [18]					
$v = 1$	0.42 ± 0.12	1.0 ± 0	0.65 ± 0.12	0.055 ± 0.01	0.04 ± 0.01
high density $\rho_{H2} = 2 \times 10^{21} \text{ cm}^{-3}$ [18]					
$v = 2$	0.40 ± 0.10	1.0 ± 0			

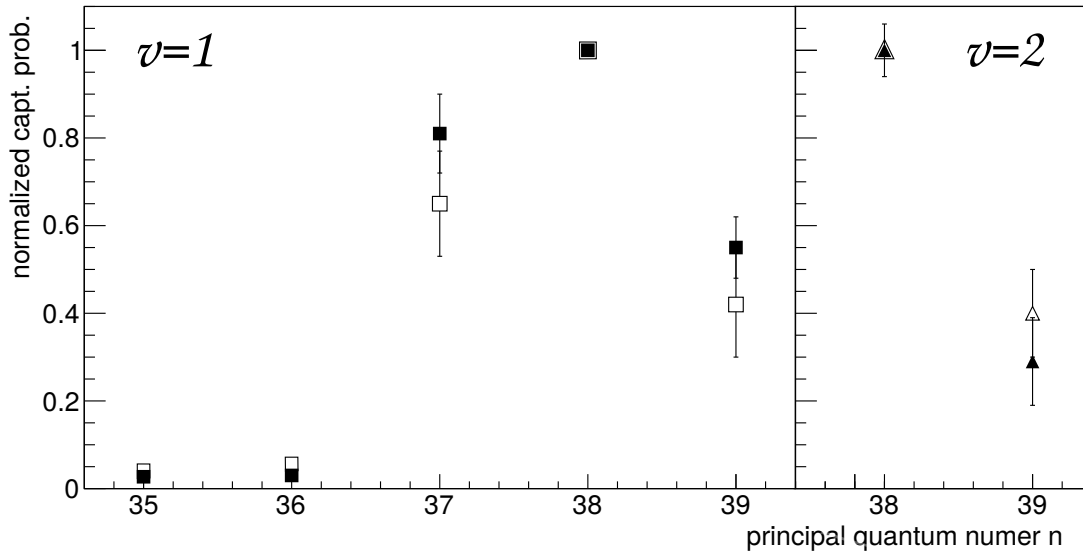


Figure 5.4.1: Relative capture probabilities in the $v = 1$ (squares) and 2 (triangles) decay chain normalized to the respective value of the $n = 38$ state. Measurements at low density $\rho_L = 5 \times 10^{18} \text{ cm}^{-3}$ are denoted by filled symbols (\blacksquare , \blacktriangle) while we used empty squares (\square) for $\rho_{H3} = 6 \times 10^{20} \text{ cm}^{-3}$ and triangles (\triangle) for $\rho_{H2} = 2 \times 10^{21} \text{ cm}^{-3}$, measurements obtained from Ref. [18]

5.5 Summary

We reported population evolution measurements of $\bar{\text{pHe}}^+$ atoms using laser spectroscopy at the lowest target density $\rho = 5 \times 10^{18} \text{ cm}^{-3}$ studied so far.

We compared these measurements at low density to previous high density measurements at $\rho = 6 \times 10^{20} - 2 \times 10^{21} \text{ cm}^{-3}$ where we found all features of the individual population evolutions to be retained irrespective of the target density. The cascade lifetimes of four states were obtained by fitting of the measurements with appropriate cascade models. The retrieved low density cascade lifetimes ranged from $\tau^{cas} = 2.1 \pm 0.2 \mu\text{s}$ in the (40, 36) state to $2.9 \pm 0.3 \mu\text{s}$ in the (35, 33) with intermediate values of $2.3 \pm 0.3 \mu\text{s}$ and $2.6 \pm 0.3 \mu\text{s}$ in the (38, 35) and (37, 35) state. Within their margins of uncertainty these values were found to remain constant with regards to the target density. The measured cascade lifetimes as a function of the principal quantum number n for both density sets are shown in Fig. 5.5.1.

In a reverse analysis we obtained the cascade lifetimes of (39, 36) at $\tau = 2.6 \pm 0.4 \mu\text{s}$ and (39, 37) at $2.1 \pm 0.4 \mu\text{s}$. We compared all the experimental cascade lifetimes to the theoretically predicted depletion τ^{dep} and radiative lifetimes τ^{rad} , as shown in Table 5.2. Measured cascade lifetimes exceeding the corresponding depletion lifetimes, indicate feeding from higher lying states. We found this excess to gradually decrease towards states of higher n from $\Delta\tau = \tau^{cas} - \tau^{dep} = 1.9 \mu\text{s}$ for $n = 35$ compared to $\Delta\tau = 0.5$ for $n = 40$. This behavior indicates reduced populations in the $n \geq 41$ region and was reproduced in terms of magnitude and direction irrespective of the target density.

We retrieved the relative capture probabilities in $v = 1$ and 2 decay chain and compared the respective results obtained from low and high density measurements. In the $v = 1$ decay chain we found the distribution of the capture probability to remain constant irrespective of the target density including its peak at $n = 38$ and small values for $n = 35$ and 36. In the $v = 2$ decay chain we found the relative capture probability in the $n = 39$ state with respect to the $n = 38$ state to be comparable at low and high density: $(29 \pm 6)\%$ compared to $(40 \pm 12)\%$.

None of these experimental findings suggests a density dependence of the cascade lifetimes or population distribution of the $\bar{\text{pHe}}^+$ atom within the studied density range.

Table 5.2: Tabular comparison of cascade lifetimes obtained at low and high density to the theoretically calculated lifetimes

state (n, ℓ)	high density		low density		$\tau^{rad}[\mu s]$	theory	
	$\tau^{cas}[\mu s]$	$\rho[\text{cm}^{-3}]$	$\tau^{cas}[\mu s]$	$\rho[\text{cm}^{-3}]$		$\tau^A[\mu s]$	$\tau^{dep}[\mu s]$
(40,36)	2.2±0.2	1×10^{21}	2.1±0.2	5×10^{18}	1.86 [19]	12.6 [94]	1.62
(38,35)	2.0±0.2	2×10^{21}	2.3±0.3	5×10^{18}	1.52 [19]	90.1 [29]	1.49
(37,35)	2.7±0.3	6×10^{20}	2.6±0.3	5×10^{18}	1.39 [19]	156000 [29]	1.39
(35,33)	2.8±0.3	6×10^{20}	2.9±0.3	5×10^{18}	1.25 [19]	4.76 [95]	0.99
reverse analysis							
(39,36)	2.4±0.4	6×10^{20}	2.6±0.4	5×10^{18}	1.77 [19]	-	-
(39,37)	2.5±0.4	6×10^{20}	2.1±0.4	5×10^{18}	1.70 [19]	-	-

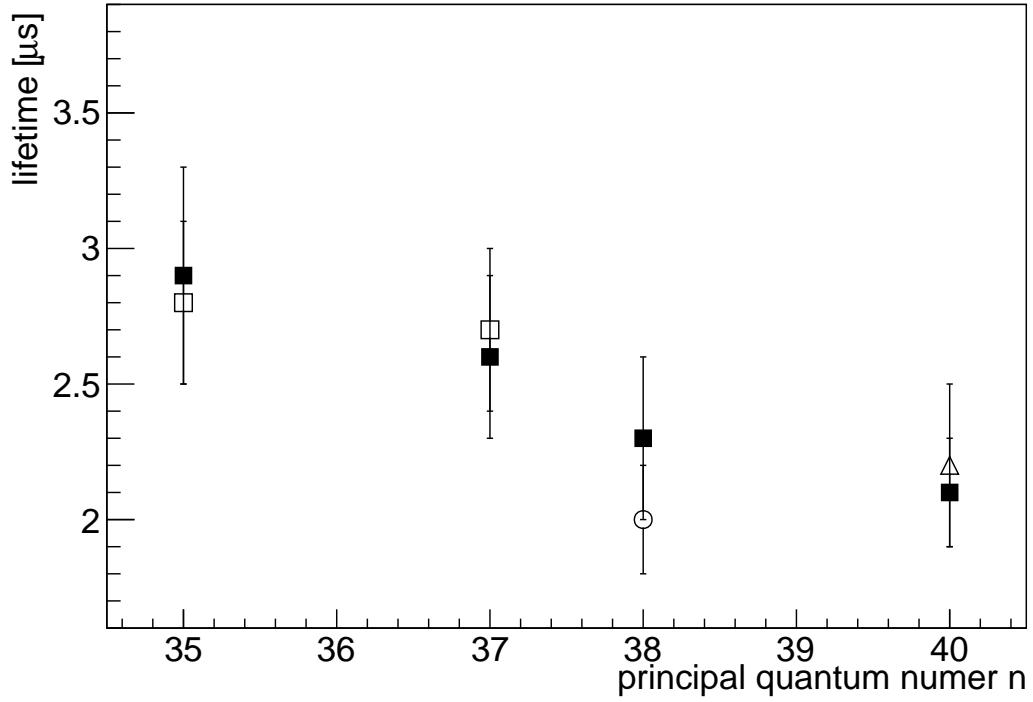


Figure 5.5.1: Cascade lifetimes obtained at low density in the 2015 run at the CERN AD compared to previous high density measurements: Measurements at $\rho = 5 \times 10^{18} \text{ cm}^{-3}$ reported in this work are denoted by filled squares \blacksquare . Empty squares \square and circles \circ correspond to measurements at $\rho = 6 \times 10^{20} \text{ cm}^{-3}$ and $\rho = 2 \times 10^{21} \text{ cm}^{-3}$ reported in [18], empty triangles \triangle to measurements at $\rho = 1 \times 10^{21} \text{ cm}^{-3}$ reported in [43]

Chapter 6

Discussions

This work contributes to the study of the $\bar{p}\text{He}^+$ atom's formation process. Given the currently favored theoretical models, quenching mechanisms of some sort are required to explain experimental observations. This includes the absence of populations in the $n \geq 41$ region of the $\bar{p}\text{He}^+$ atom. Collisional quenching is a promising idea that could explain the difference between theoretical calculations and experimental findings in this regard.

We have studied potential collisional quenching effects on $\bar{p}\text{He}^+$ atoms after they have reached thermal equilibrium within a cryogenic helium target, i.e. when they are "cold". For this we carried out systematic population evolution measurements of $\bar{p}\text{He}^+$ atoms in four states at the lowest target densities studied so far ($\rho_L = 5 \times 10^{18} \text{ cm}^{-3}$). The population evolutions were fitted with cascade models such that the associated cascade lifetimes and relative capture probabilities could be obtained. We then compared the low density results to those from previous high density measurement and theoretical values.

The experiments were carried out at the CERN AD facility which provided pulsed antiproton beams of kinetic energy $E_{kin} = 5.3 \text{ MeV}$. The cooled antiprotons were further decelerated in the ASACUSA RFQD to 75 keV and allowed to come to rest in a low density helium target that was operated at pressure $p = 1.1 \text{ mbar}$ and temperature $T = 1.5 \text{ K}$. The $\bar{p}\text{He}^+$ atoms were studied in laser spectroscopy experiments using an injection seeded pulsed Ti:Sa laser system. Transitions beyond the tuning range of Ti:Sa were accessed using a wavelength shifting H_2 Raman cell with seven transits at 6.6 bar pressure. The annihilation products were detected using Cerenkov counters that were read out using gated fine mesh photomultiplier tubes.

None of the measured population evolutions at low density deviated significantly from the respective high density measurements. The extracted cascade lifetimes as well as the relative capture probabilities were identical within the experimental uncertainty which indicates a similar overall population distribution among quantum numbers (n, ℓ) irrespective of the applied density. The comparison of these results to the theoretically expected lifetimes indicated how only a negligible number of $\bar{\text{pHe}}^+$ atoms occupies states in the very high $n \geq 41$ region at low and high densities.

Our results can constrain hypothesized collisional effects that could potentially settle the disagreement between experiment and theory, i.e. the efficient quenching of thermal $\bar{\text{pHe}}^+$ atoms within the studied density range $10^{18} - 10^{20} \text{ cm}^{-3}$ is excluded.

Theoretical models have formulated in detail how hot $\bar{\text{pHe}}^+$ collisional quenching could explain the depletion of very high $n \geq 41$ states but remain consistent with the experimentally observed population peak around $n \sim 38$. Two of these models were presented in this work: Sauge et. al argued that due to their lower activation barrier $\bar{\text{pHe}}^+$ atoms in higher n states are particularly prone towards annihilations when collisions occur on the $\sim \text{eV}$ scale. Korenman on the other hand showed that even under the premise of an only slightly n sensitive quenching cross section, higher n states will be more efficiently depleted since they are initially formed with larger recoil momenta. Experimental access to probe hot $\bar{\text{pHe}}^+$ collisional quenching is therefore crucial but remains difficult. Helium targets of density $\rho \geq 10^{18} \text{ cm}^{-3}$ are required to stop antiproton beams of energy $E_{kin} \approx 75 \text{ keV}$ within experimentally reasonable length scales $\sim \text{cm}$. In these media however hot $\bar{\text{pHe}}^+$ collisional quenching is limited to a timescale of $\lesssim 100 \text{ ps}$ which is too short to be experimentally resolved. A dedicated study must therefore utilize helium targets operated at extremely low densities in order to study the very first collisions which are critical in this regard. Concurrently this means that the corresponding antiproton beam must be of low enough energy such that it will be stopped within the low density helium medium such that $\bar{\text{pHe}}^+$ atoms can be formed.

Chapter 7

Outlook

At CERN the next antiproton storage ring ELENA (Extremely Low Energy Antiproton) is under construction and will presumably be operational by 2020. It will provide electron cooled antiproton beams at 100 keV kinetic energy. These beams can be further decelerated down to the 1 – 10 eV range. Using new targets operating at even lower densities, very low energy antiproton beams might then be used to perform laser spectroscopy experiments on $\bar{p}\text{He}^+$ atoms after a few collision only and thus well before the completion of thermalization. In this way a better control of the collision kinematics might be obtained such that the contribution of hot $\bar{p}\text{He}^+$ collisional quenching can be determined. Possible populations in states with very large $n \geq 41$ will be of particular interest in this regard as these might be probed before the respective atoms are predicted to be destroyed. The corresponding transitions are predominantly in the near IR which is why the constructed mutli-pass Raman cell will be of use as it enables the generation of pulsed laser beams with the available laser system in that wavelength range.

In the short term future the Raman cell might be used with the current target and accelerator setup to detect even small populations of $\bar{p}\text{He}^+$ atoms in unprobed states with $n \geq 41$. A potential candidate transition for this physics objective is $(41, 36) \rightarrow (42, 35)$ at wavelength $\lambda = 1326$ nm which would represent the first direct probe of a state with $n \geq 41$. Due to the wavelength dependence of the SRS process it might be necessary to operate the Raman cell in its upgraded mode with 11 instead of 7 transits.

Furthermore the Raman cell can be utilized to measure new IR transitions in the high n region of the related $\bar{p}^3\text{He}^+$ atom. Suitable candidate transitions here

are $(39,34)\rightarrow(40,33)$ at $\lambda = 1127$ nm and $(39,35)\rightarrow(40,34)$ at $\lambda = 1168$ nm. The knowledge of the respective parent state populations could provide a better understanding of this atom's formation process.

Appendix A

Formation models

In the following we briefly outline a selection of the most well established theoretical models regarding the capture of negatively charged heavy particles (such as μ, κ, \bar{p}) by atoms in particular helium.

A.1 Fermi Teller model (FTM)

The Fermi Teller model was the first model to quantitatively discuss atomic capture cross sections [96]. Here the atomic electrons are treated as a degenerate fermion gas lying in an average potential created by the nucleus. It is obvious that this approximation makes the FTM most suitable for atoms of large Z . An antiproton propagating through said fermion gas continuously loses energy via coulomb interaction and is finally captured when its energy becomes negative.

The most well known result of the Fermi Teller model is the Z scaling according to which σ_{capt} is nearly proportional to Z . The precise dependence though can be varied within certain sub-models. Today most commonly a modified power law is used such that [97]:

$$\sigma_{\text{capt}} = \begin{cases} \propto Z^{2/3} & \text{for all } E < I_0 \\ 0 & \text{else} \end{cases}$$

Nevertheless the FTM cannot provide anything beyond a rough estimate of σ_{capt} as it does not take account of the atomic shell structure.

A.2 Classical trajectory Monte Carlo calculation (CTMC)

The CTMC approach firstly presented in [98] is radical in the sense that it assigns classical dynamics to all involved particles. Furthermore the initial atomic coordinates are assumed to be constituted by a classical microcanonical distribution. Beyond these no further approximations are made. The calculations are exact and the statistical errors can be reduced by increasing the number of computed trajectories. Among the advantages of the CTMC is the consistent treatment of excitation, ionization and capture as well as its validity over a relatively wide energy range.

The CTMC consists of the following three steps: (i) Monte Carlo sampling of the initial positions and momenta assuming a microcanonical distribution (ii) integration of the classical Hamiltonians (iii) identification of the final states in the asymptotic limit. Steps (i)-(iii) are iterated until a sufficiently large sample size is obtained. For the process of interest "k" the cross section is given by

$$\sigma_k = \frac{N_k}{N_{tot}} \pi b_{max} \quad (\text{A.1})$$

where N_k is the number of k-type events, N_{tot} is the total number of trajectories and b_{max} is the maximal impact parameter to which it had been integrated. It is worthy to note that b_{max} does not need to be known in advance, since the integration is done in samples. The CTMC corroborates main features of other models and is particularly reliable in the treatment of intermediate velocities $v_{\bar{p}} \approx 1$ au. In principle multi-electron atoms can not be treated with the CTMC since they are classically unstable. However reasonable results have been obtained for helium in three body CTMC where the helium nucleus and one electron were combined to a He^+ ion [99].

A.3 Fermion molecular dynamics method (FMD)

The FMD is a quasi-classical supplement to the CMTC [100]. The classical Hamiltonian is modified by adding suitable pseudo-potentials V_P and V_H in order to satisfy the Pauli exclusion and Heisenberg uncertainty principle. The Hamiltonian of the FMD is given;

$$H_{\text{FMD}} = H_0 + V_P + V_H \quad (\text{A.2})$$

where H_0 is the conventional classical Hamiltonian containing the free particle kinetic energies and their particle pair Coulomb potentials. With the Hamiltonian obtained in

this way, one proceeds in the very same steps as in the CMTC.

A.4 Adiabatic Ionization model (AI)

The AI is a semi-classical method in which the $\bar{p} + \alpha$ -nucleus system is regarded as a classical dipole at frozen internuclear distances R . In the resulting potential the electronic Schroedinger equation is solved under the Born-Oppenheimer approximation (BO).

Critical to the AI is the assumption that the antiproton motion is slow enough such that the electrons can adapt adiabatically towards the induced perturbation and thus remain in their instantaneous eigenstates. In the AI no distinction between projectile types is made but obviously this approximation works best in the limit $m_e/m_{\bar{p}} \rightarrow 0$. Electronic interaction with fixed dipoles now has the peculiar property of having either infinite or zero eigenstates, depending on the respective dipole strength. In fact there exists a critical internuclear distance R_c , below which the electron is no longer bound but escapes adiabatically i.e. with zero kinetic energy $T_e=0$. For given R the system's adiabatic potential energy can be written

$$V_a = \langle \psi_{ad}(r, R) | H | \psi_{ad}(r, R) \rangle \quad (\text{A.3})$$

where H is the sum of $\bar{p} + \text{nucleus}$ potential and the free atom Hamiltonian H_{He}

$$H = -\frac{e^2}{R} + H_{\text{He}}$$

and $\psi_a(r, R)$ the adiabatic wave function. In Fig. A.4.1 the potential energy curves for hydrogen are shown. It can be seen that the curves for the $\bar{p} + \text{H}$ and $\bar{p} + \text{H}^+$ systems merge at $R_c=0.639a_0$. It is important to note though that the naive AI model is not applicable to helium since there is no R for which the corresponding potential energy curves meet.

A.5 Adiabatic hidden-crossing theory (AHC)

The Adiabatic hidden-crossings theory is an extension of the AI that has successfully provided ionization cross-section for ion-atom collisions [101]. Here the electronic wave functions are continued along a complex path of the internuclear distance R . The resulting electronic energy surfaces $\epsilon(R)$ have a complicated structure, in particular

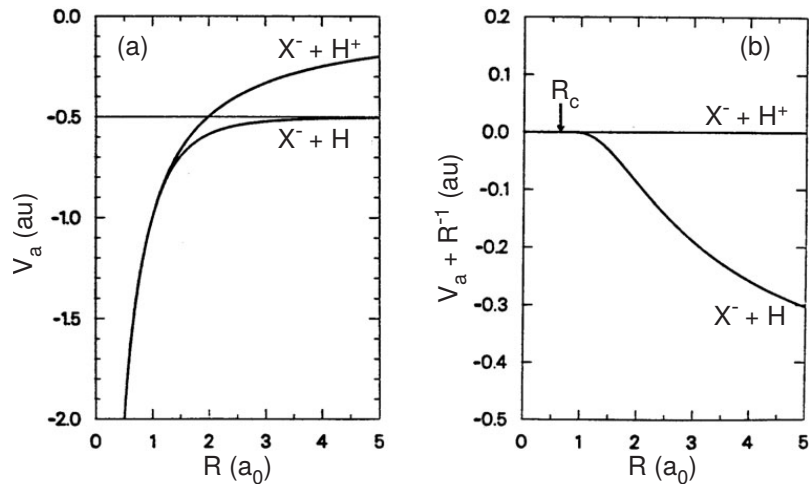


Figure A.4.1: a) Potential energy curve V_a for $X^- + H$ and $X^- + H^+$. X^- can be any sufficiently heavy negatively charged particle. For better illustration the Coulomb potential between the projectile and the α nucleus $V_{\alpha-\bar{p}} \propto \frac{1}{R}$ has been subtracted out in b). The two lines merge at $R_c = 0.639a_0$. Fig. from [41]

they comprise many branch points in the complex R plane. Furthermore it is found that if one were to start in a state on the real R -axis with wave function $\psi_\alpha(x, R)$ and energy $E_\alpha(R)$ and continued along a complex R -path that encircles a branch point P_b before returning to the real axis, one would not return to the same but to a different state with deviating wave function and $\psi_\beta(R)$ and energy $E_\beta(R)$. A behavior termed as hidden crossings. The inelastic collision problem thus reduces to the identification and integration around the relevant branch points. Briggs et. al. have applied the AHC to the capture of antiprotons by helium and found that the ionization is dominated only by the first few branch points [37].

A.6 Diabatic state model (DS)

It had been criticized that due to the accelerated motion of the negatively charged projectile towards the positive nucleus the adiabatic approximation is no longer justified at small R . The Diabatic model developed by Cohen et al. overcomes this limitation by explicitly considering non-adiabatic (diabatic) kinematics of the regarded electrons [102]. For this a non-adiabatic electronic wave function must show the effect of increasing polarization as the \bar{p} approaches. Polarization in the DS is allowed for by extending the basis of the electronic orbit wave functions by a single polarized configuration. The polarization of the said configuration is ensured in two ways (i) perturbing the isolated atom by a weak uniform electric field (ii) choosing an orbital of p-character

that minimizes the electron energy at some finite distance R_p . Analogously to Eq. A.3 diabatic potential energy is thus given by

$$V_d = \langle \psi_d(R) | H | \psi_d(R) \rangle \quad (\text{A.4})$$

where ψ_d is now the diabatic wave function and H is defined as in Eq. A.4. The diabatic potential energy V_d of the $\bar{p} + \text{He}$ crosses that of the $\bar{p} + \text{He}^+$ at $R_c = 0.96a_0$. At R below R_x the diabatic set of electron basis wave functions ψ_b^d is therefore embedded into an electronic continuum. Whereby a finite auto-ionization width is generated and can be obtained with Fermi's golden rule

$$\Gamma(R) = 2\pi\rho_e |\langle \mathfrak{A}\psi_d^+ \Phi_e | H - E_d | \psi_d \rangle|^2 \quad (\text{A.5})$$

where ρ_e is the density of electronic continuum states Φ_e per unit energy, \mathfrak{A} is the anti-symmetrization operator and ψ_d^+ is the wave function of the system with one electron removed. Difficulties typically lie in the accurate description of the continuum wave functions. Hazi suggested a method which employs the discretization of the continuum coupled with Steltjes moment theory and can be read here [103]. The combined local complex potential can finally be utilized in $\bar{p} + \text{He}$ collisions

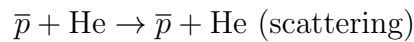
$$W_d(R) = V_d(R) - \frac{i}{2}\Gamma(R) \quad (\text{A.6})$$

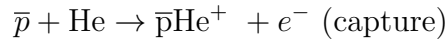
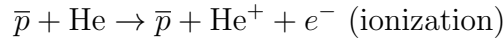
Unlike the AI the DS allows for finite kinetic energies of the ejected electron T_{e-} . Latter is defined by the potential energy difference between the initial atomic and final ionic state as well as the ionization potential and is thus a function of the distance R at which the auto-ionization occurs.

$$T_{e-}(R) = (V_d(R) - V_d^+(R)) + I_0 \quad (\text{A.7})$$

Concrete calculations reveal that the ejected electron's kinetic energy is very low compared to the ionization potential [41].

In [104] Korenman introduced the coupled channel semi-classical approximation (CCSA) that extends the diabatic state model in terms of quantum mechanical coupling between the three possible outgoing state:





the results obtained in this way are consistent with the related DS model.

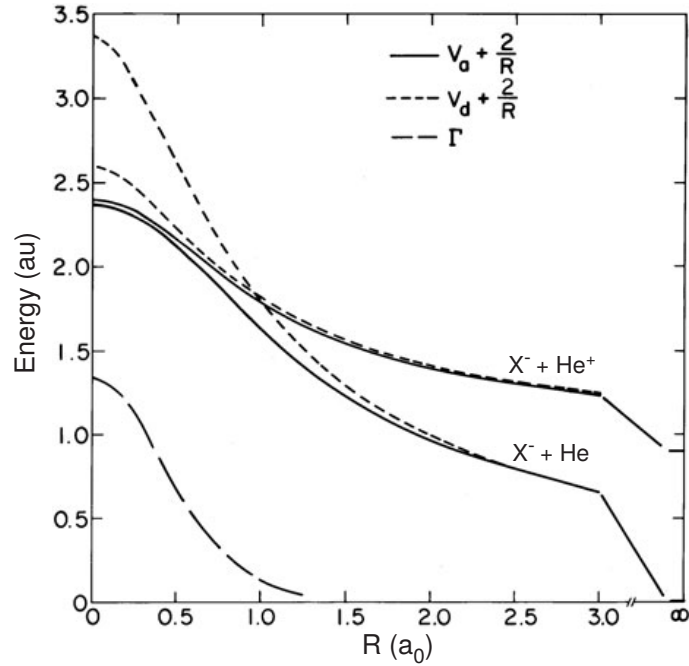


Figure A.6.1: Diabatic and adiabatic potential energy curves of the $\bar{p} + \text{He}$ and $\bar{p} + \text{He}^+$ system. The adiabatic curves do not cross which is why a simple adiabatic model cannot describe the capture process. Contrarily the diabatic potential curves cross at $R_c = 0.96a_0$. Additionally the diabatic auto-ionization width is shown. Figure from [41]

A.7 Time dependent scattering theory (TDST)

Recently Tong et. al. have provided a fully quantum mechanical ansatz based on time-dependant scattering theory [35] [105]. In the first step the system's four body configuration is reduced to a three body problem where one electron is frozen in the 1s orbital. The Lippmann-Schwinger equation of the resulting scattering problem can be written as

$$\psi = \phi \frac{1}{E - H_0 + i\epsilon} V_i \psi$$

where ψ is the solution to time-dependent overall Hamiltonian H , V_i the interaction potential and ϕ the solution to the initial state Hamiltonian H_0 . The Goldberger-Chew

formal solution

$$\psi = \phi \frac{1}{E - H + i\epsilon} V_i \phi$$

can be Fourier transformed to

$$\psi(r, R, t) = \phi(r, R, t) - i \int_{-\infty}^t e^{i(H-E)(t-t')} f(t') V_i \phi(r, R, t') dt'$$

where a correct choice of $f(t) = e^{-\epsilon|t|}$ with infinitesimally small ϵ adiabatically switches on V_i . The time integral in Eq:A.7 was directly performed using the partial wave expansion to which the details can be found in [106]. The time-dependent wave function can be used to obtain detailed information on collision system including the capture cross section and thus primordial population distribution.

Appendix B

Raman scattering

In this chapter we briefly review Raman scattering of optical fields. This is the inelastic scattering process through which the associated photon interacts with an atom or a molecule resulting in a shift of its frequency. Photons experiencing frequency down and up conversion are referred to as Stokes and anti-Stokes photons respectively. For simplicity we will only treat the Stokes photons in this chapter as all conclusions regarding the anti-Stokes follow analogously. We will further concentrate on gases as the Raman medium where the process is primarily due to a change in the corresponding molecular vibrational or rotational states.

When an optical beam emitted by a laser propagates through a Raman active gas, the generation probability of Stokes shifted photons P_S is not only determined by the number of available pump photons N_p and contributing molecules N_m but also by the number of the already present Stokes photons N_S

$$P_S = D_R N_p (N_S + 1) N_m \quad (\text{B.1})$$

where D_R is a yet to be defined proportional factor. This probability can be rewritten into a rate equation as a function of the laser propagation length z

$$\frac{dn_S}{dz} = \frac{n}{c} D N_p (N_S + 1) N_0 \quad (\text{B.2})$$

For an intuitive comprehension it is reasonable to investigate this rate equation for two distinguished scenarios

1. Spontaneous Raman scattering (RS): $N_S \ll 1$

$$N_S(z) = \frac{n}{c} D N_p N_0 z \quad (\text{B.3})$$

When no initial Stokes field is present we speak of spontaneous Raman scattering. Here the number of Stokes photons grows linearly as the laser beam propagates

2. Stimulated Raman scattering (SRS): $N_s \gg 1$

$$N_S(z) = N_S(0)e^{Gz} \quad (\text{B.4})$$

with gain coefficient

$$G = \frac{n}{c} D N_p N_0 \quad (\text{B.5})$$

Stimulated Raman scattering requires a finite initial Stokes field but grows exponentially in magnitude.

It is important to note that this simplistic approach only represents a rough estimate as it e.g. does not consider the geometry of the laser beam or pump depletion effects. Nevertheless, the different scalings of the two processes are seen which experimentally result in conversion efficiencies that differ by many orders of magnitude: $\epsilon_{SR} \sim 10^{-6}$ compared $\epsilon_{SRS} \sim 10^{-1}$.

In this work we treat each of the two processes in a classical picture which captures all aspects that are relevant for the purpose of this work. Semi- and fully quantum mechanical descriptions have been provided e.g. by Cheng and others [107]. We start however with a quick recap the polarizability which is a prerequisite for the Raman process upon molecules.

B.1 Induced polarization

Oscillating electromagnetic fields relevant to this work are exclusively in the visible and infra red range with corresponding frequencies of order ~ 300 THz. This value is too high for heavy nuclei to follow such that the primary source for the Raman effect are the electronic motions. The adiabatic electronic potentials however depend concurrently on the nuclear coordinates i.e. the presence of vibrational and rotational nuclear modes perturbs the electronic polarizability.

In this treatment we begin with the polarization P which can macroscopically be given by the sum of all electric dipole moments. For N dipoles of strengths μ one thus obtains

$$P(t) = N\mu(t) \quad (\text{B.6})$$

the Raman effect relies on dipole moments which can be induced by external electric fields $E(t)$.

$$\mu(t) = \alpha E(t) \quad (\text{B.7})$$

where α is the polarizability of the corresponding molecule. In the presence of nuclear modes one can expand α in terms of the nuclear coordinate Q

$$\alpha(t) = \alpha_0 + \left(\frac{\partial \alpha}{\partial Q_0} \right) Q + \dots \quad (\text{B.8})$$

At this point we will further assume that to first order the nuclear motion in Q can be represented by that of a classical harmonic oscillator

$$Q(t) = Q_0 (e^{i\omega_m t + i\phi} + e^{-i\omega_m t - i\phi}) + c.c. \quad (\text{B.9})$$

where ω_m is the nuclear resonance frequency and Q_0 and ϕ the amplitude and phase offset of the nuclear motion. Combining Eq. B.7, B.8 and B.9 while assuming an incoming electric field of type

$$E = E_0 e^{-i\omega_i t} a + c.c. \quad (\text{B.10})$$

we obtain for the resulting induced dipole moment

$$\mu(t) = \alpha_0 E_0 e^{-i\omega_i t} + E_0 \frac{\partial \alpha}{\partial Q_0} Q_0 (e^{-i\omega_S t + i\phi} + e^{-i\omega_{AS} t - i\phi}) + \dots \quad (\text{B.11})$$

which can be inserted in Eq. B.6 for the correspondingly induced polarization. The first term on the right side of the equation is identified with the elastic Rayleigh scattering process while the second is the associated Raman term. Due to its inelastic nature the Raman term shifts the incident field at ω_i to the Stokes frequency $\omega_S = \omega_i - \omega_m$ and the anti-Stokes frequency $\omega_{AS} = \omega_i + \omega_m$. It is further important to note that the Raman term is proportional in $\partial\alpha/\partial Q_0$ and thus dependent on the polarizability change along the nuclear mode Q . This polarizability change is highly dependent on the symmetry of the regarded molecule.

B.2 Spontaneous Raman scattering

In spontaneous Raman scattering we are interested in the field that is emitted at frequency ω_S by a molecule which is under the influence of an incident field at ω_i . Within a classical model the regarded molecule can be treated as a dressed dipole with

dipole moment μ . The amplitude of the electric far field emitted into the mode ω_S by such a dipole is obtained from classical electro dynamics

$$E(\omega_S) = \hat{\theta} |\mu(\omega_S)| \frac{\omega_S^2 e^{ikr}}{4\pi r \epsilon c^2} \sin(\theta) \quad (\text{B.12})$$

while direct integration over the unit sphere provides the correspondingly emitted power into ω_S

$$I(\omega_S) = \int d\Omega \frac{\epsilon_0 c}{2} |E(\omega_S)|^2 \quad (\text{B.13})$$

where we can insert the respective term of the dipole moment as follows from Eq. B.11

$$I(\omega_S) = \frac{\omega_S^4}{12\pi\epsilon_0 c^3} Q_0^2 |E_0|^2 \left| \frac{\partial \alpha}{\partial Q} \right|^2 \quad (\text{B.14})$$

It is common to rewrite the emitted Stokes intensity under usage of an effective cross section term $\sigma(\omega_S)$ which provides a handy expression analogous to Beer-Lambert law.

$$I(\omega_S) = Nd\sigma(\omega_S)I_0 \quad (\text{B.15})$$

Spontaneously Raman scattered light is incoherent as the phase of the Stokes field depends on the phase of the regarded molecular vibration which is generally uncorrelated for individual molecules.

B.3 Stimulated Raman scattering

Stimulated Raman scattering (SRS) can be intuitively understood in the following way: A pump field E_p of frequency ω_p interacts with a molecule with vibrational or rotational frequency ω_m and thus generates a stokes field E_s oscillating at $\omega_S = \omega_p - \omega_m$ via spontaneous Raman scattering. The stokes field now beats with the pump field producing the modulated intensity field

$$I(t) = I_0 + I_1 \cos((\omega_p - \omega_S)t) \quad (\text{B.16})$$

The associated field $E(z, t)$ coherently drives the molecular vibration at frequency ω_m which in turn leads to stronger molecular vibrations reinforcing the stokes field

$$E(z, t) = (E_p e^{i(k_p z + \omega_p t)} + E_s e^{i(k_s z + \omega_s t)} + c.c.) \quad (\text{B.17})$$

If the polarizability $(\partial\alpha/\partial Q)_0$ and thus the induced dipole moment μ is finite, then this introduces a non-zero coupling between the electronic motions and the nuclear mode such that the combined field exerts a force on the vibrational oscillator of form

$$F(z, t) = \left(\frac{\partial\alpha}{\partial Q} \right)_0 [E_s E_p^* e^{-i(Kz - \Omega t)} + c.c.] \quad (\text{B.18})$$

where we have used $\Omega = \omega_p - \omega_s$ and $K = k_p - k_s$. This expression can be used to formulate the corresponding equation of motion as suggested by [108]

$$\frac{\partial^2 Q}{\partial t^2} + 2\gamma \frac{\partial Q}{\partial t} + Q\omega_m^2 = \frac{F(z, t)}{m} \quad (\text{B.19})$$

which can be solved with the ansatz

$$Q(t) = Q_0(\Delta\omega) e^{-i(Kz - \Omega t)} + c.c. \quad (\text{B.20})$$

and the frequency dependent amplitude

$$Q_0(\Delta\omega) = \left(\frac{\partial\alpha}{\partial Q} \right)_0 \frac{E_p E_s^*}{\omega_m^2 - (\Delta\omega)^2 + 2i\gamma\Delta\omega} \quad (\text{B.21})$$

If we now insert Eq. B.20 into Eq. B.6 B.7 and B.8 we obtain for the polarization

$$P(z, t) = N \left[\alpha_0(z, t) + \left(\frac{\partial\alpha}{\partial Q} \right)_0 \right] (E_p(z, t) + E_s(z, t)) \quad (\text{B.22})$$

This result can be compared to a power expansion in $E(t)$ of the induced polarization

$$P(t) = \epsilon_0(\chi^{(1)} E(t) + \chi^{(2)} E(t)^2 + \chi^{(3)} E(t)^3 + \dots) \quad (\text{B.23})$$

where it is seen that the terms proportional α_0 are associated with the linear polarization term while the other terms are associated with the third order polarization. We can decompose latter according to respective oscillations frequencies

$$P_3 = P(2\omega_p - \omega_s) e^{-i(2\omega_p - \omega_s)t} + P(\omega_s) e^{-i\omega_s t} + P(\omega_p) e^{-i\omega_p t} + P(2\omega_s - \omega_p) e^{-i(2\omega_s - \omega_p)t} + c.c. \quad (\text{B.24})$$

Relevant for stimulated Raman scattering is only the term oscillating at the Stokes frequency ω_s and can be expressed

$$P(\omega_s) = \frac{N}{m} \left(\frac{\partial\alpha}{\partial Q} \right)_0^2 \frac{|E_p|^2 E_s}{\omega_m^2 - (\Omega)^S + 2i\gamma\Omega} \quad (\text{B.25})$$

This commonly rewritten into

$$P(\omega_2) = 6\epsilon_0\chi_R(\Omega)|E_p|^2E_s^* \quad (\text{B.26})$$

with the associated Raman susceptibility defined as

$$\chi_R = \frac{N}{6m\epsilon_0} \left(\frac{\partial\alpha}{\partial Q} \right)_0^2 \frac{1}{\omega_m^2 - (\Omega)^2 - 2i\gamma\Omega} \quad (\text{B.27})$$

It can be seen that at resonance the Raman susceptibility is purely imaginary and negative, implying a negative nonlinear absorption or in other words a gain of the Stokes field. These results can be inserted into the one-dimensional wave equation including a polarization as source such that it one finally finds

$$\frac{\partial^s E_s(z, t)}{\partial z^2} + \frac{\omega_s^2}{c^2} = -\mu_0\omega_s^2 P(\omega_s) \quad (\text{B.28})$$

If we now introduce the Raman gain G as in Eq. 3.6

$$G = \frac{3i\omega_s}{2n_s n_p \epsilon_0 c} \chi_R \quad (\text{B.29})$$

we obtain the wave equation for the stokes field consistent with Eq. 3.5

$$\left(\frac{1}{k_p} \nabla_T^2 + i \frac{\partial}{\partial z} \right) E_p = \frac{i\epsilon_0}{2} c n^2 G |E_p|^2 E_s \quad (\text{B.30})$$

List of Acronyms

Acronym	Explanation
AD	<i>Antiproton Decelerator</i> . 188 m circumference particle decelerator that decelerates and cools antiprotons.
ADC	<i>Analog to Digital Converter</i> Electronic device that converts a physical quantity e.g. voltage to a digital number.
BBO	<i>Beta Barium Borate</i> . Bifringent crystal used for second harmonic generation.
BPM	<i>Beam Profile Monitor</i> XY-grid of photocathode wires that non-destructively measures the spatial profile of pulsed UV, X-ray or charged particles beam via secondary electron emission.
c.c.	<i>Complex Conjugate</i> Number with identical real part and imaginary part that is equal in magnitude but opposite in sign.
DATS	<i>Delayed Annihilation Time Spectrum</i> Annihilation count rate of antiprotons coming to rest in helium as a function of time. Comprises to distinct features: a sharp prompt and a long tail.
CERN	<i>European Organization for nuclear research</i> European Research organization that operates the world's largest acclerator complex including the large hadron collider and the antiproton decelerator.
CODATA	<i>Committee on Data for Science and Technology</i> Interdisciplinary work group of the International Council of Science promoting improved data management. Provides globally accepted values of fundamental constants in a least-square-adjustment every four years
CW	<i>Continous Wave</i> Electromagnetic wave of constant amplitude and frequency. In the context of lasers used oposed to pulsed mode.
FP	<i>Fabry-Perot</i> Optical cavity made of two reflecting surfaces providing equidistant frequency markers.
HV	<i>High Voltage</i>
HFS	<i>Hyperfine Structure</i> Energy level splitting due to the coupling \bar{p} angular momentum and spin with the electron spin.

continued on next page

continued from previous page

Acronym	Explanation
Linac	<i>Linear Accelerator.</i> Particle accelerator in linear design typically using radio frequency cavities.
Nd:Yag	<i>Neodymium-doped Yttrium Aluminium Garnet</i> $Nd:Y_3Al_5O_{12}$ Crystal used as lasing medium for solid state lasers, particularly for high power and Q-switched applications at 1064 nm.
Nd:YVO	<i>Neodymium-doped Yttrium Orthovanadate</i> $Nd:YVO_4$ Similar to Nd:YAG but with lower upper state lifetime and higher gain absorptions which make it better suited for cw applications.
$\bar{p}He^+$	<i>Antiprotonic Helium.</i> Three body system consisting of a helium nucleus α , an electron in the 1s state e^- and an antiproton \bar{p} in a high lying Rydberg state.
PMT	<i>Photomultiplier Tube.</i> UV, x-ray or charged particle detector, employing amplification via secondary electron generation in a vacuum tube.
PS	<i>Proton Synchrotron.</i> 628 m circumference particle accelerator at CERN, accelerates protons from 1.4 GeV to 28 GeV in nominal mode.
ptt	<i>Peak To Total.</i> Measure of the population transfer from a meta-stable to an Auger unstable state in $\bar{p}He^+$ laser spectroscopy. Defined as the area below the forced annihilation peak in the DATS divided annihilation aggregate.
RS	<i>Raman Scattering</i> inelastic scattering of a photon upon a molecule or phonon.
SRS	<i>Stimulated Raman Scattering</i> Raman scattering under the influence of a seed field, leading to a strong enhancement. The seed field can either be provided by spontaneously Raman scattered photons or deliberately injected.
Ti:Sa	<i>Titanium Sapphire</i> $Ti:Al_2O_3$. Sapphire crystal doped with titanium ions, often used as lasing medium because of its large tunable range between 600 nm and 1100 nm.

Bibliography

- [1] T. H. Fields, G. B. Yodh, M. Derrick, and J. G. Fetkovich, “Cascade time of π^- in liquid hydrogen,” *Phys. Rev. Lett.*, vol. 5, pp. 69–70, Jul 1960.
- [2] J. H. Doede, R. H. Hildebrand, M. H. Israel, and M. R. Pyka, “Moderation and absorption times of negative pions in liquid hydrogen,” *Phys. Rev.*, vol. 129, pp. 2808–2811, Mar 1963.
- [3] J. G. Fetkovich and E. G. Pewitt, “Experimental study of the cascade time of negative mesons in a liquid helium bubble chamber,” *Phys. Rev. Lett.*, vol. 11, pp. 290–293, Sep 1963.
- [4] M. M. Block, T. Kikuchi, D. Koetke, J. Kopelman, C. R. Sun, R. Walker, G. Culligan, V. L. Telegdi, and R. Winston, “Moderation time for nuclear capture of negative pions in liquid he^4 ,” *Phys. Rev. Lett.*, vol. 11, pp. 301–303, Sep 1963.
- [5] K. A. O. et al., “Review of particle physics,” *Chin. Phys.*, vol. C38, p. 090001, 2014.
- [6] G. T. Condo, “On the absorption of negative pions by liquid helium,” *Physics Letters*, vol. 9, no. 1, pp. 65–66, 1964.
- [7] J. E. Russell, “Metastable states of $\alpha\pi^-e^-$, αK^-e^- , and $\alpha\bar{p}e^-$ atoms,” *Phys. Rev. Lett.*, vol. 23, pp. 63–64, Jul 1969.
- [8] J. E. Russell, “Interactions of an αK^-e^- atom with a he atom,” *Phys. Rev.*, vol. 188, pp. 187–197, Dec 1969.
- [9] J. E. Russell, “Structure of neutral mesonic atoms formed in liquid helium,” *Phys. Rev. A*, vol. 1, pp. 721–734, Mar 1970.
- [10] J. E. Russell, “Auger rates for circular orbits of $\alpha\pi^-e^-$, αK^-e^- , and $\alpha\bar{p}e^-$ atoms,” *Phys. Rev. A*, vol. 1, pp. 742–750, Mar 1970.

- [11] J. E. Russell, "Distortion of the electron wave function in $\alpha\pi^-e^-$, αK^-e^- , and $\alpha\bar{p}e^-$ atoms," *Phys. Rev. A*, vol. 1, pp. 735–742, Mar 1970.
- [12] T. Yamazaki, M. Aoki, M. Iwasaki, R. S. Hayano, T. Ishikawa, H. Outa, E. Takada, H. Tamura, and A. Sakaguchi, "Trapping of negative kaons by metastable states during the atomic cascade in liquid helium," *Phys. Rev. Lett.*, vol. 63, pp. 1590–1592, Oct 1989.
- [13] S. N. Nakamura, M. Iwasaki, H. Outa, R. S. Hayano, Y. Watanabe, T. Nagae, T. Yamazaki, H. Tada, T. Numao, Y. Kuno, and R. Kadono, "Negative-pion trapping by a metastable state in liquid helium," *Phys. Rev. A*, vol. 45, pp. 6202–6208, May 1992.
- [14] M. Iwasaki, S. N. Nakamura, K. Shigaki, Y. Shimizu, H. Tamura, T. Ishikawa, R. S. Hayano, E. Takada, E. Widmann, H. Outa, M. Aoki, P. Kitching, and T. Yamazaki, "Discovery of antiproton trapping by long-lived metastable states in liquid helium," *Phys. Rev. Lett.*, vol. 67, pp. 1246–1249, Sep 1991.
- [15] N. Morita, M. Kumakura, T. Yamazaki, E. Widmann, H. Masuda, I. Sugai, R. S. Hayano, F. E. Maas, H. A. Torii, F. J. Hartmann, H. Daniel, T. von Egidy, B. Ketzer, W. Müller, W. Schmid, D. Horváth, and J. Eades, "First observation of laser-induced resonant annihilation in metastable antiprotonic helium atoms," *Phys. Rev. Lett.*, vol. 72, pp. 1180–1183, Feb 1994.
- [16] M. Hori, A. Sótér, D. Barna, A. Dax, R. S. Hayano, S. Friedreich, B. Juhász, T. Pask, E. Widmann, D. Hórvath, L. Venturell, and N. Zurlo, "Two-photon laser spectroscopy of antiprotonic helium and the antiproton-to-electron mass ratio," *Nature*, vol. 475, pp. 484–488, Jul 2011. 10.1038/nature10260.
- [17] M. Hori and V. I. Korobov, "Calculation of transition probabilities and ac stark shifts in two-photon laser transitions of antiprotonic helium," *Phys. Rev. A*, vol. 81, p. 062508, Jun 2010.
- [18] M. Hori, J. Eades, R. S. Hayano, T. Ishikawa, J. Sakaguchi, T. Tasaki, E. Widmann, H. Yamaguchi, H. A. Torii, B. Juhász, D. Horváth, and T. Yamazaki, "Primary populations of metastable antiprotonic ^4He and ^3He atoms," *Phys. Rev. Lett.*, vol. 89, p. 093401, Aug 2002.
- [19] T. Yamazaki, N. Morita, R. S. Hayano, E. Widmann, and J. Eades, "Antiprotonic helium," *Physics Reports*, vol. 366, no. 4 - 5, pp. 183–329, 2002.

- [20] R. S. Hayano, M. Hori, D. Horvath, and E. Widmann, “Antiprotonic helium and cpt invariance,” *Reports on Progress in Physics*, vol. 70, no. 12, p. 1995, 2007.
- [21] T. B. Day, “K-meson capture by helium,” *Il Nuovo Cimento*, vol. 18, no. 2, pp. 381–394, 1960.
- [22] K. . Ohtsuki, “unpublished theoretical data.” unpublished, 1992.
- [23] T. Yamazaki and K. Ohtsuki, “Atomic core-polarization effects in metastable hadronic helium atoms,” *Phys. Rev. A*, vol. 45, pp. 7782–7786, Jun 1992.
- [24] N. Morita, K. Ohtsuki, and T. Yamazaki, “Laser spectroscopy of metastable antiprotonic helium atomcules,” *Nuclear Instruments and Methods in Physics Research Section A: Accelerators, Spectrometers, Detectors and Associated Equipment*, vol. 330, no. 3, pp. 439–446, 1993.
- [25] H. Yamaguchi, T. Ishikawa, J. Sakaguchi, E. Widmann, J. Eades, R. S. Hayano, M. Hori, H. A. Torii, B. Juhász, D. Horváth, and T. Yamazaki, “Anomalies in the decay rates of antiprotonic helium-atom states,” *Phys. Rev. A*, vol. 66, p. 022504, Aug 2002.
- [26] M. Hori, “Collisional dynamics in antiprotonic helium,” *Nuclear Instruments and Methods in Physics Research Section B: Beam Interactions with Materials and Atoms*, vol. 267, no. 2, pp. 343–346, 2009.
- [27] I. Shimamura, “Moleculelike metastable states of antiprotonic and mesic helium,” *Phys. Rev. A*, vol. 46, pp. 3776–3788, Oct 1992.
- [28] Y. Kino, M. Kamimura, and H. Kudo, “Numerical accuracy of the energy levels of antiprotonic helium atoms,” *Nuclear Instruments and Methods in Physics Research Section B: Beam Interactions with Materials and Atoms*, vol. 214, pp. 84 – 88, 2004. Low Energy Antiproton Physics (LEAP’03).
- [29] V. I. Korobov and I. Shimamura, “Auger transition rates for metastable states of antiprotonic helium $\text{he}^+\bar{p}$,” *Phys. Rev. A*, vol. 56, pp. 4587–4594, Dec 1997.
- [30] V. I. Korobov, “Metastable states in the antiprotonic helium atom decaying via auger transitions,” *Phys. Rev. A*, vol. 67, p. 062501, Jun 2003.
- [31] T. Kobayashi, *Study of highly excited states of antiprotonic helium atoms*. PhD thesis, University of Tokyo, 2013.

- [32] N. A. Cherepkov and L. V. Chernysheva, "Capture of μ -mesons by he atoms," *Yadernaya Fizika*, vol. 32, no. 709, 1980.
- [33] M. Leon, "Energy spectrum of stopping negative mesons and the concentration dependence of capture fractions," *Phys. Rev. A*, vol. 17, pp. 2112–2115, Jun 1978.
- [34] H. Daniel, "Formation of mesonic atoms in condensed matter," *Phys. Rev. Lett.*, vol. 35, pp. 1649–1651, Dec 1975.
- [35] X. M. Tong, K. Hino, and N. Toshima, "Anomalous bumpy structures in the capture cross sections of antiprotons by helium," *Phys. Rev. Lett.*, vol. 101, p. 163201, Oct 2008.
- [36] J. S. Cohen, "Multielectron effects in capture of antiprotons and muons by helium and neon," *Phys. Rev. A*, vol. 62, p. 022512, Jul 2000.
- [37] J. S. Briggs, P. T. Greenland, and E. A. Solov'ev, "The capture of slow antiprotons in noble gases," *Journal of Physics B: Atomic, Molecular and Optical Physics*, vol. 32, no. 2, p. 197, 1999.
- [38] V. K. Dolinov, G. Y. Korenman, I. V. Moskalenko, and V. P. Popov, "Atomic capture of negative muons and hadrons in helium," *Muon Catal. Fusion*, vol. 4, p. 169, 1989.
- [39] J. S. Cohen, R. L. Martin, and W. R. Wadt, "Diabatic-state treatment of negative-meson moderation and capture. ii. mixtures of hydrogen and helium," *Phys. Rev. A*, vol. 27, pp. 1821–1830, Apr 1983.
- [40] G. Y. Korenman and S. I. Rogovaya, "Formation of mesonic atoms in mixtures of the lightest elements," *Radiation Effects*, vol. 46, no. 3, pp. 189–198, 1980.
- [41] J. S. Cohen, "Capture of negative exotic particles by atoms, ions and molecules," *Reports on Progress in Physics*, vol. 67, no. 10, p. 1769, 2004.
- [42] M. Hori, J. Eades, E. Widmann, T. Yamazaki, R. S. Hayano, T. Ishikawa, H. A. Torii, T. von Egidy, F. J. Hartmann, B. Ketzer, B. C. Maierl, R. Pohl, M. Kumakura, N. Morita, D. Horváth, and I. Sugai, "Populations and lifetimes in the $v = n - \ell - 1 = 2$ and 3 metastable cascades of $\bar{p}\text{He}^+$ measured by pulsed and continuous antiproton beams," *Phys. Rev. A*, vol. 70, p. 012504, Jul 2004.
- [43] T. Kobayashi, D. Barna, R. S. Hayano, Y. Murakami, K. Todoroki, H. Yamada, A. Dax, L. Venturelli, N. Zurlo, D. Horvath, H. Aghai-Khozani, A. Soter, and

- M. Hori, "Observation of the 1154.9Å nm transition of antiprotonic helium," *Journal of Physics B: Atomic, Molecular and Optical Physics*, vol. 46, no. 24, p. 245004, 2013.
- [44] G. Y. Korenman, "Elastic scattering, ionisation and atomic capture in slow antiproton-atomic collisions," *Nuclear Physics A*, vol. 692, no. 1-2, pp. 145–152, 2001. Sixth Biennial Conference on Low-Energy Antiproton Physics.
- [45] G. Y. Korenman, "Collisional quenching of $\bar{\text{p}}\text{He}^+$ metastable states," *Hyperfine Interactions*, vol. 101-102, no. 1, pp. 463–469, 1996.
- [46] S. Sauge and P. Valiron, "Collisional survival of antiprotonic helium atoms," *Chemical Physics*, vol. 265, no. 1, pp. 47–61, 2001.
- [47] G. Y. Korenman, "Collisional processes in exotic atoms," *Hyperfine Interactions*, vol. 209, no. 1-3, pp. 15–20, 2012.
- [48] G. Y. Korenman, "Mechanisms and kinetics of exotic atom formation in hydrogen and helium," *Hyperfine Interactions*, vol. 101-102, no. 1, pp. 81–89, 1996.
- [49] G. Bonomi, "Long living states in antiprotonic helium at low densities," *Nuclear Physics A*, vol. 692, no. 1-2, pp. 137–144, 2001. Sixth Biennial Conference on Low-Energy Antiproton Physics.
- [50] M. Hori, H. A. Torii, R. S. Hayano, T. Ishikawa, F. E. Maas, H. Tamura, B. Ketzer, F. J. Hartmann, R. Pohl, C. Maierl, M. Hasinoff, T. von Egidy, T. M. Kumakura, N. Morita, I. Sugai, D. Horváth, E. Widmann, J. Eades, and T. Yamazaki, "Laser spectroscopic studies of state-dependent collisional quenching of the lifetimes of metastable antiprotonic helium atoms," *Phys. Rev. A*, vol. 57, pp. 1698–1712, Mar 1998.
- [51] M. Hori, K. Yamashita, R. S. Hayano, and T. Yamazaki, "Analog cherenkov detectors used in laser spectroscopy experiments on antiprotonic helium," *Nuclear Instruments and Methods in Physics Research Section A: Accelerators, Spectrometers, Detectors and Associated Equipment*, vol. 496, no. 1, pp. 102–122, 2003.
- [52] Hori, "Internal memo concerning the analysis of the $\bar{\text{p}}\text{He}^+$ experimental data measure in 2004." internal memo, 2004. internal memo.
- [53] M. Hori, "Buffer-gas cooling of antiprotonic helium to ~ 1.5 kelvin, and the antiproton-to-electron mass ratio," *Science*, 2016.

- [54] M. Hori, J. Eades, R. S. Hayano, T. Ishikawa, J. Sakaguchi, E. Widmann, H. Yamaguchi, H. A. Torii, B. Juhász, D. Horváth, and T. Yamazaki, “Sub-ppm laser spectroscopy of antiprotonic helium and a cpt-violation limit on the antiprotonic charge and mass,” *Phys. Rev. Lett.*, vol. 87, p. 093401, Aug 2001.
- [55] D. Bakalov and V. Korobov, “Hyperfine structure of antiprotonic helium energy levels,” *Phys. Rev. A*, vol. 57, pp. 1662–1667, Mar 1998.
- [56] H. Yamaguchi, R. S. Hayano, T. Ishikawa, J. Sakaguchi, E. Widmann, J. Eades, M. Hori, H. A. Torii, B. Juhász, D. Horváth, and T. Yamazaki, “Systematic study of the decay rates of antiprotonic helium states,” *Phys. Rev. A*, vol. 70, p. 012501, Jul 2004.
- [57] G. Y. Korenman and S. N. Yudin, “Coupled-channel analysis of collisional effects on hfs transitions in antiprotonic helium atoms,” *Journal of Physics B: Atomic, Molecular and Optical Physics*, vol. 39, no. 6, p. 1473, 2006.
- [58] C. T. Martin, A. Perillo-Marccone, M. Calviani, and J.-L. Munoz-Cobo, “The cern antiproton target: hydrocode analysis of its core material dynamic response under proton beam impact,” 2016.
- [59] D. Möhl, “Production of low-energy antiprotons,” *Hyperfine Interactions*, vol. 109, no. 1, pp. 33–41, 1997.
- [60] M. Hori and J. Walz, “Physics at cern’s antiproton decelerator,” *Progress in Particle and Nuclear Physics*, vol. 72, no. 0, pp. 206–253, 2013.
- [61] P. Belochitskii, T. Eriksson, A. Findlay, E. B. Holzer, R. MacCafferri, S. Maury, S. Pasinelli, F. Pedersen, and G. Tranquille, “Two years of ad operation: Experience and progress,” *CERN/PS 2002-046 (OP)*, p. 4 p, Jul 2002.
- [62] A. M. Lombardi, W. Pirkl, and Y. Bylinsky, “First operating experience with the cern decelerating rfq for antiprotons,” in *Particle Accelerator Conference, 2001. PAC 2001. Proceedings of the 2001*, vol. 1, pp. 585–587, 2001.
- [63] M. Hori, “Photocathode microwire monitor for nondestructive and highly sensitive spatial profile measurements of ultraviolet, x-ray, and charged particle beams,” *Review of Scientific Instruments*, vol. 76, no. 11, 2005.
- [64] M. Hori, “Spatial profile monitors for kev and mev antiproton beams,” *Nuclear Instruments and Methods in Physics Research Section A: Accelerators, Spec-*

- trometers, Detectors and Associated Equipment*, vol. 604, no. 1-2, pp. 154–157, 2009.
- [65] Temati, “Advanced cryogenic temperature sensors & thermometry for research, manufacturing & industry,” 06 2014. Retrieved on 09/2014 from <http://www.temati-uk.com/>.
- [66] Habia, “Habia cable,” 06 2014. Retrieved on 06/2014 from <http://habia.com/>.
- [67] Lakeshore, “Lakeshore cryotronics,” 03 2014. Retrieved on 03/2014 from <http://lakeshore.com/>.
- [68] A. Magnetics, “American magnetics,” 03 2014. Retrieved on 03/2014 from <http://americanmagnetics.com/>.
- [69] I. Tamm and I. Frank, “Coherent visible radiation of fast electron paspass through matter.,” *Compt. Rend. Acad. Sci. USSR*, vol. 14, p. 109, 1937.
- [70] M. Hori and A. Dax, “Chirp-corrected, nanosecond ti:sapphire laser with 6 mhz linewidth for spectroscopy of antiprotonic helium,” *Opt. Lett.*, vol. 34, pp. 1273–1275, Apr 2009.
- [71] C. V. Raman and K. S. Krishnan, “A new type of secondary radiation,” *Nature*, vol. 121, pp. 501–502, 1928.
- [72] W. R. Trutna and R. L. Byer, “Multiple-pass raman gain cell,” *Appl. Opt.*, vol. 19, pp. 301–312, Jan 1980.
- [73] D. V. Guerra and R. B. Kay, “Stimulated raman scattering in hydrogen pumped with a tunable, high power, narrow linewidth alexandrite laser,” *Journal of Physics B: Atomic, Molecular and Optical Physics*, vol. 26, no. 21, p. 3975, 1993.
- [74] A. W. et al., *Topics in Current Physics Raman Spectroscopy of Gases and Liquids*. Springer, 1979.
- [75] G. Boyd, W. Johnston, and I. Kaminow, “Optimization of the stimulated raman scattering threshold,” *Quantum Electronics, IEEE Journal of*, vol. 5, pp. 203–206, Apr 1969.
- [76] Y. R. Shen and N. Bloembergen, “Theory of stimulated brillouin and raman scattering,” *Phys. Rev.*, vol. 137, pp. 1787–1805, Mar 1965.

- [77] D. Cotter, D. C. Hanna, and R. Wyatt, “Infrared stimulated raman generation: Effects of gain focussing on threshold and tuning behaviour,” *Applied physics*, vol. 8, no. 4, pp. 333–340, 1975.
- [78] W. K. Bischel and M. J. Dyer, “Wavelength dependence of the absolute raman gain coefficient for the q(1) transition in h_2 ,” *J. Opt. Soc. Am. B*, vol. 3, pp. 677–682, May 1986.
- [79] C. S. Wang, “Theory of stimulated raman scattering,” *Phys. Rev.*, vol. 182, pp. 482–494, Jun 1969.
- [80] R. Heeman and H. Godfried, “Gain reduction measurements in transient stimulated raman scattering,” *IEEE journal of quantum electronics*, vol. 31, no. 2, pp. 358–364, 1995.
- [81] T. X. Phuoc, “Laser spark ignition: experimental determination of laser-induced breakdown thresholds of combustion gases,” *Optics Communications*, vol. 175, no. 4-6, pp. 419 – 423, 2000.
- [82] R. Kung, “Multiple pass stimulated raman conversion with pump depletion,” *Quantum Electronics, IEEE Journal of*, vol. 17, pp. 509–513, Apr 1981.
- [83] A. E. Siegman, *Lasers*. University Science Books, 1986.
- [84] D. Herriott, H. Kogelnik, and R. Kompfner, “Off-axis paths in spherical mirror interferometers,” *Appl. Opt.*, vol. 3, pp. 523–526, Apr 1964.
- [85] D. W. Vinson, W. M. Nutt, and B. B. Bullen, “Survey of the degradation modes of candidate materials for high-level radioactive waste disposal containers: Iron-base, corrosion-allowance materials,” *as a UCRL report*, 1995.
- [86] M. Hori, A. Dax, J. Eades, K. Gomikawa, R. S. Hayano, N. Ono, W. Pirkel, E. Widmann, H. A. Torii, B. Juhász, D. Barna, and D. Horváth, “Determination of the antiproton-to-electron mass ratio by precision laser spectroscopy of $\bar{\text{p}}\text{He}^+$,” *Phys. Rev. Lett.*, vol. 96, p. 243401, Jun 2006.
- [87] B. Juhasz, *Effect of foreign molecules on the lifetime of antiprotonic helium atoms*. PhD thesis, Debreceni Egyetem, 2004.
- [88] F. James, *MINUIT Function Minimization and Error Analysis Reference Manual*. CERN, Geneva (CH), March 1994.

- [89] J. Wolberg, *Data Analysis Using the Method of Least Squares: Extracting the Most Information from Experiments*. Springer, 2006.
- [90] R. S. Hayano, F. E. Maas, H. A. Torii, N. Morita, M. Kumakura, T. Yamazaki, H. Masuda, I. Sugai, F. J. Hartmann, H. Daniel, T. von Egidy, B. Ketzer, W. Müller, W. Schmid, D. Horváth, J. Eades, and E. Widmann, “Laser studies of the decay chain of metastable antiprotonic helium atoms,” *Phys. Rev. Lett.*, vol. 73, pp. 1485–1488, Sep 1994.
- [91] E. Widmann, I. Sugai, T. Yamazaki, R. S. Hayano, M. Iwasaki, S. N. Nakamura, H. Tamura, T. M. Ito, A. Kawachi, N. Nishida, W. Higemoto, Y. Ito, N. Morita, F. J. Hartmann, H. Daniel, T. von Egidy, W. Schmid, J. Hoffmann, and J. Eades, “Phase and density dependence of the delayed annihilation of metastable antiprotonic helium atoms in gas, liquid, and solid helium,” *Phys. Rev. A*, vol. 51, pp. 2870–2880, Apr 1995.
- [92] F. E. Maas, R. S. Hayano, T. Ishikawa, H. Tamura, H. A. Torii, N. Morita, T. Yamazaki, I. Sugai, K. Nakayoshi, F. J. Hartmann, H. Daniel, T. von Egidy, B. Ketzer, A. Niestroj, S. Schmid, W. Schmid, D. Horváth, J. Eades, and E. Widmann, “Laser-induced resonant transition at 470.724 nm in the $v = n - l - 1 = 2$ cascade of metastable antiprotonic helium atoms,” *Phys. Rev. A*, vol. 52, pp. 4266–4269, Nov 1995.
- [93] V. Chohan, M. Angoletta, M. Ludwig, O. Marquerssen, P. Odier, F. Pedersen, G. Transquille, U. Raich, L. Soby, and T. Spickermann, “Beam measurement systems for the cern antiproton decelerator (ad),” in *Particle Accelerator Conference, 2001. PAC 2001. Proceedings of the 2001*, vol. 3, pp. 2302–2304, 2001.
- [94] V. I. Korobov, “private communications.” 5 2016.
- [95] V. I. Korobov, “Calculation of transitions between metastable states of antiprotonic helium including relativistic and radiative corrections of order $R_\infty\alpha^4$,” *Phys. Rev. A*, vol. 77, p. 042506, Apr 2008.
- [96] E. Fermi and E. Teller, “The capture of negative mesotrons in matter,” *Phys. Rev.*, vol. 72, pp. 399–408, Sep 1947.
- [97] D. Horvath and F. Entezami, “On the models of coulomb capture of negative particles,” *Nuclear Physics A*, vol. 407, no. 3, pp. 297–308, 1983.

- [98] J. S. Cohen, “Slowing down and capture of negative muons by hydrogen: Classical-trajectory monte carlo calculation,” *Phys. Rev. A*, vol. 27, pp. 167–179, Jan 1983.
- [99] B. J. K. Toekesi and J. Burgdoerfer, “Exotic rydberg atom formation in low-energy antiproton-helium collisions,” *Journal of Physics B: Atomic, Molecular and Optical Physics*, vol. 38, no. 2, p. S401, 2005.
- [100] W. A. Beck, L. Wilets, and M. A. Alberg, “Semiclassical description of antiproton capture on atomic helium,” *Phys. Rev. A*, vol. 48, pp. 2779–2785, Oct 1993.
- [101] E. A. Solov’ev, “The advanced adiabatic approach and inelastic transitions via hidden crossings,” *Journal of Physics B: Atomic, Molecular and Optical Physics*, vol. 38, no. 12, p. 153, 2005.
- [102] J. S. Cohen, R. L. Martin, and W. R. Wadt, “Diabatic-state treatment of negative-meson moderation and capture. i. the hydrogen atom,” *Phys. Rev. A*, vol. 24, pp. 33–43, Jul 1981.
- [103] A. U. Hazi, “A purely l^2 method for calculating resonance widths,” *Journal of Physics B: Atomic and Molecular Physics*, vol. 11, no. 8, p. 259, 1978.
- [104] G. Y. Korenman, “Coupling of two- and three-particle channels in slow antiproton-atom collisions,” *Few-Body Systems. Suppl.*, vol. 12, pp. 45–49, 2000.
- [105] X. M. Tong, K. Hino, and N. Toshima, “A new time dependent scattering theory: Application to the capture of antiprotons by hydrogen atoms and helium atoms,” *AIP Conference Proceedings*, vol. 1037, no. 1, pp. 286–296, 2008.
- [106] X. M. Tong, K. Hino, and N. Toshima, “State-specified protonium formation in low-energy antiproton-hydrogen-atom collisions,” *Phys. Rev. Lett.*, vol. 97, p. 243202, Dec 2006.
- [107] J. X. Cheng and X. S. Xie, *Coherent Raman Scattering Microscopy*. Series in Cellular and Clinical Imaging, Taylor & Francis, 2012.
- [108] E. Garmire, F. Pandarese, and C. H. Townes, “Coherently driven molecular vibrations and light modulation,” *Phys. Rev. Lett.*, vol. 11, pp. 160–163, Aug 1963.

Acknowledgements

This thesis carries my name but to say it was all my work would be hubris. Many people have a share to all of which I am grateful. First I want to thank Professor T. W. Hänsch who gave me the great opportunity to work in his group. I also want to thank Dr. Horst Breuker and Yorick Blumenfeld who agreed to be my official supervisors while I was stationed at CERN. My direct supervisor Dr. Masaki Hori, I want to thank for many things but foremost for his passion for science and his patience with his students. I'm indebted to Dr. Daniel Barna for introducing me into the reality of experimental physics but also for being a great role model. I thank Ms. Anna Soter, my fellow PhD student and good friend, for her invaluable contributions on the technical and the personal level. My gratitude goes to my Japanese colleagues Koichi Todoroki, Takumi Kobayashi, Hiroyuki Yamada and Yohei Murakami for the interesting and productive time we shared. Furthermore I thank the entire ASACUSA collaboration for the professional environment and the excellent facilities at CERN that I was allowed to enjoy. Beyond that I thank Nobuaki Imai for his instructions on experimental nuclear physics. I'm deeply indebted to Karl Linner, Wolfgang Simon, Helmut Brückner and the MPQ workshop for their contributions regarding design and manufacturing of technical components. I thank Gabriele Gschwendtner and Ingrid Hermann for their administrative support. I thank Frederik Beaujean for his help with statistical problems. Of course I would also like to thank my office mates at MPQ Simon Holzner, Bernhard Bohn and Raphael Probst with whom I have shared a great time. Same goes for my friends and colleagues at CERN among them Manuel Alejandro Olmedo Negrete, Ruben Garcia Alia and Meric Taze who made my time at CERN significantly more enjoyable. Last but not least I thank the people who matter most in my life my family, my friends, my girlfriend and her family. This work was sponsored by the Wolfgang Gentner Programme of the Federal Ministry of Education and Research.

